PROTECT2024

9th International Colloquium on Performance, Protection & Strengthening of Structures Under Extreme Loading & Events

13 - 16 August 2024 I Singapore

CONFERENCE PROCEEDINGS

Organised by

NANYANG TECHNOLOGICAL UNIVERSITY SINGAPORE

NTU CEE Alumni Association

LIST OF TECHNICAL PAPERS

ID Number	Authors (s) – Paper Title
PS-21	***Jaswanth Gangolu, Hezi Grisaro –*** Parametric Analysis Of The Residual Axial Load Capacity Of Wide-flange Steel Columns Subjected To Far-field Detonations
PS-27	***Toshiyuki Horiguchi, Toshinobu Takahashi –*** Impact Force Of Evaluation For Full-scale Rockfall Protection Net Using Dem Applied Abstract To Planner Clump Model
PS-29	***Yuta Miyahara, Toshiyuki Horiguchi*** – Experiments On Debris Flow Impact Loads Using Open Sabo Dam Supported By Cables Abstract
PS-30	***Jianshe Xu, Ran Ma, Wei Wang*** – Features Of Prestressed Tendons With Caternary-cantilever Shape And Its Influence On Friction Loss And Inverted Arch Deflection
PS-31	***Ashok Malhotra, Scott McFadden, Babak Mashayekhi*** - Equivalent Static Pressure Design Procedure For Internal Pressure Due To External Blast
PS-32	***Ming Li, Changqing Miao, Manrong Song, Gezhi Xu, Pengyu Dong*** - Study On Fluctuating Wind Pressure Characteristics And Fatigue Performance Of Fully Enclosed Noise Barrier Of Beijing-xiong'an Intercity High-speed Railway Bridge
PS-33	***Jun Lei, Qing-Jun Chen, Miao-jin Yao, Yu-qi Zhang*** – Study On Dynamic Behavior Of Precast Concrete Columns With Pressed Sleeve Connections Under Impact Loading

PARAMETRIC ANALYSIS OF THE RESIDUAL AXIAL LOAD CAPACITY OF WIDE-FLANGE STEEL COLUMNS SUBJECTED TO FAR-FIELD DETONATIONS

Jaswanth Gangolu[1] and Hezi Grisaro[2]

[1] Technion Post Doctoral Fellow, Technion – Israel Institute of Technology, gangolu@campus.technion.ac.il.

[2] Assistant Professor, Technion – Israel Institute of Technology, hezi@technion.ac.il.

Corresponding Author: Jaswanth Gangolu, PhD

Technion – Israel Institute of Technology, Technion City, Haifa 32000, Israel

Email: gangolu@campus.technion.ac.il

ABSTRACT

This study employed a parametric numerical analysis to evaluate the residual axial capacity of wide-flange steel sections under combined static axial load and transverse far-field blast loading acting on its strong axis. These simulations entailed the variation of the Axial Load Ratios (ALRs) at levels ranging from 0-80% (of the capacity of the undamaged column) across various blast profiles. To validate the numerical methodology, it was benchmarked against two experimental cases, revealing a close alignment of displacement profiles. A similar procedure adopted for the validation was employed to 20 Finite Element (FE) simulations. Certain columns showed plastic deflections, retaining their structural integrity without failure when exposed to combined loading conditions, resulting in residual axial capacity. These values were utilized for computing the Damage Index (DI), representing the ratio of residual to maximum axial capacity, providing insight into the level of damage experienced by the columns. Graphical representations illustrating ALR and DI were presented, serving as valuable tools for informed decision-making regarding building occupancy. These findings can be instrumental in considering retrofitting options to preserve structural integrity, thereby averting the need for complete demolition, or rendering the building unusable.

Keywords: *Wide-Flange Steel Sections, Finite-Element Simulations, Axial Load Ratio, Far-Field Detonations, Damage Index.*

1. INTRODUCTION

The safety of buildings against blast-induced threats is crucial, given the constant risk of terrorism and accidental detonations [1]. Steel columns, as primary load-bearing elements, are vital for the stability of steel buildings, making their behavior under blast conditions a key

focus of research. Buildings often collapse due to damage to these columns, especially ground floor columns, leading to a widespread failure. Blast loading introduces complex interactions between axial load and lateral forces, which affect the response of steel columns. Understanding this interaction is essential for a more accurate assessment and optimal design of blast-resistant structures, especially in critical facilities. The occupancy of buildings post-blast is paramount, particularly in vital societal structures like petrochemical plants, hospitals, and military facilities. While research on axially loaded steel columns under blast loads is not as extensive as that on reinforced concrete columns, there are notable investigations available in the literature.

Nassr et al. [2] conducted tests on wide-flange steel columns loaded by axial force under detonations ranging from 50 to 250 kg ANFO explosive charges at stand-off distances of 7.0 m and 10.3 m. The axial load influenced lateral displacements by modifying the column fundamental period and the P-delta effect, leading to up to 1.58 times increment in deflection in columns with plastic damage state. Momeni et al. [3] explored the maximum displacement and residual load-carrying capacity of steel columns using LS-DYNA, considering various cross-sectional shapes. They observed minimal variations in global dynamic behavior, regardless of the specific cross-sectional shapes employed. Hadianfard et al. [4] utilized the Monte Carlo Simulation (MCS) approach to assess the likelihood of damage and emphasized the significant influence of support conditions on Damage Index (DI) determination. The DI, based on the ratio of residual to maximum axial capacity, reflects column damage levels. Here, the term maximum axial capacity refers to the column capacity before the blast load application, i.e. the capacity of the undamaged column. Changing support conditions from pinned to fixed ends decreased the probability of damage in flexural mode. In a study by Mazurkiewicz et al. [5], multistage numerical analyses in LS-DYNA assessed the load-carrying capacity, highlighting the blast resistance of HKS-300 steel sections and a significant capacity loss attributed to web-flange separation in I-sections. Grisaro et al. [6], in a numerical study using AUTODYN software, investigated close-in detonation on steel members. They found that the boundary conditions had no effect on the local damage but significantly impacted overall global behavior. The geometric shape of the charge was significant in a close-in detonation but not in the far-field range, where the load was uniformly distributed on the column [7]. Momeni et al. [8] developed an expression using gene expression programming to correlate the DI (based on residual axial capacity) with the standard displacement-rotational index. The equations were formulated using these LS-DYNA models to determine the initial and residual axial capacities of blast-loaded steel H-columns. Al-Thairy [9] proposed an analytical technique to compute the critical blast impulse for the loss of global stability in steel columns, validated using ABAQUS. In accordance with the literature, the numerical analysis provided precise results that corroborated the experimental conditions of blast loadings and effectively captured essential parameters.

UFC 3-340-02 [10] tends to mismatch with column capacity, especially for ductility ratios (μ) greater than 1.0, regardless of the applied axial load to Euler elastic buckling load ratio (P/P_e). Even when 'μ' is less than 1.0, the UFC method still does not match the column capacity when P/P_e exceeds 0.5 [11]. Accounting for P-delta effects is crucial for all structural components experiencing combined axial load and bending [10]. The Single-Degree-of-

Freedom Blast Effects Design Spreadsheets (SBEDS) software incorporates the impact of strain rate on column strength and deformations through a constant Dynamic Increase Factor (DIF). However, this approach assumes a uniform strain rate across the cross-section and along the element, therefore posing limitations [12],[13]. In blast-resistant design, the prevalent practice often involves using simplified models based on Single-Degree-of-Freedom (SDOF) dynamic analysis. While these models consider certain dynamic effects, they fall short of fully replicating true nonlinear behavior, resulting in uncertain structural responses that may lead to unforeseen failures.

In a building, the P-delta effect of a column stems from the interplay between axial loads and lateral deflections, introducing nonlinearity that generates additional bending moments during lateral displacements. This phenomenon significantly alters structural behavior, particularly for tall and slender columns facing lateral blast loads. Based on the limitations of existing literature, there is a need to conduct an assessment of the feasibility of occupying the structure after being loaded, and the impact of axial load on critical steel members in structures such as firecracker factories, hospitals, petrochemical facilities, schools, laboratories, etc. In essence, understanding the residual capacity of a column after a blast event and evaluating the risk of the disparity between the actual axial load and the residual capacity is crucial. For instance, if the actual axial load closely matches the residual capacity but is slightly lower, the risk associated with occupying the building is expected to be very high. To explore this scenario, the current study conducted a comprehensive analysis comprising numerical simulations using ANSYS LS-DYNA [14], focusing on four distinct column sections: W150X24, W200X71, HEB320, and HEB500. The simulations determined the residual axial capacity of the column, which was utilized to assess the damage extent under various applied axial loads, considering transversely applied blast loading on the column's strong axis. Before the parametric study, ensuring proper numerical validation is imperative, as outlined in the subsequent section.

2. FINITE ELEMENT (FE) NUMERICAL INVESTIGATION

2.1. Material Modelling and Structural Configuration

In this study, LS-DYNA, a Finite Element (FE) software, is utilized for both the pre-processing and post-processing stages to replicate a realistic model scenario. A 3D solid structure was generated to represent the elements subjected to a far-field blast load (Figure 1). The material model "Plastic Kinematic" (Mat_003) in LS-DYNA was selected for simulating the steel material of the columns, offering compatibility with isotropic and kinematic hardening plasticity, and accommodating rate effects if necessary [15]. The inputs for this model include mass density, Young's Modulus, Poisson's ratio, yield stress, tangent modulus, and hardening parameter. This study assumed the tangent modulus to be '0', indicating elastic behavior transitioning into a perfectly plastic state. The study adopts the kinematic hardening parameter

and incorporates strain rate parameters (C and P) based on the Cowper-Symonds relationship in the model. These parameters are employed to calculate the Dynamic Increase Factor (DIF).

$$DIF = 1 + \left(\frac{\dot{\varepsilon}}{C} \right)^{1/P} \quad (1)\ [14]$$

In the model (Eq. 1), the Dynamic Increase Factor (DIF), representing the increase in yield stress compared to the static value, was calculated using the strain rate ($\dot{\varepsilon}$) and constants C and P. Various studies have proposed different values for C and P. In this study, the chosen values were 599 (s^{-1}) for C and 0.753 for P, following the recommendations of [16]. Erosion was assigned to elements when the effective plastic failure strain was 20%. The study employed a fully integrated selective reduced (S/R) solid element with eight integration points on the element surface (ELFORM-2). The material model RIGID (Mat_020) was assigned to the rigid plates located above and below the I section.

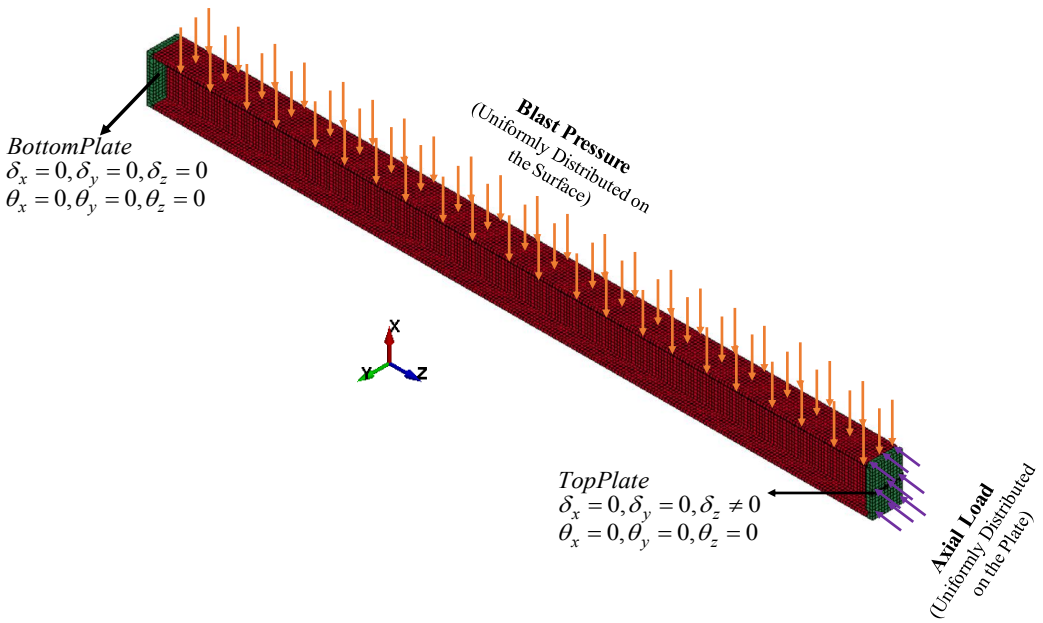

Figure 1 Three-dimensional wide-flanged solid configured model in LS-DYNA with boundary conditions

2.2. Application of Static Axial and Dynamic Blast Loads

In this study, the evaluation of the residual capacity of the steel I-section involved subjecting it to loadings at different stages (Figure 2). Under normal static conditions, a column in a building experiences an axial load from the superstructure. However, when exposed to blast loading along with the static axial load, the steel member may incur more significant damage or failure, endangering overall structural integrity. The axial load was applied to the member at all stages until column collapse (Figure 2). As the axial load is static, it should be applied statically. However, in this study, since the dynamic response stage was modeled in LS-DYNA as an explicit FE model, the initial static stage was also modeled as a part of dynamic simulation.

Thus, the axial load was applied at a given (and slow) loading rate to avoid dynamic effects. In the numerical model, initially, a linear axial load-time history was applied until reaching the required axial load level. The axial load remained constant until the model reached a steady state after the movement of the top plate attached to the column. At this point, the dynamic blast pressure was applied, as shown in Figure 1 and Figure 2. Given the study's focus on far-field detonations, it can be inferred that the blast loading applied on the column may be equivalent to a uniformly distributed load along its length.

LS-DYNA software was used to generate three distinct load profiles at different intervals. In all simulations, an initial axial load was applied until 1.0 sec, followed by a steady axial load until 1.1 sec (Figure 2). It was found that these time intervals were sufficiently slow to prevent dynamic effects during these simulated static phases. The intense blast pressure caused the section to undergo continuous and prolonged oscillations, significantly increasing the computational time needed for the simulation to reach the residual state post blast. To address prolonged oscillations, a damping force was introduced into the section at this stage. In this calculation phase, the damping force was applied to each node of the section, with a magnitude set at 20% of critical damping. The damping force remained active for a duration of 0.75 sec, effectively controlling and stabilizing the section oscillations during this crucial period. Once the section damage state was successfully controlled and stabilized, the model entered its last stage, where a linear (and slow) axial load time history was incrementally applied to the movable rigid plate until collapse (Figure 2), assessing the residual capacity of the column. In some simulations, the assessment of residual load-carrying capacity was not conducted, as the section failed under the blast loading and did not reach the residual stable state. For the modeling of far-field detonations in this study, the inclusion of modeling the air block was omitted, and the blast pressure was simulated as a directly applied pressure boundary condition.

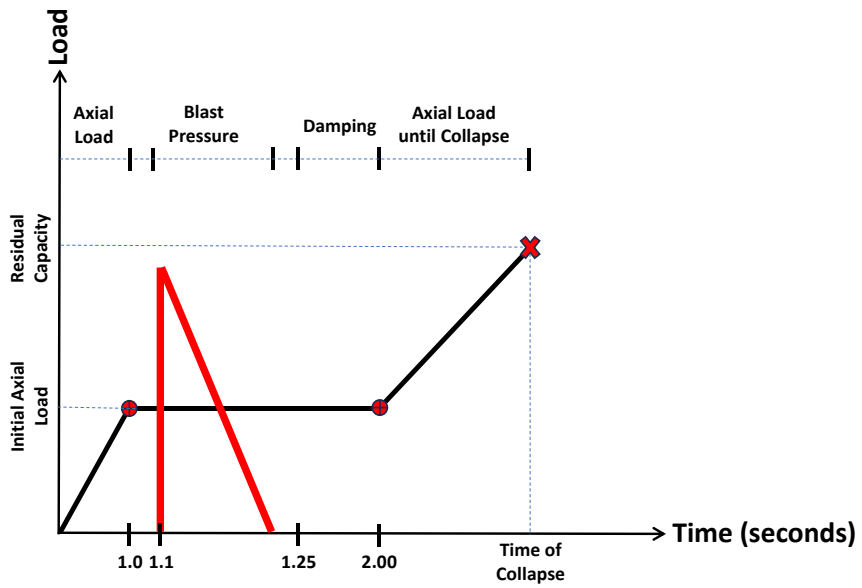

Figure 2 Column undergoing various stages of loading

2.3. Contact Interface and Boundary Conditions

In this study, all simulations (excluding validation models with distinct boundary conditions, as discussed in the following sections) were performed with fixed boundary conditions. The top plate was axially supported by a roller and fixed under all other conditions, while the bottom was completely fixed in all directions, as illustrated in Figure 1. The blast load was applied to induce bending along the strong axis of the section, and during the process of capturing the maximum axial load capacity, simulations revealed column failure along its axis due to buckling or compression failure (or a combination of both effects). However, the current study aims to analyze and assess simple case studies to deepen understanding of the scientific aspects involved in applying blast loads. Therefore, complex failure modes such as biaxial bending are beyond the scope. Two approaches were used to handle the contact between the I-section and the rigid plates (Figure 1). Firstly, an "AUTOMATIC SURFACE TO SURFACE" contact card was assigned, designating the rigid plates as the master and the steel section as the slave. Secondly, to ensure robust bonding while applying axial load, common nodes between the steel section and rigid plates were merged. Before conducting the parametric assessment of the steel section, a proper validation process is necessary to demonstrate the reliability of the selected numerical approach, as detailed in the subsequent section.

2.4. Finite Element (FE) Numerical Validation

For the validation process using LS-DYNA FE software, a steel I section, specifically W150X24, was chosen from Nassr et al. [11]. The selected section was subjected to blast pressures generated by charge masses of 100 kg and 150 kg at stand-off distances of 10.3 m and 9.0 m, respectively, inducing bending along both its weak and strong axes. The validation case employed equivalent uniform reflected pressure with its corresponding duration of all recorded pressure gauges, resulting in the use of an equivalent triangular blast load that has the same impulse. The dimensions of the I section were 2,413 mm in length, 160 mm in depth, 102 mm in width, with a flange thickness of 10 mm and a web thickness of 7 mm. The yield stress was 470 MPa, and an axial load of 270 kN (~25% of its maximum axial capacity) was applied to the top column. In the FE model, the axial load (270 kN) was distributed among the nodes of the top movable plate, with 204 nodes, resulting in a load of 1323.5 N applied to each node. The specific boundary conditions applied to the bottom and top plate of the column are $\delta_x=0$, $\delta_y=0$, $\delta_z=0$, $\theta_x=0$, $\theta_y\neq0$, $\theta_z=0$ and $\delta_x=0$, $\delta_y=0$, $\delta_z\neq0$, $\theta_x=0$, $\theta_y\neq0$, $\theta_z=0$ resembling the simply supported conditions wherein a hinge is positioned at the bottom and a roller is placed at the top. Blast pressure was applied in the x-direction for the strong axis and in the y-direction for the weak axis. The translation in the z-direction at the top of the column was released to enable the application of the axial load on the member. For validation purposes, a finer mesh with 10 mm spacing was assigned to the member. The same pre-processing keywords, as described in sections 2.1 to 2.3, were employed for both the validation and the remaining simulations (Table 1).

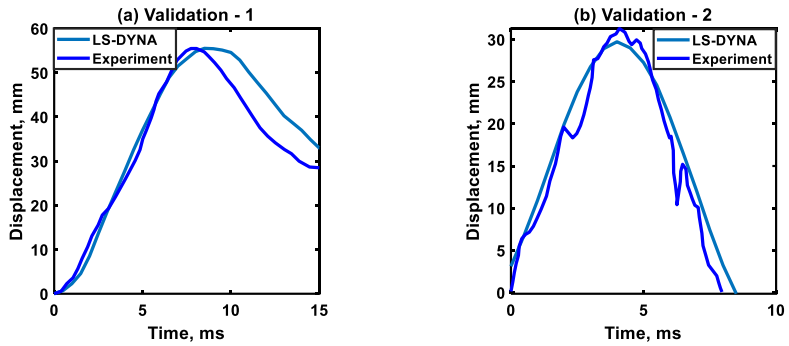

Figure 3 Displacement profiles of W150X24 sections with LS-DYNA (a) Validation – 1 (weak axis) and (b) Validation – 2 (strong axis)

The peak displacements obtained from both the experiment and FE simulation demonstrate favorable consistency in their displacement profiles (Figure 3). In validation 1 (blast load on weak axis), the experimental and FE simulation displacements were 55.5 mm and 55.4 mm, respectively, at durations of 7.7 ms and 8.5 ms (Figure 3 a). Similarly, for validation 2 (blast load on strong axis), the corresponding values were 30.8 mm and 29.7 mm at times of 4.3 ms and 4.0 ms, respectively (Figure 3 b). With the successful validation process, the current study aims to conduct further investigations on steel I sections, exploring their behavior under various axial loadings and blast pressures.

3. PARAMETRIC INVESTIGATION FROM FE SIMULATIONS

3.1. Maximum Axial Load Capacity

This study entailed the analysis of 20 unique FE simulations, categorized into four steel I sections: W150X24, W200X71, HEB320, and HEB500, each with five simulations. All 20 columns were assumed to have a length of 3,500 mm, aligning with the range of actual available columns, and their dimensions are detailed in Table 1 with a yield stress of 470 MPa. Before delving into the parametric analysis involving various Axial Load Ratios (ALRs), simulations were conducted to determine the column maximum axial loading capacity in the absence of any blast load (i.e. for undamaged columns). These values served as benchmarks for comparing the residual axial capacities after a blast. A linear (and slow) loading curve with respect to time, following the pattern discussed in sections 2.1 to 2.3, was employed. The simulation outcomes revealed the maximum capacity for W150X24, W200X71, HEB320, and HEB500 as 1,378.3 kN, 4,134.0 kN, 7,258.2 kN, and 10,327.5 kN, respectively. The maximum capacity obtained from the simulations was then compared with the values of $P_y = \sigma_y . A$ and, $P_{Euler} = \frac{\pi^2 EI}{l_{cr}^2}$. In the equations, P_y represents the maximum axial load capacity resulting from pure compression failure (i.e., full yielding of the cross-section), 'σ_y' denotes the yield stress of the steel I section, 'A' represents the area of the cross-section, P_{Euler} signifies the maximum axial load capacity

resulting from elastic buckling failure, 'E' stands for Young's modulus of the section, 'I' represents the moment of inertia in the strong axis, and l_{cr} is the effective length of the member.

Table 1. Dimensions of four chosen wide flanged I sections

Section	Length, mm	Width, mm	Depth, mm	Flange thickness, mm	Web thickness, mm
W150X24	3500	102	160	10.0	7.0
W200X71	3500	206	216	17.0	10.0
HEB320	3500	300	320	20.5	11.5
HEB500	3500	300	500	28.0	14.5

Table 2. Obtained maximum axial load capacities of the four chosen I sections

Section	Simulation (kN)	Compression (kN)	Euler (kN)	Buckling (kN), (SA) EN 1993-1-1	Buckling (kN), (WA) EN 1993-1-1
W150X24	1378.3	1419.4	1199.7	1399.0	1121.7
W200X71	4131.0	4147.2	16772.8	4204.1	3977.6
HEB320	7258.2	7289.7	62456.2	7289.7	7143.2
HEB500	10327.50	10922.8	85349.8	10922.8	10704.3

EN 1993-1-1 – Euro Code 3 [17], SA – Strong Axis, WA – Weak Axis

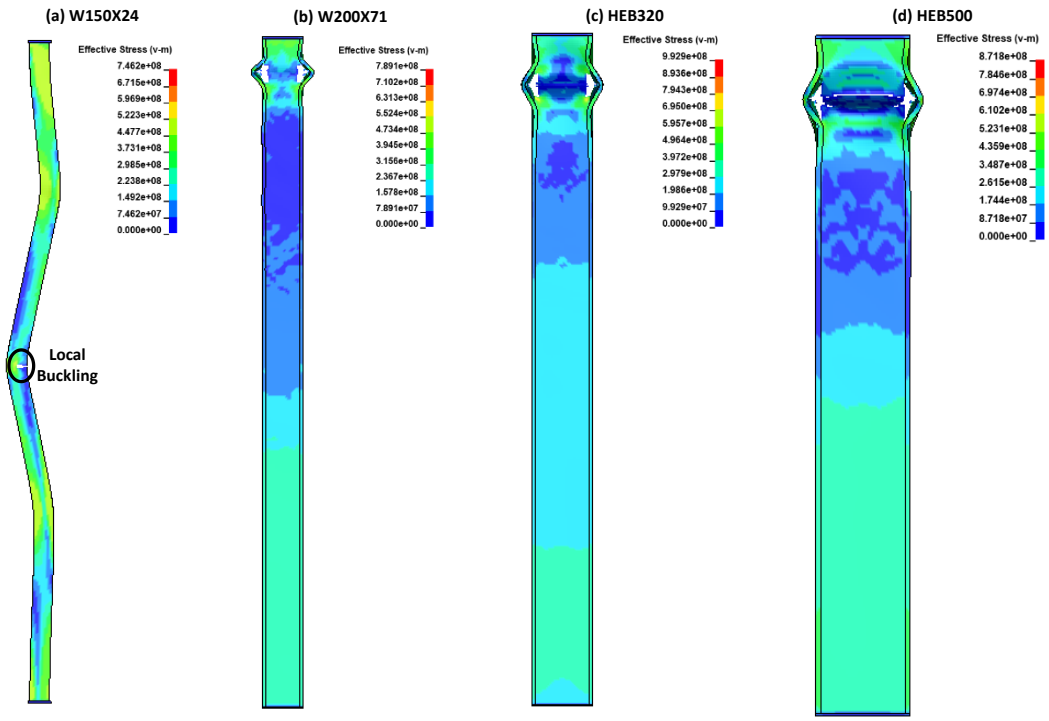

Figure 4 Failure modes and Von Mises Stress profiles of (a) W150X24, (b) W200X71, (c) HEB320 and (d)HEB 500 due to static axial load

The axial capacity of the sections was further evaluated using Eurocode 3, EN 1993-1-1 [17], considering local and global buckling and plasticity based on buckling curves (see Figure 4). Except for the W150X24 section, all other sections experienced compression failure under static axial load on top of the column. The W150X24 section yielded a value of 1,378.26 kN, closely aligning with the combined buckling and compression resistance specified in EN 1993-1-1, rather than pure buckling. This alignment is supported by the observed local buckling failure pattern (Figure 4 a). Simulation results for the W200X71 section indicated a maximum axial capacity of 4,131.0 kN, consistent with compression and EN 1993-1-1 specifications. This alignment is supported by the observed compression failure pattern (Figure 4 b). Similarly, the HEB320 and HEB500 sections followed a similar pattern of compression failure as the W200X71 section (Figure 4 c, d).

3.2. Effect of Axial Load Ratio (ALR) on the residual axial capacity

As mentioned in the preceding section regarding the maximum axial load capacity of each section, this study aims to investigate five distinct ALRs, specifically 80%, 60%, 40%, 20%, and 0% (representing no axial load during the application of the blast load). ALR refers to the ratio between the applied axial load and the maximum axial load capacity of the member $\left(ALR = \frac{P_{applied}}{P_{\text{maximum}}} \right)$ where $P_{applied}$ is applied axial load on the column and $P_{maximum}$ is maximum

axial load capacity of the column. A comprehensive investigation involving a total of 20 FE simulations was conducted, covering a broad range of blast pressures and time durations (Table 3). The simulations recorded the residual axial capacity of the section (Table 3). The simulations were conducted using LS-DYNA on a remote server with 512GB of RAM. The damage state of the member after blast loading was documented in the last column of the table.

To illustrate a representative outcome from the numerical simulations, a specific case, Model-2, has been chosen from the results presented in Table 3. This case study was employed to elucidate the scientific and technical aspects of the respective simulations. Model-2 entails the axial application of section W200X71 under various ALRs ranging from 0% to 80% at intervals of 20%. Subsequently, the section was subjected to a blast pressure of 1.15 MPa with a positive time duration of 11.0 ms. A plot of the axial nodal displacement at the top plate of the column revealed a sudden decrease, indicating the onset of failure. The time when this decline in displacement occurred was recorded, and the corresponding axial load was calculated, representing the residual axial capacity. At ALRs of 80%, the section experienced failure at its ultimate level during its dynamic blast load. However, it demonstrated resilience and maintained its structural integrity at ALR values of 0%, 20%, 40% and 60% under the same blast loading conditions. The residual axial capacity values distinctly illustrate the increment as the ALR decreases. The section demonstrated no resistance in cases with ALR values of 80% resulting in almost no load-bearing capacity. However, with a reduction of 20% ALR i.e. 60% the section resisted the blast pressure significantly with a residual axial capacity of 3,804.9 kN with a plastic damage state. Likewise, for other ALRs of 0%, 20% and 40%, the residual axial capacities were 4,098.6 kN, 4,069.4 kN, and 4,002.7 kN, respectively. Based on these results, the designer can allow the static axial load of 60% on the columns top with a blast pressure and time of 1.15 MPa and 11.0 ms. The difference in residual axial capacity of ALR from 0% to 60% is insignificant. Figure 5 (a, b, c, d, e) illustrates the plastic deformation and variation in effective stresses for ALRs ranging from 0% to 80%, where red signifies the highest stress level, while blue indicates the lowest (Figure 5). The contours vary with respect to time. The secondary geometric nonlinear structural behavior, particularly the P-delta effects, was markedly influenced by the combined effect of axial and transverse blast loads. The finite element analysis underscores the substantial impact of axial load during blast loading in a building, emphasizing the necessity to account for axial load effects in the design of structures, particularly in critical locations such as petrochemical facilities, hospitals, and laboratories.

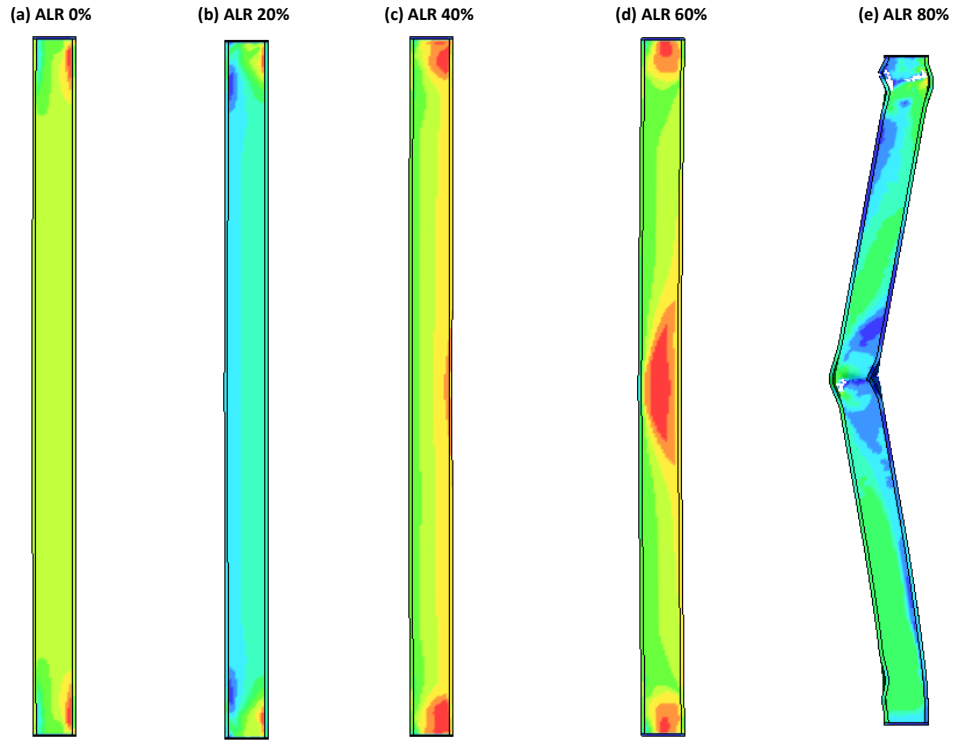

Figure 5 Plastic deformation of W200X71 section and its effective stress variations of ALR's (a) 0%, (b) 20%, (c) 40%, (d) 60% and (e) 80%. Red color indicates maximum values.

Table 3 Analysis of 20 Models: Results and Member Condition following Blast Loading

S. No	Section	Maximum Axial Load (kN)	ALR (%)	Axial Load Applied (kN)	Blast Peak Pressure (MPa)	Duration (msec)	Residual Axial Capacity (kN)	Damage Index (DI)	State of Section
1	W150X24 (Model-1)	1378.2	80	880.1	0.40	9.1	1220.2	0.110	Plastic
2			60	660.0	0.40	9.1	1298.5	0.060	Plastic
3			40	440.0	0.40	9.1	1305.1	0.050	Plastic
4			20	220.0	0.40	9.1	1349.3	0.020	Plastic
5			0	0.0	0.40	9.1	1378.2	0.000	Elastic
6	W200X71 (Model-2)	4131.0	80	3304.8	1.15	11.0	-	1.000	Failed
7			60	2478.6	1.15	11.0	3806.8	0.078	Plastic
8			40	1652.4	1.15	11.0	4002.7	0.031	Plastic
9			20	826.2	1.15	11.0	4069.3	0.015	Plastic
10			0	0.0	1.15	11.0	4098.6	0.008	Plastic
11	HEB320 (Model-3)	7258.1	80	5806.5	1.65	18.7	-	1.000	Failed
12			60	4354.9	1.65	18.7	7042.1	0.030	Plastic
13			40	2903.2	1.65	18.7	7195.5	0.009	Plastic
14			20	1451.6	1.65	18.7	7205.9	0.007	Plastic
15			0	0.0	1.65	18.7	7212.1	0.006	Plastic
16	HEB500 (Model-4)	10327.5	80	8262.0	4.04	13.4	-	1.000	Failed
17			60	6196.5	4.04	13.4	10327.5	0.000	Elastic
18			40	4131.0	4.04	13.4	10327.5	0.000	Elastic
19			20	2065.5	4.04	13.4	10327.5	0.000	Elastic
20			0	0.0	4.04	13.4	10327.5	0.000	Elastic

3.3. Damage Index (DI)

In addition to exploring the residual axial capacity, this study also investigated the Damage Index (DI) using those values. The DI was calculated based on the residual axial load capacity of the column, as outlined in Table 3. The formulation for the DI of the section is as follows:

$$DI = 1 - \frac{P_{residual}}{P_{\max imum}} \tag{2}$$

Where, DI – Damage Index, $P_{residual}$ – residual axial capacity of the section after the response to blast load, $P_{maximum}$ – Maximum axial capacity of the section (Eq. 2). The residual axial capacity of the column represents the amount of residual axial load that the column can carry or resist after being subjected to the combined effects of axial and blast loads. The values obtained from the simulations were recorded and presented in tabular form in Table 3. In this context, a DI value of '1.0' signifies the total failure of the column, while a DI value of '0' indicates no damage in the column as it remains in its elastic state. The DI serves as a measure of the structural integrity and failure level of the column under the given axial load and blast conditions. The selected sections from the FE analysis are graphed with ALR on the x-axis and DI on the y-axis in Figure 15 (a, b). Note that the figure shows linear lines connecting the calculated point. However, more simulations may be added to study the more realistic behavior between the calculated points.

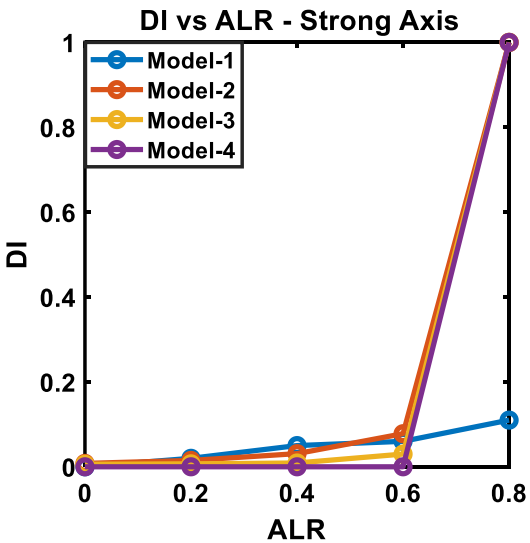

Figure 6 Damage Index with corresponding Axial Load Ratio of Model 1 to 4

The simulations demonstrate that varying percentages of axial load on the column, under the same blast load, significantly influence the DI or damage level of the section. For example, in Model-2, the DI for an ALR of 80% was '1.0', indicating complete failure of the section. However, the same model with an ALR of 60% produced a DI of '0.078' and settled in a plastic state. The difference in the damage level between the two models is 92.2%, highlighting the critical influence of axial load for similar blast profiles. A noteworthy observation from all simulations is that reducing the axial load by 20% results in a large

difference in DI in certain cases. Based on these plots, informed decisions can be made regarding the occupancy of the building. By analyzing the graphs, it can be assessed whether retrofitting measures can be implemented to ensure the column structural integrity, rather than opting for complete destruction or rendering the building unusable.

4. CONCLUSIONS

A numerical parametric study utilizing LS-DYNA with 20 FE models was conducted, employing the Plastic Kinematic material model to address strain rate effects in blast loading scenarios. Validation ensured accuracy, aligning well with experimental results. Four sections were assessed for maximum axial load capacity, revealing failure modes: local buckling for W150X24 and compression for others. Results were compared against compression failure, Euler's buckling, and Eurocode 3, showing reasonable agreement. The study explores the influence of five Axial Load Ratios (ALRs), leading to elastic behavior, plastic deformation, or failure, on the residual axial capacity. Axial loads significantly impacted residual axial capacity, while combined loads affected secondary geometric nonlinear behavior (P-delta effects). Reduction in ALR by 20% notably enhanced section resistance and stiffness, as observed from ALR vs DI plots. Findings inform occupancy decisions and retrofitting strategies for critical structures, aiding their integrity and resilience. Future research could extend probabilistic equations to address displacement and axial capacity, considering more intricate boundary conditions.

ACKNOWLEDGMENTS

Financial support for this study has been provided by the Technion Israel Institute of Technology.

REFERENCES

[1] Gangolu, J., Kishore, K. B., & Sharma, H. (2023). Probabilistic demand models and reliability based code calibration for reinforced concrete column and beam subjected to blast loading. Reliability Engineering & System Safety, 240, 109577.

[2] Nassr, A. A., Razaqpur, A. G., Tait, M. J., Campidelli, M., & Foo, S. (2014). Dynamic response of steel columns subjected to blast loading. Journal of structural engineering, 140(7), 04014036.

[3] Momeni, M., Hadianfard, M. A., Bedon, C., & Baghlani, A. (2019, August). Numerical damage evaluation assessment of blast loaded steel columns with similar section properties. Structures (Vol. 20, pp. 189-203). Elsevier.

[4] Hadianfard, M. A., Malekpour, S., & Momeni, M. (2018). Reliability analysis of H-section steel columns under blast loading. Structural Safety, 75, 45-56.

[5] Mazurkiewicz, L., Malachowski, J., & Baranowski, P. (2015). Blast loading influence on load carrying capacity of I-column. Engineering Structures, 104, 107-115.

[6] Grisaro, H. Y., Seica, M. V., Packer, J. A., & Li, W. (2021). Strong-axis response of steel I-sections subjected to close-in detonations. International Journal of Protective Structures, 12(3), 347-376.

[7] Grisaro, H. Y., Edri, I. E., & Rigby, S. E. (2021). TNT equivalency analysis of specific impulse distribution from close-in detonations. International Journal of Protective Structures, 12(3), 315-330.

[8] Momeni, M., Hadianfard, M. A., Bedon, C., & Baghlani, A. (2020). Damage evaluation of H-section steel columns under impulsive blast loads via gene expression programming. Engineering Structures, 219, 110909.

[9] Al-Thairy, H. (2018). Behaviour and failure of steel columns subjected to blast loads: Numerical study and analytical approach. Advances in Materials Science and Engineering, 2018.

[10] US Department of Defense. Structures to resist the effects of accidental explosions. US Department of Defense; 2008. UFC 3-340-02.

[11] Nassr, A. A., Razaqpur, A. G., Tait, M. J., Campidelli, M., & Foo, S. (2013). Strength and stability of steel beam columns under blast load. International Journal of Impact Engineering, 55, 34-48.

[12] ASCE. (2011). "Blast protection of buildings." ASCE/SEI 59-11, New York.

[13] Nassr, A. A., Razaqpur, A. G., Tait, M. J., Campidelli, M., & Foo, S. (2012). Single and multi degree of freedom analysis of steel beams under blast loading. Nuclear Engineering and Design, 242, 63-77.

[14] Hallquist, J. O. (2007). LS-DYNA keyword user's manual. Livermore software Technology corporation, 970, 299-800.

[15] Gangolu, J., Daudeville, L., Rao Gangolu, A., & Sharma, H. (2023). Improvement of Probabilistic Models for Prediction of Missile-Impact Effects on Reinforced Concrete Protective Panels Using an Experimental and Numerical Database. Journal of Performance of Constructed Facilities, 37(5), 04023036.

[16] Cadoni, E., & Forni, D. (2015). Strain rate effects on reinforcing steels in tension. In EPJ Web of Conferences (Vol. 94, p. 01004). EDP Sciences.

[17] EN 1993-1-1 (May 2005) Eurocode 3: Design of steel structures – Part 1-1: General rules and rules for buildings, CEN, Brussels.

IMPACT FORCE OF EVALUATION FOR FULL-SCALE ROCKFALL PROTECTION NET USING DEM APPLIED TO PLANNER CLUMP MODEL

Toshiyuki Horiguchi[1], Toshinobu Takahashi[2]

[1] PhD, National Defense Academy, Dept. Civil Engineering, htoshi@nda.ac.jp

[2] Tokyo Rope MFG. CO. LTD, takahashi.toshinobu@tokyorope.jp

Corresponding Author: Toshiyuki Horiguchi, PhD

1-10-20, Hashirimizu, Yokosuka, Kanagawa, Japan, 2380811

Email: htoshi@nda.ac.jp

ABSTRACT

In Japan, the road traffic network infrastructure, driven by escalating traffic demand and urbanization, has precipitated a rise in rockfall incidents. Therefore, falling rock protection nets have been deployed, necessitating a rigorous evaluation of their structural load-bearing capacities. This study presents a simulation of a full-scale falling rock protection net using the 3D-distinct element method (3D-DEM). In addition, the proposed method reproduced the unevenness in representing the planar clump model. First, a collision experiment was performed in advance, the dynamic deformation process of the wire net was recorded using video and a high-speed camera, and the tension of the wire ropes was measured. Second, the net and wire ropes were modeled using cylindrical and spherical elements. The reproducibility of the analysis results was examined by comparing with the experimental results. Therefore, the interlocking between the wire and dead weight and the relationship between the impact load and time in the experiment can be represented by the proposed method. The results showed that local deformations around the impact area caused by a heavy-weight collision spread within the protective net, and demonstrated that ropes far from the impact point experienced delayed maximum tension owing to wave propagation.

Keywords: *Full-scale protection net, Distinct element method, Impact Loading, planner clump model, connect spring.*

1. INTRODUCTION

The latest worldwide statistics on natural disasters such as landslides, debris flows, and earthquakes indicate an increase in casualties. Japan has numerous steep hills and unstable ground; moreover, the ground and natural instability of the soil have overcome the need to expand road traffic networks [1]. Recently, a rock of 1.0 m diameter fell directly on a moving car in Shimane in 2016. Against the backdrop of similar accidents, prefecture offices and responsible organizations strongly insist on improved road management [2]. Disasters such as rockfall accidents, human casualties, and traffic disruptions affect everyday life. Effective falling protection nets developed based on performance-based design are needed in mountainous areas such as Japan. The falling protection net illustrated in **Figure 1** was constructed to measure the falling rock. The falling protection net, which is composed of a wire rope and metal mesh, has a marginal bend rigidity similar to construction materials. Therefore, any impact force is expected to reduce the impact load across the entire net structure. Otherwise, the net acts as a flexible structure that cannot maintain its shape, and the response shape after collision with a falling rock is different from the initial shape. Because it is necessary to define the limit state, including the serviceability limit, for standard materials, the energy calculation method is generally used as part of the design method. Essentially, this method calculates the kinetic energy of the falling rock and the absorption energy of the net. Therefore, a full-scale falling protection net capable of absorbing energy is required for a comprehensive experiment. However, experiments involving various crash positions and the destruction characteristics observed in numerous cases have rarely been conducted. Numerical approaches were adopted to simulate the experiments. Consequently, several studies involving impact response experiments were conducted by various methods [3]-[5]. In addition, experiments on the response of a falling protection net of height 3 m and width 3 m to a rock falling on it with a kinetic energy of 1.0-3.2 kJ confirmed the capacity of the net to provide safety [6]. In another study, the energy absorption mechanism of a falling rock protection net was investigated [7]-[9], and an accumulator was installed at the end of the harnessing rope. Moreover, Sonoda et al. performed an impact response analysis of a wire–ring net system using an improved SPH method [10]. This study aimed to simulate the impact response of wire ring nets composed of a soft steel mesh. Moreover, we conducted an experiment and analysis to estimate the strength of a soft structure [11]. In this study, an improvement in the computational efficiency is aimed at decreasing the number of elements, including long and slender ones, such as ropes modeled by the cylindrical element of the distinct element method (DEM). The proposed method of DEM was able to reproduce the net behaviour and load-time relationship in the analysis of a 400 KJ type rockfall protection net. We demonstrated the reproduction of the deformation response using DEM in impact experiments on full-scale rockfall protection nets. The results demonstrated that the load-time relationship of the rockfall protection net can be expressed. However, to pseudo-express the

Figure 1. Falling rock protection net

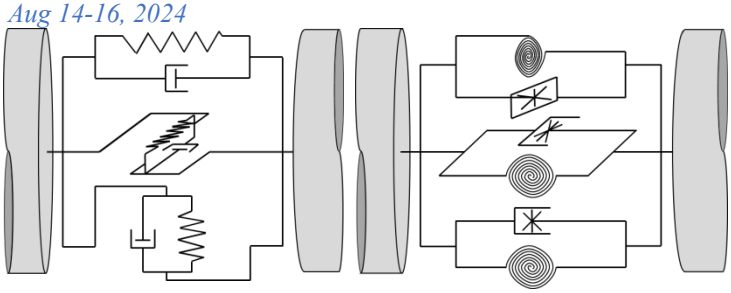

Figure 2. Between elements of the connected spring: Right is the axial spring for axial force and Left is rotational spring for moment force.

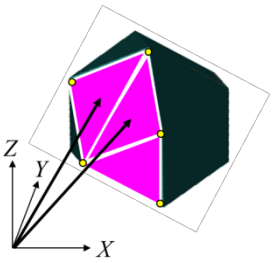

Figure 3. Sample of the plane clump model using assemble

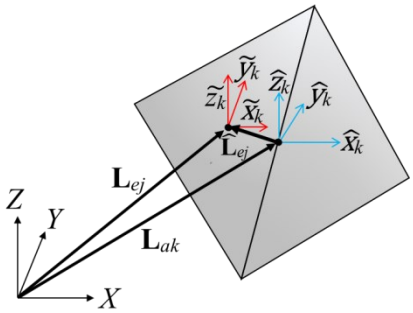

Figure 4. Coordinate system of the constituent elements within the clump element (initial coordinates)

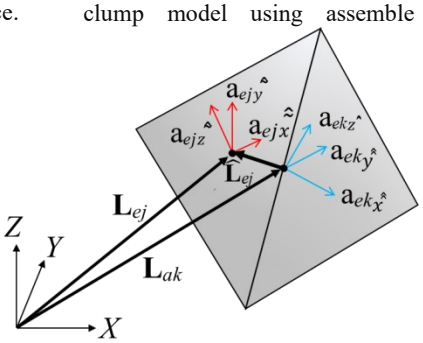

Figure 5. Attitude matrix

irregularities of the spherical shape of the heavyweight, it is necessary to increase the friction angle between the original elements and significantly increase the rotational motion [12].

This study proposes an assembly element model that combines planar elements to reproduce the shape of the weight using DEM and examines the reproducibility with experiments from the aspects of tension and response.

2. PLANER CLUMP MODEL

2.1. Outline of the proposed DEM

The proposed DEM utilizing connecting springs was employed to model a wire net that mitigated the impact of falling rocks. The wire rope structure was divided into appropriate lengths with rigid cylindrical or spherical elements corresponding to the actual length. These are connected by springs, which represent the stiffness of the rope. As shown in **Figure 2**, the spring has six degrees of freedom corresponding to the three-dimensional components of the translational and bending rotations determined by the orientation of the spring in the local coordinate system. In addition, dashpots were installed parallel to each component. Here, we focus on a plane element assembly that replicates the shape of a falling weight. **Figure 3** illustrates the coordinate system and shows examples of the components of the assembly element. The advantage of the Planer clump model is that it can represent elements of similar shape by combining spherical elements, but it is computationally expensive. In addition, the use of spherical elements makes it impossible to represent elements with corners.

2.2. Coordinate of the clump model

In **Figure 4**, the plane, cylindrical, and spherical elements are color-coded to indicate that they are assembly components. The proposed plane element assembly uses cylindrical and spherical

elements because constructing the components solely with planes makes contact determination difficult and increases the computational cost. **Figure 5** shows the relationships between the planes extracted from **Figure 4**. First, the state of the assembly element sets an unrelated global coordinate system (X, Y, Z). Subsequently, a local coordinate system ($\hat{x}$, $\hat{y}$, $\hat{z}$) parallel to the general coordinate system is established at the center of gravity of the assembly element, as well as another local coordinate system ($\tilde{x}$, $\tilde{y}$, $\tilde{z}$) parallel to the center of gravity of the elements (the so-called constituent elements) that make up the assembly.

2.3. Attitude matrix and Compatibility condition

In this case, we solved for translational motion in the general coordinate system and rotational motion in the inertial principal axis coordinate system of the assembly element in the equations of motion. Therefore, transformation conditions that convert the solution into the motion of the constituent elements are necessary. First, the attitude vectors at the initial analysis ($t = 0$) and time ($t = t$) are provided. In this case, the change due to rotation of the principal axis of inertia of the assembly element is expressed by the following equation:

$$\mathbf{A}_{ak\text{-}t}=\widehat{\mathbf{A}}_{ak\text{-}t}\mathbf{A}_{ak\text{-}0} \tag{1}$$

where $\mathbf{A}_{ak\text{-}0}$, $\mathbf{A}_{ak\text{-}t}$ are the attitude matrices of clump element k at a time and $\widehat{\mathbf{A}}_{ak\text{-}t}$ is the coordinate transformation matrix representing the change in the attitude matrix of assembly element k over time.

Since the assembly element is rigidly connected, the following equation holds.

$$\mathbf{A}_{ej\text{-}t}\mathbf{A}_{ak\text{-}t}^{\mathrm{T}}=\mathbf{A}_{ej\text{-}0}\mathbf{A}_{ak\text{-}0}^{\mathrm{T}}=\widehat{\widehat{\mathbf{A}}}_{aej} \tag{2}$$

$$\widehat{\mathbf{L}}_{ej\text{-}t}=\widehat{\mathbf{A}}_{ak\text{-}t}^{\mathrm{T}}\widehat{\widehat{\mathbf{L}}}_{ej\text{-}0} \tag{3}$$

where $\mathbf{A}_{ej\text{-}0}$, $\mathbf{A}_{ej\text{-}t}$ are the attitude matrices of constituent element j at times $t = 0$ and $t = t$, respectively; $\widehat{\widehat{\mathbf{A}}}_{aej}$ is the attitude matrix of the constituent element j in the inertia principal axis coordinate system of the assembly element k; $\widehat{\mathbf{L}}_{ej\text{-}t}$ is the position vector of the center of gravity of the constituent element j in the assembly element coordinate system at a time; and $\widehat{\widehat{\mathbf{L}}}_{ej\text{-}0}$ is the position vector of the center of gravity of constituent element j in the inertia principal axis coordinate system of the assembly element. $\widehat{\widehat{\mathbf{A}}}_{aej}$and $\widehat{\mathbf{L}}_{ej\text{-}t}$ are invariant regardless of motion.

$$\mathbf{L}_{ej\text{-}t}= \mathbf{L}_{ak\text{-}t}+\widehat{\mathbf{L}}_{ej\text{-}t} \tag{4}$$

$$\mathbf{A}_{ej\text{-}t}=\widehat{\widehat{\mathbf{A}}}_{aej}\mathbf{A}_{ak\text{-}t} \tag{5}$$

where $\mathbf{L}_{ak\text{-}t}$ and $\mathbf{L}_{ej\text{-}t}$ are the position vectors of assembly element k and constituent element j at the time, respectively.

Therefore, by updating $\mathbf{A}_{ak\text{-}t}$ in (4) and (5), it becomes possible to update other vectors and matrices. The velocity and angular velocity vectors are expressed as follows:

$$\dot{\mathbf{u}}_{ej\text{-}t}=\dot{\mathbf{u}}_{ak\text{-}t}+\boldsymbol{\omega}_{ak\text{-}t}\times\widehat{\mathbf{L}}_{ej\text{-}t} \tag{6}$$

$$\boldsymbol{\omega}_{ej\text{-}t}=\boldsymbol{\omega}_{ak\text{-}t} \tag{7}$$

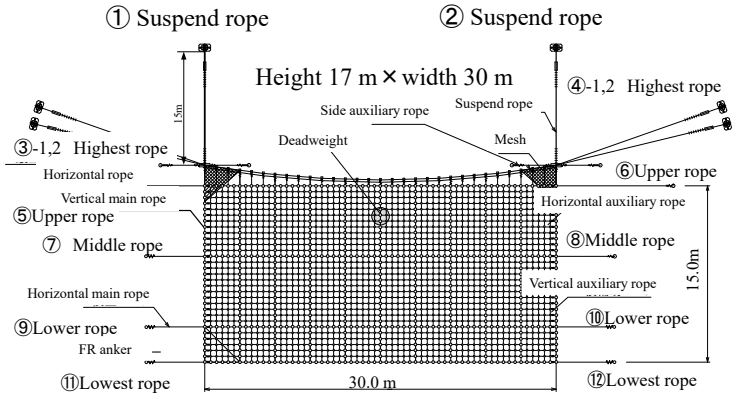

Figure 6. Full scale of rockfall protection net in the experimental facility

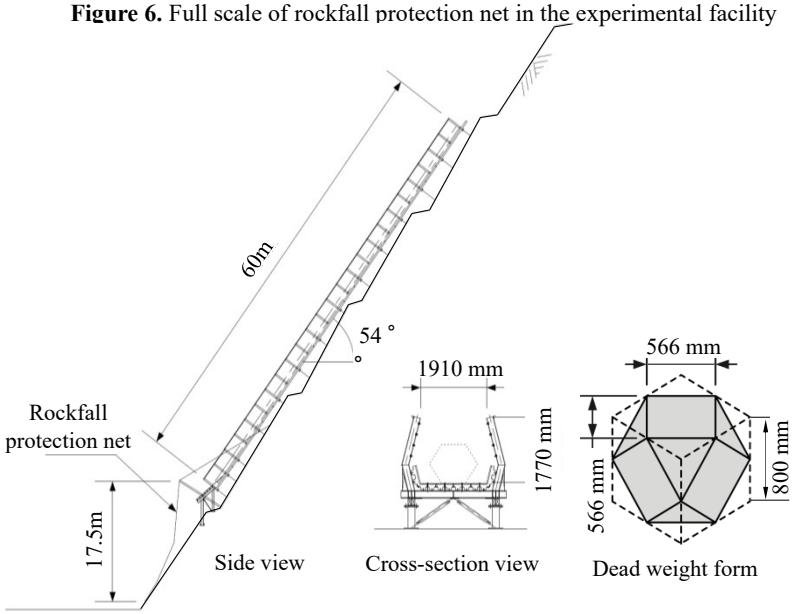

Figure 7. Experimental facility and shape of the weight

where, $\dot{\mathbf{u}}_{ak\text{-}t}$and $\dot{\mathbf{u}}_{ej\text{-}t}$ are the velocity vectors of the assembly element k or constituent element j at the time, and $\boldsymbol{\omega}_{ak\text{-}t}$ and $\boldsymbol{\omega}_{ej\text{-}t}$ are the angular velocity vectors of assembly element k or constituent element j at time.

2.4. Constituent element and force equilibrium matrix

The equations of motion were solved for the center of gravity of the assembly element. Therefore, for each element, the contact determination and calculation of contact forces were performed using the constituent elements, and the forces acting on the center of gravity of each constituent element were integrated into the center of gravity of the assembly element. In this case, there is a relationship between the force acting on the center of gravity of the constituent element in the constituent element coordinate system and the force acting on the assembly element in the assembly element coordinate system, which is given by the following equation:

$$\widehat{\mathbf{F}}_{ak} = \sum_{j=1}^{n_{ak}} \tilde{\mathbf{f}}_{ej} \tag{12}$$

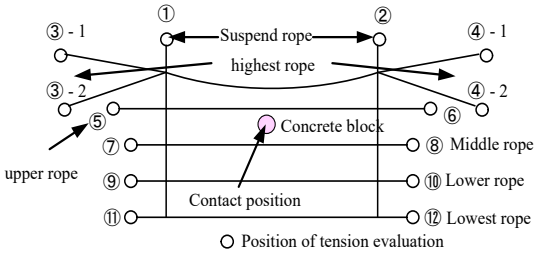

Figure 8. Position of tension evaluation for load cell

Table 1. Experiment condition

Item	Value
Specification	Concrete block (14 hedron) 1.0 t
Suspended rope	7×7, 24φ
Highest rope	7×7, 24φ
Vertical main rope	3×7, 18φ
Traversal main rope	3×7, 18φ
Vertical auxiliary rope	3×7, 14φ
Horizontal auxiliary rope	3×7, 14φ
Wire mesh	5.0φ×50×50
Predicted energy at design (impact velocity)	378 kJ (27.5 m/s)

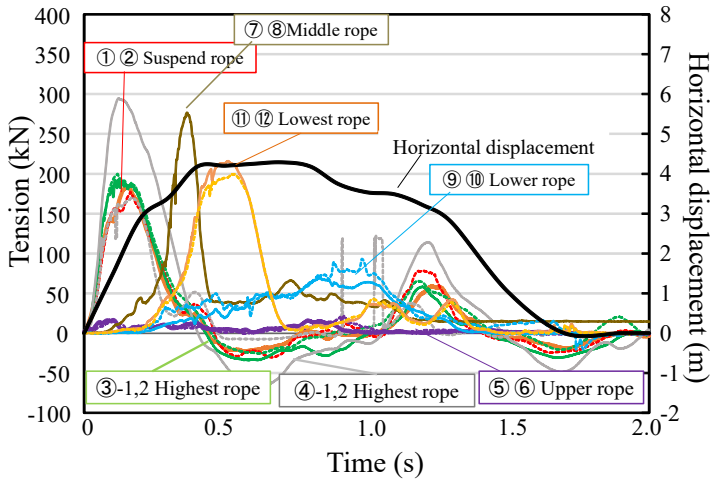

Figure 9. Tension and displacement response

3. Experiment on the full-scale falling protection net

3.1. Outline of the experiment

The experimental facility shown in **Figure 6** and **Figure 7** can drop a weight from a specified height to collide with a full-scale protection net measuring 15 and 21 m in height and width, respectively. The rockfall protection net is constructed with vertical and horizontal ropes arranged in a grid pattern at 1.0 m intervals, and a diamond-shaped wire mesh with a wire diameter of 5 mm and a mesh size of 50 mm × 50 mm is stretched on the inner (mountain-side) surface and fixed with coil-shaped connectors. **Figure 7** shows the experimental setup. The weight is dropped from a vertical height of 40 m using a slope with a 54° incline. **Table 1** lists the experimental conditions used in the study. Additionally, for this experiment, the overall behaviour of the protection net was recorded using a video recorder, and load cells were installed at the positions marked with circles in **Figure 8** to measure the rope tension.

3.2 Results of the experiment

The response of the protection net in the weight impact experiment is also shown. The impact velocity of the weight, determined from the continuous camera images, was 23.6 m/sec, the kinetic energy was 346 kJ, and the impact angle was 23.7° with respect to the horizontal plane.

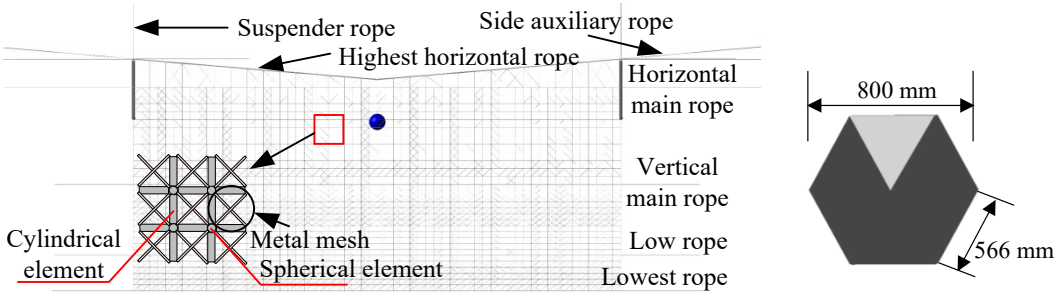

(a) Rockfall protection net model **(b)** Proposed model

Figure 10. Analysis model

Table 2. Analysis parameter

Item			Value
Wire Rope	7×7 φ24	Axial spring *EA* (N)	2.9×10^{7}
		Bending direction spring *EI* (N·m^2)	24.4
	3×7 φ18	Axial spring *EA* (N)	1.2×10^{7}
		Bending direction spring *EI* (N·m^2)	2.5
	3×7 φ14	Axial spring *EA* (N)	7.9×10^{6}
		Bending diretion spring *EI* (N·m^2)	0.9
Wire mesh		Axial spring *EA* (N)	1.3×10^{4}
		Bending direction spring *EI* (N·m^2)	0.0
Deadweight		Cylinder element	24
		Spherical element	12
		Plane element	20
		Mass(kg)	1000
		Initial velocity(m/s)	20.8
		Rotation (rad/s)	31.4
Between element		Normal direction k_n (N/m)	1.0×10^{7}
		Tangential direction *k*s (N/m)	3.0×10^{6}
		Viscosity *C* (N)	0
		Coefficient of friction tan φ	0.577
		Dumping constant	0.2
Time conditon			3.0×10^{-7}

Figure 9 shows the time history response of the tension generated at each fixed end of the rope. The response waveform begins with an increase in tension for the hanging ropes (I, II) and the topmost ropes (③, ④). Subsequently, after the tension in the upper ropes (⑤, ⑥) reaches its maximum and decreases, the tension in the middle ropes (⑦, ⑧) located at the lower part increases. After the tension of the middle ropes decreases, the tension of the bottom ropes (⑪, ⑫) increases. Additionally, the second peak occurs after $t = t_0 + 0.7$ s, when the protective net pushes back the weight.

4. DEM simulation

4.1. Analysis model

Figure 10(a) shows the analytical model of the rockfall protection net and falling weight. The falling weight model in **Figure 10(b)** uses cylindrical, spherical, and planar elements. The net was composed of spherical, cylindrical, and connected springs. Spherical elements were placed at the junction points of the vertical and horizontal ropes, and the ropes between the junction points were modeled with two cylindrical elements. Additionally, cylindrical elements were

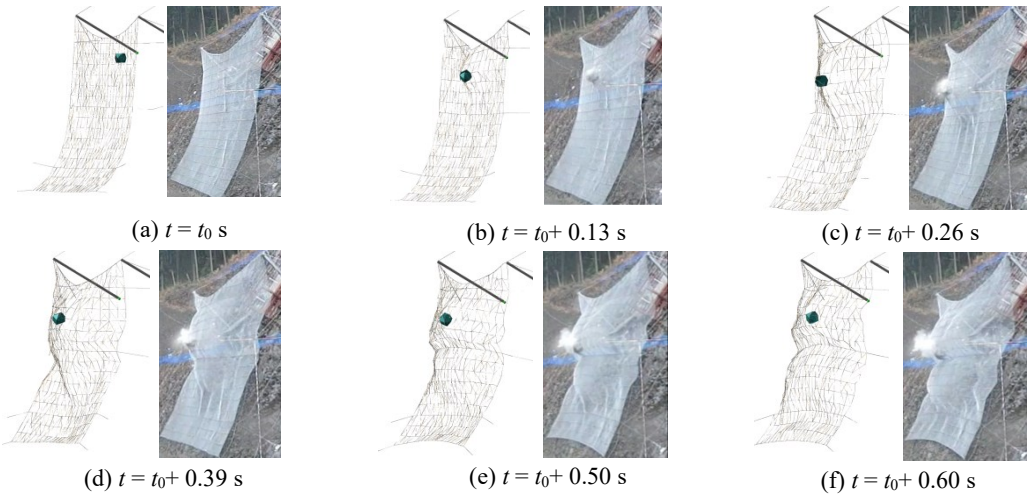

Figure 11. Simultaneous overall deformation response in analysis and experiment

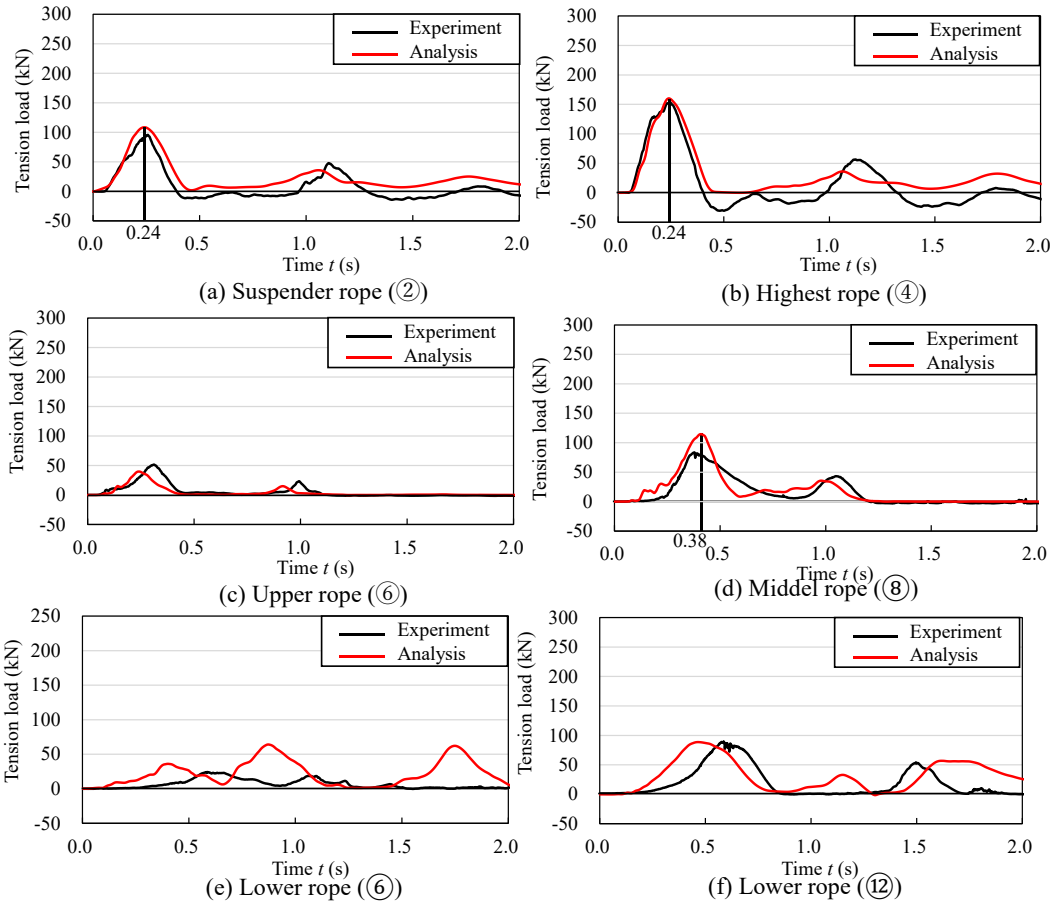

Figure 12. Experimental and analytical time history

arranged diagonally at the intersections of the ropes in the wire mesh section to represent the resistance to lattice-type shear deformation. **Table 2** lists the analysis parameters determined based on the specifications of the wire nets used in the experiment. The axial springs in the

wire mesh section were set to have an axial stiffness approximately 1/1000th of that of a rope with an external diameter of 18 mm in a lattice shape (hereafter referred to as a 3×7, 18φ rope). **Table 2** presents the initial values for the analysis of the falling weight. Additionally, sensitivity analysis was conducted with stiffness values k_n = 1.0×10^8 to 1.0×10^6 and friction coefficients φ = 0 ° to 50 ° to ensure that there is little influence in the friction of the analysis. It was confirmed that the impact of these differences on tension and motion was smaller than that in the presence or absence of the initial rotation.

4.2. Reproduction analysis

Figure 11 shows the overall deformation response at the same time in both the analysis and the experiment. **Figure 11(a)** shows the state before the impact of the falling weight ($t = t_0$ s). **Figure 11(b)** shows the upper part of the net bulging toward the roadside, with no deformation occurring in the lower part of the net. The topmost rope is pulled and curved because of the bulging of the impacted net part, and there is a match between the analysis and experiment ($t = t_0$ + 0.13 s). The deformation is also local, similar to that observed experimentally. **Figure 11(d)** shows that bulging occurs in the lower parts of the middle ropes, which do not collide with the falling weight during the experiment ($t = t_0$ + 0.39 s). The analysis also replicates this behaviour. Furthermore, the extent of the bulging is observed. Subsequently, as shown in **Figures 11(e)** and **(f)**, the bulging in the lower part increases and the analysis can replicate the response deformation of the wire, where the deformation gradually spreads from the vicinity of the collision point.

Figure 12 shows a comparison of the tension–time relationship in both the analysis and the experiment. The analysis values considered the tension at the spring force at the ends, which were at the same position as the ends where the load cells were installed in the experiment. The comparison focuses on the points ②, ④, ⑥, ⑧, ⑩, and ⑫, where the tension at the measurement locations reaches its maximum value. In **Figure 12(a)**, the maximum tension in the suspension rope occurs at $t = t_0$ + 0.24 s, with a difference of 0.01 s from the experiment. The pattern is the same until the second peak. However, looking at the waveform after that, the proposed model shows a smoother peak, which better matches the experiment. In Figure 12(b), the maximum tension in the topmost rope occurs at $t = t_0$ + 0.24 s with a maximum tension of 160 kN, and the proposed model closely matches the experimental value. Subsequently, regardless of the model differences, the second peak is reached earlier than that in the experiment, followed by a decline in the waveform, resulting in a smaller amplitude than that obtained in the experiment. In **Figure 12(c)**, the first and second peaks occur earlier in the upper rope than in the experiment, and it is successfully replicated that the tension is smaller than that of the other ropes, despite being close to the collision point. This is because the topmost rope assumes the tension of the upper rope. Moreover, in the case of the spherical model, there is no tension, indicating that the proposed model provides a better reproduction. As shown in **Figure 12(d)**, the decline after the maximum tension in the middle rope occurs faster than that in the experiment, and the second peak is 0.07 s earlier. While the tension alone shows the same pattern, a comparison with the analysis video revealed that the second tension occurrence is due to the vibration of the net itself after pushing back the falling weight. This indicates that the proposed model requires time for snagging on the net and disengaging,

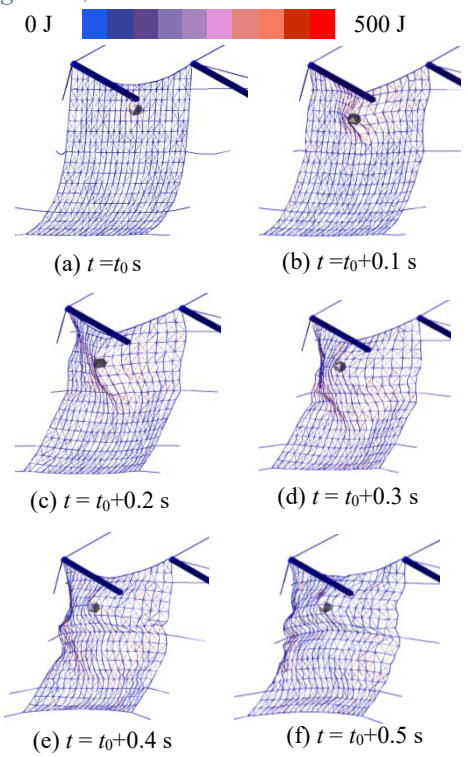

Figure 13. Propagation of kinetic energy

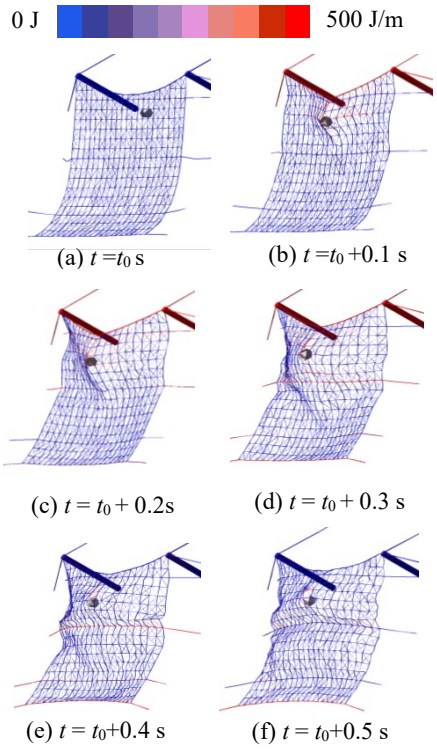

Figure 14. Propagation of deformation

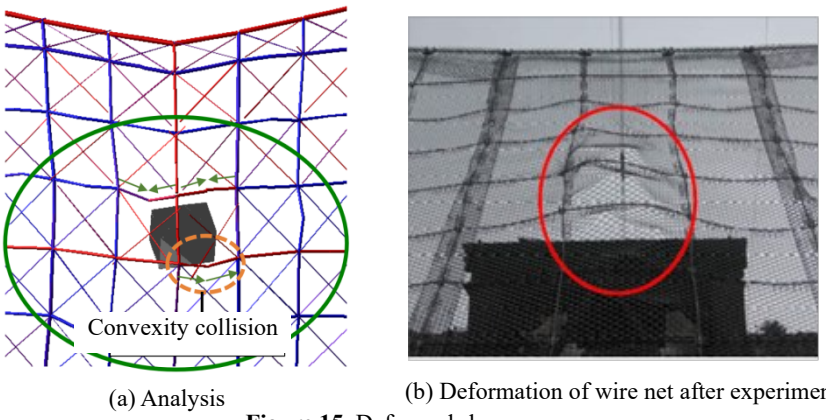

Figure 15. Deformed shape

resulting in the second tension peak occurring closer to the falling process of the weight. Therefore, the proposed model replicates the snagging on the net observed in the experiment. **Figure 12(e)** shows that the lower rope does not match the experimental results well. This is because the waves generated in the upper part propagate and spread below the middle rope, reaching the edge of the net after $t = t_0 + 0.5$ s. Additionally, the rope that generates the maximum load is the same as in the experiment at the same time, and it is found that the differences owing to the model are reflected in the maximum loads of the topmost and middle ropes. This is influenced by the behaviour of the weight falling above the middle rope.

4.3. Energy propagation

Figure 13 shows the transfer of the kinetic energy of the net and the deformation energy of the springs in the proposed model. For the deformation energy of the springs shown in **Figure 14**, the influence of the element length is significant; therefore, the energy per unit length is used for color coding. Each energy source propagates from the collision position of the falling weight to the lower part of the net. Generally, the kinetic energy spreads radially from the upper to the lower part of the net through the wire mesh, while the deformation energy is propagated to the mainline rope simultaneously. Therefore, as shown in **Figure 14**, the deformation energy propagates to the lowest rope before reaching the lower ropes.

Figure 15(a) shows the deformation energy of the falling weight model at a certain time. In the proposed model, energy was concentrated on a specific horizontal rope. This is because snagging on the net occurs, and it affects the propagation of waves. By observing the deformation of the wire net in **Figure 15(b)**, it can be seen that deformation occurs in both the vertical and horizontal ropes, indicating that the model could closely replicate the phenomena occurring in the experiment.

5 Conclusion

This study replicated the load-time relationship by conducting a replication analysis of a collision experiment on a full-scale rockfall protection net using a plane element clump model.

1) The proposed method could replicate the deformation response and tension of each rope in a full-scale rockfall impact experiment on a protection net measuring 15 m in height and 21 m in width.
2) The impact of the falling weight demonstrated that the local deformation induced near the collision site propagated within the rockfall protection net. Additionally, the analysis results confirmed the occurrence of a phenomenon in which the maximum tension in ropes distant from the impact point was delayed by the propagation of waves.
3) The uneven surface shape of the proposed model successfully replicated the snagging effect on the net. This effect led to an increase in the contact time between the net and falling weight, wire, or wire mesh. Consequently, the propagation of energy to the lowest rope was delayed, demonstrating the ability of the model ability to capture the interaction dynamics between the net and the falling weight.

Future research will focus on incorporating a rupture model into the rope constitutive raw material and advancing the modelling of the wire mesh portion, supported by detailed experimental data. In addition, we will continue to study methods for determining the parameters of analysis and creating analytical models to predict the load-bearing capacity of actual structures.

REFERENCES

[1] Disaster management, Cabinet office, Report of disaster management in Japan, 2016.

[2] Road maintenance unit, Civil engineering department, Shimane prefectural office, Report in Shimane prefecture, 2016.

[3] Tazima, T., Maegawa, K., Iwasaki, M., and Kota Kawakami. K., Evaluation of pocket-type rockfall protection nets using shock absorbers by full-scale weight impacts tests, Japan Society of Civil Engineers, Journal of Structural Engineering, 56A, 1088-1100, 2010.

[4] Takahashi, T., Yamamoto, Y., Katsuki, S., and Takamori, K., Full-scale experiments of falling rock protection net, Japan Society of Civil Engineers, Journal of applied mechanics, 69(2), I_787- I_798, 2013.

[5] Hiroaki N., Hisashi, K., Yamaguchi, S., Sasaki, T., and Masato, K., Full-scale experiment of pocket-type rockfall protection nets, Japan Society of Civil Engineers, academic lecture outline collection, 68, 935-936, 2013.

[6] Haraki, D., Katsuki, S., and Tashiro, M., Response analysis of falling rock protection net by using distinct element method with cylinder element, Journal of Japan Society of Civil Engineers, Ser.A1(Structural Engineering & Earthquake Engineering), 65(2), 536-553, 2009.

[7] Naoko, S., Yoshida, H., Tomohiro, F., Kubota, J., and Maekawa, K., Real scale experiment of a falling rock inducement wire-net system with buffer devices, Japan Society of Civil Engineers, Journal of Structural Engineering, 46A, 1853-1864, 2000.

[8] Namba, M., Maekawa, K., Tajima, T., and Yokota, T., A study on full-scale weight impact tests of pocket-type rockfall protective nets using shock absorber, Japan Society of Civil Engineers, academic lecture outline collection, 68, 933-934, 2013.

[9] Iwasaki, E., Syuuji, K., and Masahiro, M., Development of buffer devices for falling rock protection and its performance evaluation, Japan Society of Civil Engineers, Journal of Structural Engineering, 57A, 75-85, 2011.

[10] Sonoda, Y., Yoshihiro, H., and Fukunaga, K., Impact response analysis of wire ring net system using an improved SPH method, Japan Society of Civil Engineers, Journal of Structural Engineering, 57A, 1155-1162, 2011.

[11] Takahashi, T., Yamamoto, Y., Katsuki, S., and Takamori, K., Impact response analysis of falling rock protection net by using 3D-DEM, Japan Society of Civil Engineers, Journal of Structural Engineering, 60A, 1042-1055, 2014.

[12] Toshiyuki Horiguchi, Toshinobu Takahashi, Kiyoshi Takamori, Satoshi Katsuki, Study of limit state estimation for falling rock protection net by using 3D-DEM, Japan Society of Civil Engineers, Journal of Structural Engineering, 63A, 1061-1073，2017.

[13] Horiguchi, T., Shibuya, H., Katsuki, S., Ishikawa, N., and Mizuyama, T., A Basic Study on Protective Steel Structures Against Woody Debris Hazards, International Journal of Protective Structures, 6(2), pp. 191-215, 2015.

EXPERIMENTS ON DEBRIS FLOW IMPACT LOADS USING OPEN SABO DAM SUPPORTED BY CABLES

Yuta Miyahara[1], Toshiyuki Horiguchi[2]

[1]PhD student, National Defense Academy, ed24010@nda.ac.jp

[2] PhD, National Defense Academy, htoshi@nda.ac.jp

Corresponding Author: Yuta Miyahara, PhD student

1-10-20 Hashirimizu, Yokosuka, Kanagawa, Japan, 239-8686

Email: ed24010@nda.ac.jp

ABSTRACT

Recently, natural disasters have occurred frequently owing to abnormal weather conditions. In particular, debris flows have increased in the small valleys adjacent to residential areas. Therefore, easily constructable structures are required for small valleys because construction is difficult owing to the narrow valleys and steep mountains. The use of an open Sabo dam supported by cables has been proposed for no-flow streams or small planed scale of debris flow. However, the behavior of the proposed dam in capturing debris flows is unclear. In this study, the response of the proposed dam to debris flow loads was investigated using an experimental channel and a sliding-dam model supported by cables. The experimental results showed that the debris flow impact loads acting on the dam supported by a cable were constant regardless of the dam weight and did not significantly differ from those of a steel pipe open Sabo dam. However, the load on the cables decreased with an increase in dam weight. Moreover, the impact load on the cables compensated the lack of friction force of the dam model for the debris flow impact load.

Keywords: *no-flow stream, open Sabo dam, cable, water-channel experiment, debris flow load, boulder, driftwood*

1. INTRODUCTION

Localized torrential rain and large typhoons associated with climate change have recently caused numerous landslides in Japan. Among these, the number of cases for small-scale and no-flow streams increased, as shown in **Figure 1**. The area of no-flow streams is relatively small, and sediment transport is unexpected under normal conditions. The streambed gradient upstream is 10° or greater, and the entire stream is a debris-flow-generated zone [1]. During the July 2018 torrential rain disaster, 70 % of the human casualties were attributed to streams with a basin area of 0.05 km^2 or smaller. Only three of the 33 streams in Hiroshima and Ehime that caused the most human casualties had Sabo dams constructed in advance [2, 3]. Therefore, countermeasures are required for no-flow streams.

An open Sabo dam supported by cables (cable-type dam) was proposed as a countermeasure for no-flow streams, as shown in **Figure 2**. The cables are connected to the ground, mountainous areas, and the open Sabo dam to maintain structural stability. Thus, the amount of concrete required for construction is limited, and the structure can be easily constructed. However, no structural form has been analyzed for cable-type dams, and the response of cable-type dams subjected to debris flow loads has not been investigated.

The design load of a Sabo dam comprises the debris flow fluid force at the top and sediment pressure at the bottom, and the dam's stability against overturning, sliding, and ground settlement has been verified. However, because cable-type dams are supported by cables, marginal sliding and overturning are expected. In our previous studies [4, 5], we conducted experiments focusing on the structural stability of Sabo dams under overturning and sliding. However, the interaction between the dam and cables under these two structural conditions must be examined in loading experiments.

In addition, woody debris has frequently caused serious damage to residential areas in recent years. However, the current design load is treated as a boulder debris flow. Woody debris is also assumed to occur in no-flow streams. Thus, the load bearing and capture performances of cable-type dams against driftwood must be considered.

This study investigates the debris flow load on a cable-type dam model using a sliding experimental device. The effects of the dam weight on the debris flow load are discussed, and the loading mechanisms of the cables and dam are clarified. Furthermore, the behaviors of the dam against boulder and woody debris flows are compared.

Figure 1. Disasters caused by no-flow streams [2]

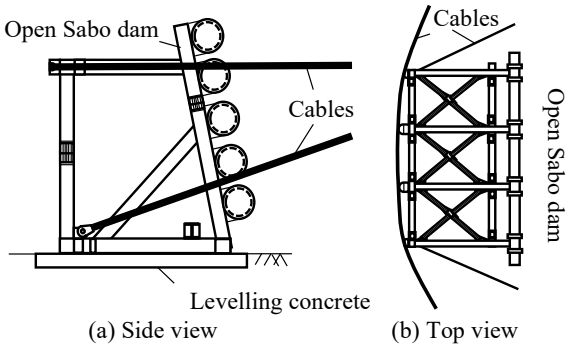

Figure 2. Open Sabo dam supported by cables

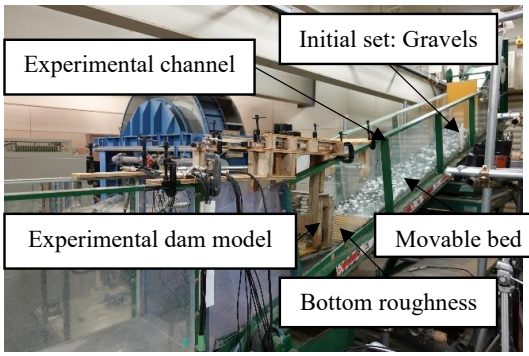

Figure 3. Overview of the experimental device

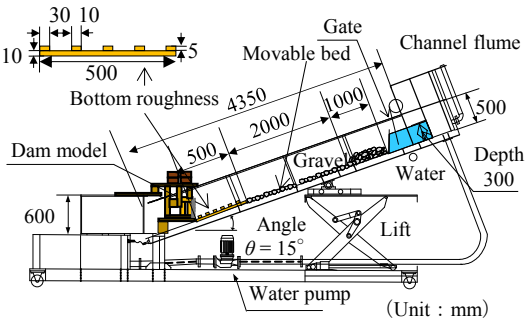

Figure 4. Experimental channel

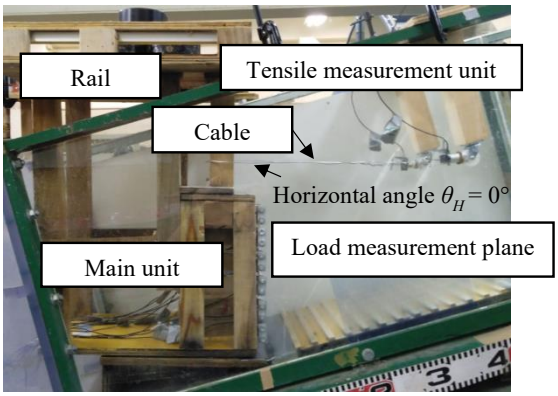

Figure 5. Experimental dam model

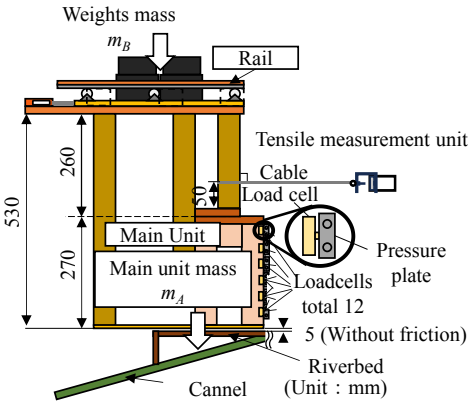

Figure 6. Schematic of the experiment dam model

2. EXPERIMENTAL METHOD

2.1. Experimental device

Figure 3 shows an overview of the experimental setup. The experiment was conducted in a straight channel with a dam model installed at the downstream end. In this study, the experimental scale was set to 1/10 based on Froude's similarity rule.

Figure 4 illustrates the straight channel used in the experiment. A pump was used to generate the debris flow from upstream to downstream. The bed slope was adjusted to mimic a small-scale stream, with a slope of $\theta = 15°$, representing the debris-flow-generation zone. A boulder with bottom roughness featuring 30 mm spacings, 5 mm height, and 10 mm width was placed 500 mm upstream of the dam model.

2.2. Dam model

Figure 5 shows the experimental dam model. The dam model was designed to have a height of 270 mm, which was limited by the constraints of the experimental channel. Based on the Froud similarity rule, the actual scale of the dam model was 2.7 m.

Figure 6 shows a schematic of the experimental dam model. The main unit was suspended from the upper rail to minimize the effect of water on friction, ensuring that only the bottom of the rail was in contact with the main unit. Three rollers were attached to each edge of the upper surface of the main body, which slid along the upper guide rail under a load. The main body of

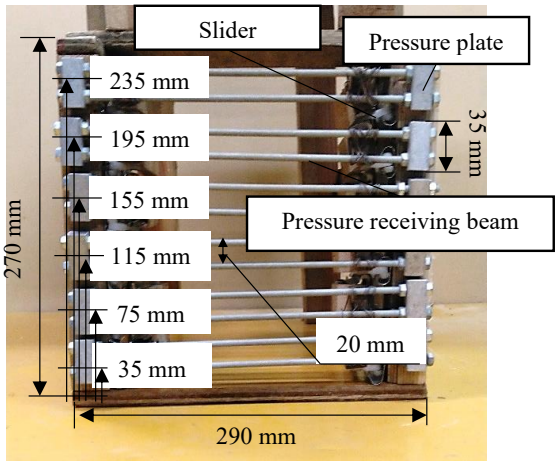

Figure 7. Load measurement plane

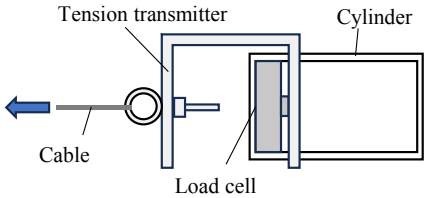

Figure 8. Tensile measurement unit

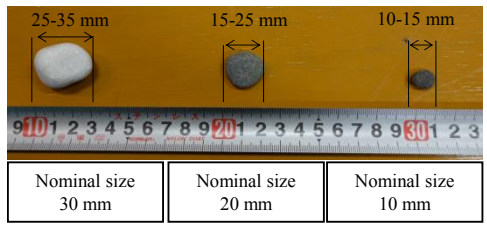

Figure 9. Gravel model

the device was elevated 5 mm above a sloped bed. The mass of the main unit was 8.0 kg, with variable weights added to its upper part.

Figure 7 shows the load measurement plane, which had an effective height of 270 mm, a width of 300 mm, and a spacing of 20 mm between the centers of the cross members. The surface had six stages, and each stage had two load cells (LMB-500-N-P, KYOWA, TOKYO). Therefore, 12 load cells were installed on the measurement surface to measure the debris-flow loads. In this study, the sum of measured load on the measurement surface is called "total load *P.*" An energy-dispersive X-ray spectrometer (EDX-100A, KYOWA, TOKYO) with a sampling frequency of 100 Hz was used [6].

Figure 8 shows the tensile measurement unit. A steel wire with a length of 1,000 mm and diameter of 1.6 mm was used as the cable model. The steel wire did not yield under the debris flow loads. The tensile force on the steel wire was measured by attaching a U-shaped metal to the end of the wire and catching it onto a load cell (LMB-500-N-P, KYOWA, TOKYO) installed in the pipe. In this study, the sum of measured loads with both load cells of the tensile measurement unit is called the "cable reaction force *R*." The steel wire was installed at a horizontal angle of $\theta_H = 0°$ and positioned 50 mm above the top of the dam to avoid the debris flow.

The coefficient of friction between the main unit and rail was calculated in advance by measuring the load at the start of the dam movement when the dam model was pulled by a spring gauge. Five cases with dam's masses ranging from 10 to 50 kg were tested three times each. The coefficient of static friction μ ranged from 0.18 to 0.21. The coefficient of kinetic friction was also measured, and no difference was observed between the static- and kinetic-friction coefficients.

2.3. Debris flow model

As shown in **Figure 9**, The debris flow model was established by mixing three types of gravel with nominal diameters of 10, 20, and 30 mm at a volume ratio of 1:1:1 considering the voids. The specific gravity of the gravel was 2.6, and the dam's mass of the gravel was 60 kg. The

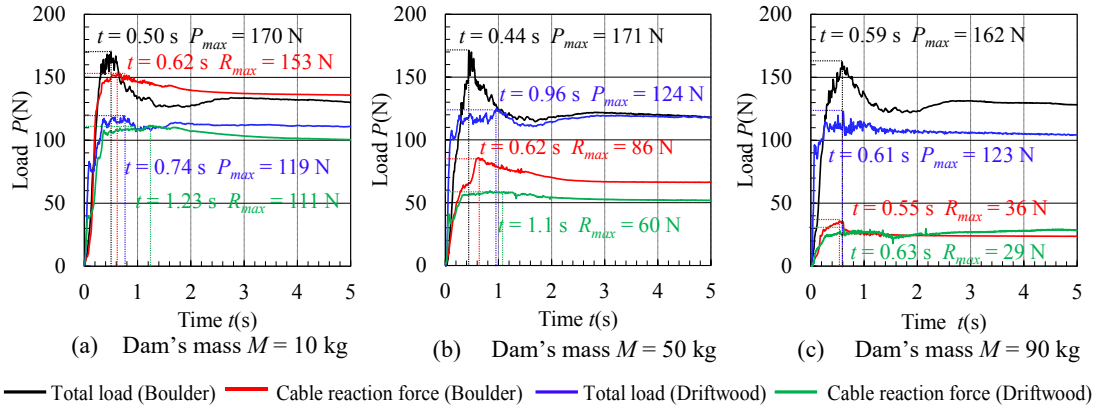

Figure 12. Relationship between load and time

each case, we considered the boulder and driftwood mixed types. The debris-flow conditions were constant, and each test was conducted in triplicate.

3. EXPERIMENTAL RESULTS

3.1. Comparison of relationship between load and time

To investigate the differences in response owing to the dam's mass M, three scenarios with dam's masses M = 10, 50, and 90 kg were considered. **Figure 12** illustrates the response of the dam model to each dam's mass. This highlights the difference between the boulder and driftwood mixed types. A time t was set to t = 0 s, corresponding to the moment when the tip of the debris flow impacted the dam model.

3.1.1 Response against boulder type

First, considering the maximum load P_{max}, which was the maximum value of the total load P for the boulder type, the maximum load $P_{max\text{-}10}$ = 170 N for a dam's mass M = 10 kg, $P_{max\text{-}50}$ = 171 N for a dam's mass M = 50 kg, and $P_{max\text{-}90}$ = 162 N for a dam's mass M = 90 kg. These loads were the same as that for the non-sliding dam [5]. Therefore, the load acting on the open Sabo dam supported by the cable is the same as that acting on the dam with concrete base. Next, considering the maximum reaction force R_{max}, which is the maximum value of reaction force R, the maximum reaction force $R_{max\text{-}10}$ = 153 N for dam's mass M =10 kg, the maximum reaction force $R_{max\text{-}50}$ = 86 N for dam's mass M =50 kg, and the maximum reaction force $R_{max\text{-}90}$ = 36 N for dam's mass M =90 kg, which were 90 %, 50 %, and 22 % of the maximum load P_{max}, respectively.

Second, the difference between the total load P and cable reaction force R is considered. For the dam's mass M = 10 kg, the maximum load $P_{max\text{-}10}$ was reached at t = 0.50 s, at which time the cable reaction force R = 150 N. The difference between the total load P and cable reaction force R was 20 N. This was within the distribution of the friction force f_{10} for a dam's mass M = 10 kg, which was 18–21 N. The maximum reaction force $R_{max\text{-}10}$ was reached at t = 0.62 s, at which time the total load P = 160 N. The difference between the total load P and cable reaction force R was 7 N, which was smaller than the friction force f_{10}. The cable reaction force R

converged with the total load P, and the total gravel-pressure load P_s = 130 N and convergence-reaction force R_s = 135 N, which were similar. Here, the total gravel-pressure load P_s and convergence reaction force R_s refer to the total load P and cable reaction force R, which converged after t = 5.0 s.

For the dam's mass M = 50 kg, the maximum load $P_{max\text{-}50}$ was reached at t = 0.44 s, at which time the cable reaction force R = 66 N. The difference between the total load P and cable reaction force R was 105 N. This was similar to the distribution of the friction force f_{50} for a dam's mass M = 50 kg, which was 88–103 N. The maximum reaction force $R_{max\text{-}50}$ was reached at t = 0.62 s, at which time the total load P = 141 N. The difference between the total load P and cable reaction force R was 55 N, which was smaller than the friction force f_{50}. The total gravel pressure load P_s = 117 N and convergence reaction force R_s = 66 N after t = 5.0 s. The difference between the two forces was 51 N.

For the dam's mass M = 90 kg, the maximum load $P_{max\text{-}90}$ was reached at t = 0.59 s, at which time the cable reaction force R = 35 N. The difference between the total load P and cable reaction force R was 127 N. This was smaller than the distribution of the friction force f_{90} for a dam's mass M = 50 kg, which was 168–185 N. The maximum reaction force $R_{max\text{-}90}$ was reached at t = 0.55 s, at which time the total load P = 151 N. The difference between the total load P and cable reaction force R was 115 N, which was smaller than the friction force f_{90}. The cable reaction force R reached its maximum value earlier than the total load P, unlike the cases of M = 10 and 50 kg. This may be because the dam's mass M = 90 kg could bear most of the frictional force f_{90}; however, a small amount of tension was generated at the time of the debris flow impact. The total gravel-pressure load P_s = 104 N and the convergence reaction force R_s = 29 N after t = 5.0 s. The difference between these values was 75 N.

The above results indicate that the larger the total load M, the smaller the cable reaction force R generated. When the total load P reached its maximum value, the frictional force f also reached its maximum value, and cable tension was considered to be generated to compensate the shortfall. The cable reaction force R reached the maximum load marginally later than the total load P and converged with P.

3.1.2 Response against driftwood mixed type

Next, considering the maximum load $P_{max\text{-}w}$ for the driftwood mixed type, the maximum load $P_{max\text{-}w10}$ = 119 N for a dam's mass M = 10 kg, $P_{max\text{-}w50}$ = 124 N for a dam's mass M = 50 kg, and $P_{max\text{-}w90}$ = 123 N for a dam's mass M = 90 kg. The loads did not exhibit significant differences. Considering the maximum reaction force R_{max}, the maximum reaction force $R_{max\text{-}w10}$ = 111 N for dam's mass M =10 kg, the maximum reaction force $R_{max\text{-}w50}$ = 60 N for dam's mass M =50 kg, and the maximum reaction force $R_{max\text{-}w90}$ = 29 N for dam's mass M = 90 kg, which were 93 %, 48 %, and 24 % of the maximum load P_{max}, respectively.

Subsequently, the difference between the total load P and cable reaction force R was considered. For the dam's mass M = 10 kg, the maximum load $P_{max\text{-}w10}$ was reached at t = 0.74 s, at which time the cable reaction force R = 108 N. The difference between the total load P and cable reaction force R was 11 N, which was smaller than the distribution of the friction force f_{10} for a dam's mass M = 10 kg. The maximum reaction force $R_{max\text{-}w10}$ was reached at t = 1.2 s, at which

time the total load P = 108 N. The total gravel-pressure load P_s = 110 N, and the convergence reaction force R_s = 100 N after t = 5.0 s. Although R_s was smaller than P_s, their values were generally similar.

For the dam's mass M = 50 kg, the maximum load $P_{max\text{-}w50}$ was reached at t = 0.96 s, at which time the cable reaction force R = 58 N. The difference between the total load P and cable reaction force R was 66 N, which was smaller than the distribution of the friction force f_{50} for a dam's mass M = 50 kg. The maximum reaction force $R_{max\text{-}w50}$ was reached at t = 1.1 s, at which time the total load P = 120 N. The difference between the total load P and cable reaction force R was 62 N, which was smaller than the friction force f_{50}. The total gravel-pressure load P_s = 118 N and the convergence-reaction force R_s = 52 N after t = 5.0 s. The difference between these values was 66 N.

For the dam's mass M = 90 kg, the maximum load $P_{max\text{-}w90}$ was reached at t = 0.61 s, at which time the cable reaction force R = 25 N. The difference between the total load P and cable reaction force R was 98 N, which was smaller than the distribution of the friction force f_{90} for a dam's mass M = 50 kg. The maximum reaction force $R_{max\text{-}w90}$ was reached at t = 0.63 s, at which time the total load P = 109 N. The difference between the total load P and cable reaction force R was 80 N, which was smaller than the friction force f_{90}. The total gravel pressure load P_s = 104 N and the convergence reaction force R_s = 28 N after t = 5.0 s. The difference between these values was 76 N.

In the driftwood mixed type, as in the boulder type, the total load P was generally constant regardless of the dam's mass M; however, the maximum load P_{max} was smaller than that in the boulder type. This trend is consistent with that reported in previous studies [7]. However, the ratio of the maximum reaction force R_{max} to the maximum load P_{max} was similar to that of the boulder type. The difference between the total load P and cable reaction force R was smaller than the maximum frictional force f, unlike in the boulder type. A comparison of the graphs of the boulder and driftwood mixed types shows no-peak in the driftwood mixed type, and the time at which the maximum load P_{max} was reached was later. This may be because the preceding driftwood acted as a cushioning material.

3.2. Comparison of load distribution

The load distribution at the time when load P_l generated at each stage reached its maximum value is discussed. Difference in the total load P wasn't observed for the dam's mass M. Therefore, the load distribution for a dam's mass of M = 50 kg is shown as a representative example.

3.2.1 Load distribution of boulder type

Figure 13 shows the load distribution based on the time history for a dam's mass of M = 50 kg. The blue line shows the load distribution in the direction of each step in front of the dam. The final gravel-pressure distribution at t = 5.0 s is indicated by a red line. **Table 2** lists the load in each step P_l, total load P, cable reaction force R and the difference between total load P and cable reaction force R when each step reaches its maximum value. First, the first and second stages reached their maximum values at t = 0.12 and 0.18 s with loads P_l = 33 and 45 N, respectively. The total loads at these times were P = 71 and 89 N and the cable reaction forces

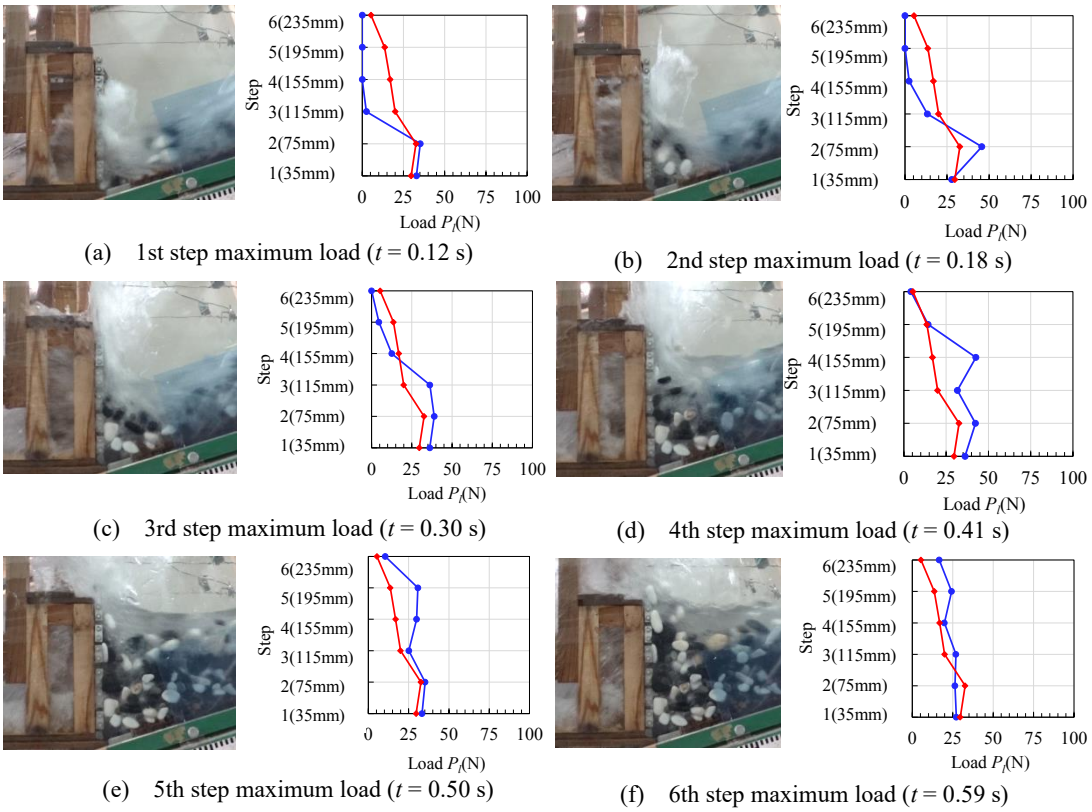

(a) 1st step maximum load (t = 0.12 s)

(b) 2nd step maximum load (t = 0.18 s)

(c) 3rd step maximum load (t = 0.30 s)

(d) 4th step maximum load (t = 0.41 s)

(e) 5th step maximum load (t = 0.50 s)

(f) 6th step maximum load (t = 0.59 s)

Figure 13. Load distribution of boulder type (Dam's mass M = 50 kg)

Table 2. Load values (Figure 13.)

Figure 13	Time t	P_l						P	R	P - R
		1st	2nd	3rd	4th	5th	6th			
(a)	0.12 s	33 N	35 N	3 N	0 N	0 N	0 N	71 N	28 N	43 N
(b)	0.18 s	28 N	45 N	13 N	3 N	0 N	0 N	89 N	41 N	48 N
(c)	0.30s	36 N	38 N	36 N	13 N	5 N	0 N	128 N	60 N	68 N
(d)	0.41 s	36 N	42 N	32 N	42 N	15 N	4 N	171 N	64 N	107 N
(e)	0.50 s	33 N	35 N	25 N	30 N	31 N	10 N	164 N	69 N	95 N
(f)	0.59 s	27 N	26 N	27 N	20 N	24 N	17 N	141 N	85 N	56 N

were R = 28 and 41 N, respectively. The differences between these values were 43 and 48 N, respectively, indicating that friction bore a large proportion of the load. The third stage reached its maximum value at t = 0.30 s, with a load P_l = 36 N. The total load P = 128 N and the cable reaction force R = 60 N. The difference between these values was 68 N. The fourth and fifth stages reached their maximum values at t = 0.41 and 0.50 s with loads P_l = 42 and 31 N, respectively. The total loads were P = 171 and 164 N and the cable reaction forces R = 64 and 69 N, respectively. The differences between them were 107 and 95 N, respectively, which were similar to the friction force f_{50}. The sixth stage reached its maximum value at t = 0.59 s with a load P_l = 17 N. The total load P = 141 N and the cable reaction force R = 85 N. The difference was 56 N, indicating that friction bore a smaller share of the load.

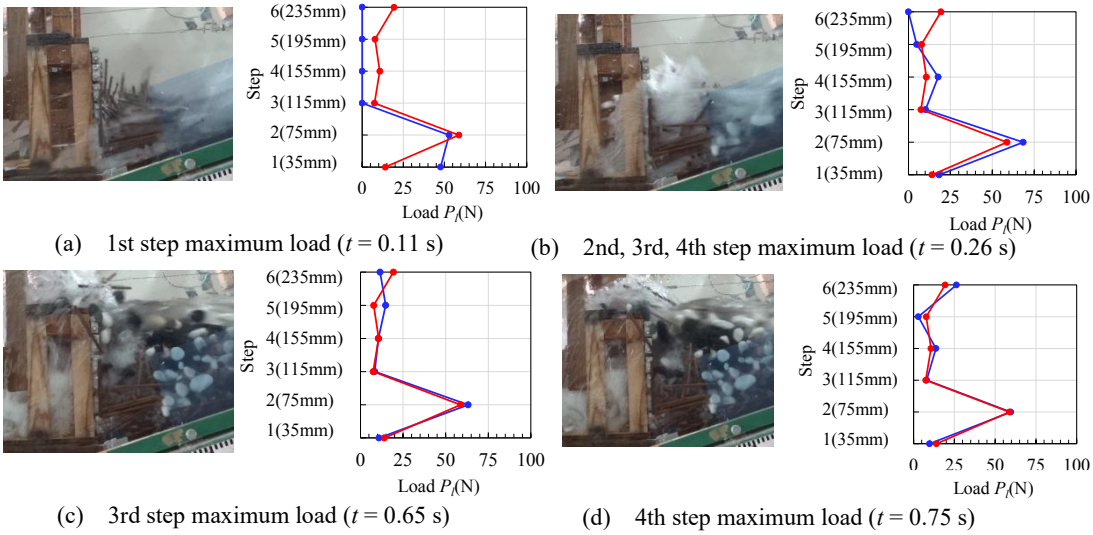

(a) 1st step maximum load (t = 0.11 s) (b) 2nd, 3rd, 4th step maximum load (t = 0.26 s)

(c) 3rd step maximum load (t = 0.65 s) (d) 4th step maximum load (t = 0.75 s)

Figure 14. Load distribution of driftwood mixed type (Dam's mass M = 50 kg)

Table 3. Load values (Figure 14.)

Figure 14	Time t	P_l						P	R	P - R
		1st	2nd	3rd	4th	5th	6th			
(a)	0.11 s	47 N	54 N	0 N	0 N	0 N	0 N	101 N	35 N	66 N
(b)	0.26 s	19 N	68 N	10 N	17 N	5 N	0 N	119 N	50 N	69 N
(c)	0.65s	11 N	63 N	8 N	11 N	14 N	12 N	119 N	57 N	62 N
(d)	0.75 s	10 N	60 N	8 N	13 N	3 N	26 N	120 N	58 N	62 N

These results indicate that the total load P reached its maximum value when the fourth and fifth stages reached their maximum values. Next, considering the cable reaction force R, when the first stage reached its maximum value, a small proportion of R was generated by friction. The cable reaction force R increased gradually after the maximum frictional force f was reached. In other words, the response of the cable reaction force can be considered to be greatly influenced by the friction force f. The maximum value decreased as the number of stages increased; however, this was owing to the loss of velocity caused by the collision between the gravel deposited ahead and the gravel following it [10, 11].

3.2.2 Load distribution of driftwood mixed type

Figure 14 shows the load distribution based on the time history for a dam's mass of M = 50 kg; **Table 3** lists the load in each step P_l, total load P, cable reaction force R and the difference between total load P and cable reaction force R when each step reaches its maximum value. The first stage reached its maximum value at t = 0.11 s, with a load P_l = 47 N on the first stage. The total load P = 101 N and the cable reaction force R = 35 N. The difference between these values was 66 N. The second, third, and fourth stages reached their maximum values simultaneously at t = 0.26 s, with loads P_l = 68, 10, and 17 N, respectively. The total load P = 119 N and the cable reaction force R = 50 N. The difference between these values was 69 N. The 5th and 6th stages then reached their maximum values at t = 0.65 and 0.75 s, with loads P_l = 14 and 11 N, respectively. The total loads were P = 119 and 120 N and the cable reaction

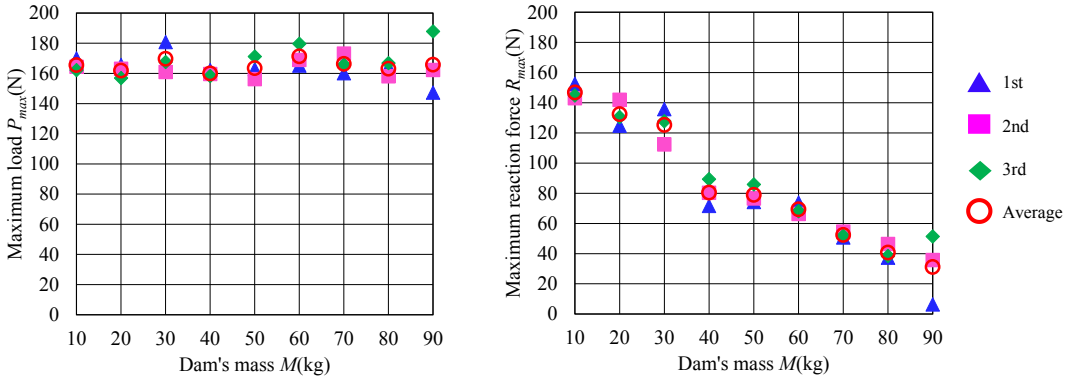

(a) Maximum load P_{max} (b) Maximum reaction force R_{max}

Figure 15. Relationship between load and dam's mass (Boulder type)

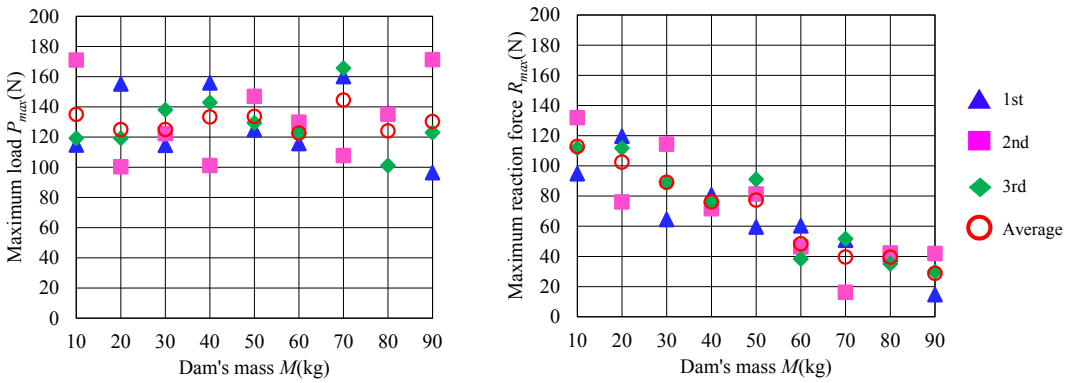

(a) Maximum load P_{max} (b) Maximum reaction force R_{max}

Figure 16. Relationship between load and dam's mass (Driftwood mixed type)

forces were R = 57 and 58 N, respectively. The differences between these values were 62 N in both cases.

In the case of driftwood, the maximum load tended to be reached simultaneously in the second, third, and fourth stages after the first stage impact because the driftwood flowed down in a lump prior to the gravel. The gravel-pressure distribution showed that the load increased as one moved downward in the boulder type. However, in the case of the driftwood mixed type, the load at the second level was more prominent, exhibiting a different distribution from that of the boulder type. This may be because, unlike gravel, driftwood entangles itself in the gravel during sedimentation, resulting in a large gap and a space where it is not in contact with the cross members. The fifth and sixth stages tended to reach their maximum values later than the boulder type; however, this was because the gravel must be deposited upstream of the driftwood before it passes over the deposited driftwood.

3.3. Relationship between load and dam's mass

3.3.1 Result of boulder type

Figure 15 shows the relationship between the load and dam's mass for the boulder type. The maximum load P_{max} was distributed between 160 and 180 N, regardless of the dam's mass M.

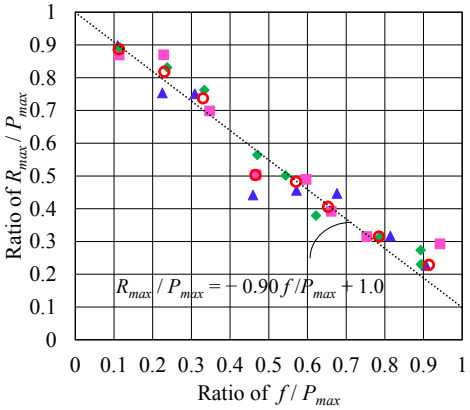

Figure 17. Relationship between the ratios (Boulder type)

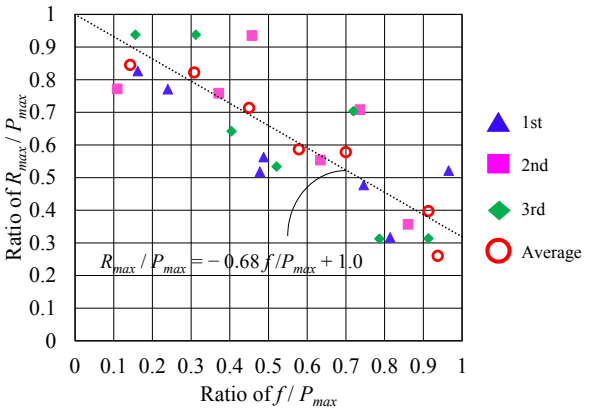

Figure 18. Relationship between the ratios (Driftwood mixed type)

The average value of the maximum load P_{max} on a non-sliding dam was 170 N [5]; therefore, we can assume that an open Sabo dam supported by cables is subjected to the same debris flow action as a non-sliding dam. The maximum reaction force R decreased as the dam's mass M increased.

3.3.2 Result of driftwood mixed type

Figure 16 shows the relationship between the load and dam's mass for driftwood mixed type. The maximum load P_{max} was distributed between 100 and 170 N, which had a larger variation than that of the boulder type, and the values were lower than those of the boulder type. The maximum reaction force R also decreased as the dam's mass M increased.

3.4. Burdened load of cable

Based on the previous experimental results, the burdened load of the cable decreased as the dam's mass M increased. Furthermore, the magnitude of the load borne by the cable is affected by the frictional force. However, quantitatively evaluating the burdened load of cables is difficult because the experimental results varied. Therefore, the ratio of the maximum reaction force R_{max} to the maximum load P_{max} and the ratio of the maximum friction force f to the maximum load P_{max} were taken and made non-dimensional to quantitatively evaluate the effect of the maximum friction force f. Here, the average of the measured values, $\mu = 0.19$, was used to calculate the maximum friction force f for each dam's mass M.

3.4.1 Burdened load of cable against boulder type

Figure 17 shows the relationship between the boulder type ratios. The graph shows that the maximum reaction force R_{max} compensated the lack of maximum friction force f with respect to the maximum load P_{max}. Using all the experimental values, the following equation was obtained by linear approximation:

$$R_{max} / P_{max} = -0.90\, f / P_{max} + 1.0 \tag{1a}$$

$$R_{max} = -0.90\, f + P_{max}. \tag{1b}$$

This equation enables the estimation of the maximum reaction force R_{max} produced against the maximum load P_{max} if the maximum frictional force f is known. The coefficient of

determination for this approximate equation was $R^2 = 0.95$. In other words, assuming a constant boulder type load, as shown in **Figure 17** by the red line, the area shown in blue is borne by the cable, and the area shown in green is borne by the friction force, depending on the change in the mass of the dam.

3.4.2 Burdened load of cable against driftwood mixed type

Figure 18 shows the relationship between the ratio of the driftwood mixed type. The graph shows that the ratio of the maximum reaction force R_{max} to the maximum load P_{max} was greater than that of the boulder type. Using all the experimental values, the following equation was obtained by linear approximation:

$$R_{max} / P_{max} = -0.68 f / P_{max} + 1.0 \quad (2a)$$

$$R_{max} = -0.68 f + P_{max}. \quad (2b)$$

This equation also indicates that the burdened load of the cable against the driftwood mixed type was greater than that against the boulder type. This was because the driftwood mixed type flowed down as a lump of driftwood, and the increase in the load at the time of first impact was larger than that of the boulder type. However, because the total load P was smaller for the driftwood mixed type than for the boulder type, the cable reaction force R was also smaller. Furthermore, quantitatively evaluating the burdened load of cables against the driftwood mixed type is difficult owing to large variability. Therefore, when designing a cable-type dam, the cable should be able to compensate the lack of frictional force of the dam against the boulder type flow.

4. CONCLUSION

This study investigated the response of an open Sabo dam model supported by cables during the capture of debris flows. The experimental device was a sliding dam model supported by a cable. The response of the cable, frictional force of the dam model, and load were organized using the dam's mass M as a parameter. The results are summarized as follows.

1) The displacement of the dam could be suppressed by installing cables in the sliding-dam model. The debris flow load acting on the dam model supported by cables was the same as that acting on the non-sliding dam.

2) A comparison of the maximum load P_{max} between the boulder and driftwood mixed types showed that the maximum load P_{max} in the driftwood mixed type was smaller than that in the boulder type owing to the cushioning effect of the driftwood. The cable reaction force R was also smaller for the boulder type; however, no significant difference was observed in the ratio of the maximum load P_{max} to the maximum reaction force R_{max}.

3) The maximum reaction force R_{max} decreased as the dam's mass M increased.

4) The maximum friction force f affected the maximum reaction force R_{max}. The maximum reaction force R_{max} could be estimated from the ratio of the maximum frictional force f to the maximum load P_{max} for the boulder type.

5) The burden ratio of the cable against the woody debris load was larger than that against the boulder-type load. However, the total load *P* was smaller for the driftwood mixed type than for the boulder type, and the cable reaction force *R* was also smaller; therefore, when designing the proposed dam, the burden load of the cables can be considered as a load that compensates the lack of frictional force of the dam against the load of the boulder type flow.

REFERENCES

[1] Ministry of Land, Infrastructure, Transport and Tourism. (2022). *Muryuusuikeiryu taisaku ni kakaru gizyutsutekiryuiziko [Technical considerations for no-flow stream measures]*. https://www.mlit.go.jp/river/shishin_guideline/sabo/murymuryuusuikei_ryuuizikou_r0403.pdf.

[2] Ministry of Land, Infrastructure, Transport and Tourism. (2018). *Heisei 30nen 7gatsu gohu saigai niyoru dosyasaigai gaiyo [Summary of Landslide Disaster Caused by Torrential Rainfall in July,2018]*. https://www.mlit.go.jp/river/sabo/jirei/h30dosha/H30_07gouu_gaiyou1807311800.pdf.

[3] Ministry of Land, Infrastructure, Transport and Tourism. (2019). *Zikkousei noaru hinan wo kakuho surutameno dosyasaigai taisaku no arikata ni tsuite, houkokusyo [Landslide countermeasures to ensure effective evacuation, report]*. https://www.mlit.go.jp/river/sabo/committee_jikkousei/190529/hokokusyo.pdf.

[4] Komatsu, Y., Horiguchi, T., & Katsuki, S. (2021). Experimental study on debris flow impact load against overturning limit of steel open type Sabo dam. *Journal of Structural Engineering*, 67A, 838-848.

[5] Miyahara, Y., Horiguchi, T., Takeya, K., & Mantoku, M. (2023). Influence of sliding phenomena on debris flow load acting on an open Sabo dam. *Journal of Structural Engineering*, 69A, 1128-1139.

[6] Horiguchi, T. (2022). *Sabo kozobutsu ni sayo suru dosekiryu kazyu zikken no keisokuyoryo ni tsuite [Measurement method of debris flow load acting on Sabo structures]*. *Journal of the Japan Society of Erosion Control Engineering*, 75(2), 23-28.

[7] Miyahara, Y., Horiguchi, T., & Komatsu, Y. (2023), Influence of approach shape of debris flow on impact load subjected to open Sabo dam under an overturning experiment of open Sabo dam. *E3S Web of Conference*, 415(DFHM8), 02013. https://doi.org/10.1051/e3sconf/202341502013

[8] Shibuya, H., Katsuki, S., Kokuryo, H., Ohsumi, H., & Ishikawa, N. (2012). Experimental study of load for steel frame check dam caused by debris flow with woody debris. *Journal of the Japan Society of Erosion Control Engineering*, 65(1), 54-61.

[9] Horiguchi, T., Goda, A., Shimakawa, O., & Yamada, T. (2020). Impact load of debris acted a steel pipe open Sabo dam. *Journal of Japan Society of Civil EngineeringA2(Applied Mechanics)*, 76(2), 325-326.

[10] Horiguchi, T. & Komatsu, Y. (2019). Method to evaluate the effect of inclination angle of steel open-type check dam on debris flow impact load. *International Journal of Protective Structures*, 10(1), 95-115.

[11] Shimakawa, O., Horiguchi, T., Komatsu, Y., & Katsuki, S. (2019). Debris flow load reduction effect on front inclination angle of open Sabo dam possessed by DEM. *Journal of Japan Society of Civil EngineeringA2(Applied Mechanics)*, 75(2), 175-185.

FEATURES OF PRESTRESSED TENDONS WITH CATERNARY-CANTILEVER SHAPE AND ITS INFLUENCE ON FRICTIOIN LOSS AND INVERTED ARCH DEFLECTION

Jianshe Xu[1], Ran Ma[2], and Wei Wang[3]

[1] Ph. D, School of Environment and Architecture, University of Shanghai for Science and Technology, buildxu@163.com

[2] Postgraduate, School of Environment and Architecture, University of Shanghai for Science and Technology, 861958037@qq.com

[3] Ph. D, State Key Laboratory of Disaster Reduction in Civil Engineering & Department of Structural Engineering, Tongji University, weiwang@tongji.edu.cn

Corresponding Author: Jianshe Xu, Ph. D,

No. 516 Jungong Road, Shanghai, China, 200093

Email: buildxu@163.com

ABSTRACT

Post-tensioned unbonded prestressed tendons conforming to parabolic shapes are widely used in prestressed concrete slabs. Due to construction deviations, even if numerous supporting reinforcements are introduced along the tendon at intervals to control the vertical positions, the final shape of the curve may differ significantly from a real parabola. This paper proposes a catenary-cantilever curve shape, allowing unbonded prestressed tendons to be located by controlling only the top and bottom points, instead of numerous shape-governing points. By solving the curve equations, we undertake a comparative analysis between the shape features of the catenary-cantilever curve and parabola curve. Subsequently, the friction loss of the prestressed tendons are obtained. The results show that for common slab spans, although some geometrical characteristics of the catenary-cantilever curve, e. g., the position of the inflection point and the height ratio of the curve, differ significantly from those of a parabola, the friction loss discrepancy of the two shapes is not considerable and can be neglected in the total prestress loss. The deflection analysis conducted using ANSYS reveals a striking resemblance in the inverted arch deflections of the two shapes, implying that the balance load effects of the prestressed tendons with the two shapes are close.

Keywords: *unbonded prestressing, prestressed slab, curved tendon, catenary line, prestress friction loss, inverted arch deflection.*

1. INTRODUCTION

Curvilinear prestressed tendons are widely used in prestressed concrete floor structures. In comparison with straight line prestressed tendons, curvilinear prestressed tendons can adjust their vertical position according to the internal force diagram of the member and can produce an ideal "balanced-load" in the opposite direction of the vertical load. With respect to curve shapes of prestressed tendons, parabola curves are widely used at present, as shown in Figure 1(a). Other shapes were also reported in recent years. Park [1] presented bi-circular curves. The numerical example demonstrated that the use of the bi-circular curve is quite effective for the tendon profile, and the proposed methodology to compute the internal bending moments can be an efficient tool for the analysis of the prestressed concrete flat slabs. However, detailed comparisons between the bi-circular curve and traditional parabola curve were not made. References [2-7] proposed new prestressed tendon arrangements for various structures or members such as simple beams, continuous beam bridges, concrete flat slabs, T-beams strengthened with externally prestressed tendons, external prestressing self-centering frames, prestressed reticulated mega-structures, which made progress in improving mechanical performance and facilitating construction, but nearly all of the tendon shapes in these literatures are fold lines. In the respect of prestress loss, Yu [8] and Zhang [9] improved the precise formula for anchoring loss of curved steel strands in post tensioned beams and pointed out the unreasonable aspects in current bridge design specifications. Zhao [10] systematically provided a segmented linear calculation method for friction and anchorage prestress loss by considering the linear characteristics of spatial prestressed tendons. Except for prestress loss, tendon profiles may have influences on other structural behaviors. Kim [11] investigated the behavior of indeterminate prestressed concrete T beams with two different unbonded tendon profiles, which induced different hyperstatic moment at the support. Pandimani [12] conducted nonlinear simulations of unbonded prestressed concrete beams by use of FEA software ANSYS and proposed a model that can effectively predict the cracking of the concrete, the stress of the member and prestressed tendons, and the load-deflection curves of the beams. Le [13] and Pang [14] studied the performance of prestressed concrete beams under different parameters and conditions by numerical simulation. Toader [15] presented an analytical design approach for post-tensioned concrete slabs with unguided tendons. The performance of the prestress slab when unguided tendons are used instead of the classical guided ones decreased by 12%. Abbas [16] studied the optimization algorithm of the bonded post-tensioned one-way concrete slab and a significant reduction in the area of post-tensioned tendons was reached which was approximately 22%. Only V-shaped line tendons, however, were taken into account.

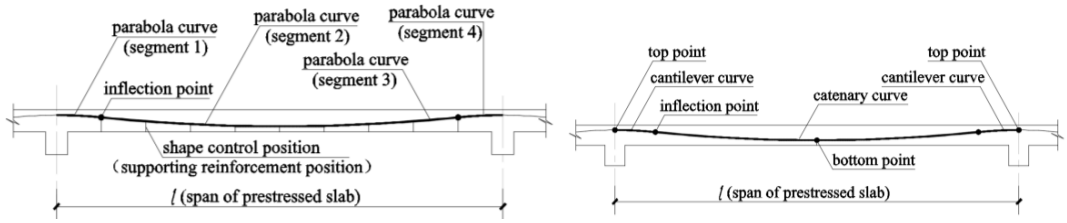

(a) Parabola curve shape. (b) Catenary-cantilever curve shape.

Figure 1. Two types of prestressed tendon curve shapes.

During the construction process of prestressed concrete slabs, to attain the desired curve shape of the tendons, shape control points, where supporting reinforcements are usually placed, are introduced along the tendon at predetermined intervals (e.g., 1 m) to control the vertical positions. Given that both the concrete slab thickness and the overall rise of the tendon curve (i.e. the vertical distance of the top and bottom point) are relatively minor, the curve shape of the prestressed tendon is very sensitive to the vertical position deviation of each point of the curve. Consider, for example, a prestressed slab spanning 8 m and measuring 200 mm in thickness. If the top and bottom points of the curve are located at 50 mm beneath the slab's upper surface and 50 mm above the slab's lower surface, respectively, the overall rise of the curve is 200 – 50 – 50 = 100 mm. For such a curve rise, it can be calculated that the maximum calculated vertical position difference between a parabola curve and a bi-circular curve is only 0.012 mm. By contrast, deviations in the vertical positioning of prestressed tendons encountered in actual construction process are significantly more substantial. For instance, adhering to Chinese specifications, the permissible deviation in the alignment of prestressed tendons within members with a thicknesses under 300 mm is stipulated at 5 mm [17]. This means that even if the vertical positon deviation in prestressed tendons can meet the specification requirements, the final shape of the curve is probably far different from the expected profile. In this paper, a novel curve shape is proposed based on a practice in which only the top point (usually near the bearing position) and bottom point (usually near mid span) are controlled. For this practice, the middle segment of the curve drops naturally, forming a catenary curve, while the segments at both ends adopt cantilever configurations, as shown in Figure 1(b). Advantages of this practice includes enhanced convenience, rapid construction pace, and high efficiency. Nonetheless, the implications of this particular curve profile on the mechanical behavior of prestressed slabs remains largely unexplored. This study initiates with the derivation of the equations governing the catenary-cantilever (hereinafter referred to as C-C) curve. Subsequently, comparisons are drawn between this curve and the traditional parabola curve with respect to parameters like catenary rise, the position of the inflection point, prestress friction loss, and the inverted arch deflection. These assessments aim to ascertain the feasibility and potential application domains for this innovative curve shape.

2. ESTABLISHMENT AND SOLUTION OF CURVE EQUATIONS

2.1 Basic assumptions and force diagrams

The following assumptions are adopted for the C-C curve illustrated in Figure 1(b):

(1) The cantilever segment is fixed at the end;

(2) The middle segment is a catenary curve;

(3) There is an inflection point between the catenary and cantilever segments;

(4) The prestressed tendon is a single unbonded prestressed tendon.

Based on the above assumptions and considering symmetry, a half-span prestressed tendon is taken as the object of our study, the span of which is $l/2$. The difference in vertical positions between the top (at the bearing position) and bottom points is f. As shown in Figure 2, the horizontal projection lengths of the catenary segment and cantilever segment are x_1 and x_2,

respectively. Their vertical projection lengths are y_1 and y_2, respectively. The lengths of the catenary and cantilever segments are L_1 and L_2, respectively. The loads on the half-span prestressed tendon include:

(1) q, the self-weight of the prestressed tendon (kN/m);

(2) R, the tension force of the prestressed tendon at the bottom point;

(3) The internal force of the prestressed tendon at the top point.

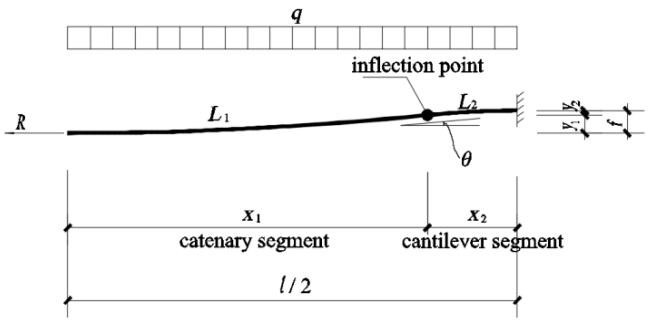

Figure 2. Diagram of half-span prestressed tendon.

The force diagram of the catenary segment and cantilever segment in Figure 2 can be divided into Figure 3(a) and Figure 3(b). The forces acting on the catenary segment consists of q and the tension forces R and T_1 at the ends. The forces acting on the cantilever segment comprise its own weight, the tension force T_1 of the prestressed tendon at the inflection point, the weight transferred from the catenary segment to the cantilever segment (amounting to qL_1) and the reaction force at the bearing point.

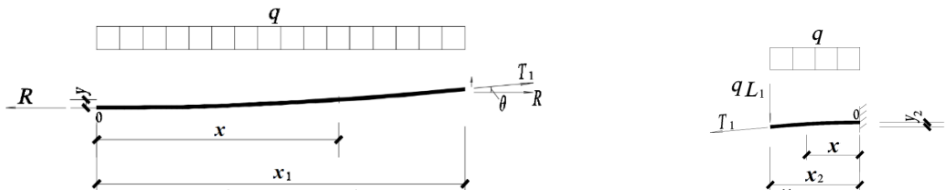

(a) Catenary segment. (b) cantilever segment.

Figure 3. Force diagram of the catenary segment and the cantilever segment.

2.2 Establishment of catenary segment and cantilever segment equations

For the catenary segment in Figure 3(a), the tangent direction at the bottom point is horizontal. The catenary curve equation can be written as follows [18]:

$$y = a \cdot \left[\cosh\left(x/a\right) - 1\right] \tag{1}$$

The length measured from any point in the catenary curve to the bottom point is

$$L = a \cdot \sinh\left(x/a\right) \tag{2}$$

The tension force at any point in the catenary curve is

$$T = R \cdot \cosh\left(x/a\right) \tag{3}$$

where $a = R/q$

From formula (1), when $x = x_1$, the height of the catenary segment y becomes

$$y_1 = a \cdot \left[\cosh\left(x_1/a\right) - 1\right] \tag{4}$$

From formula (2), the total length of the catenary segment is

$$L_1 = a \cdot \sinh\left(x_1/a\right) \tag{5}$$

According to Figure 3(b), the deflection at any point in the cantilever segment can be expressed by (note that the coordinates x, y in Figures 3(a) and 3(b) are in a separate system)

$$y = \frac{qx^2}{12EI}\left[3x_2^2 - 2xx_2 + \frac{1}{2}x^2 + 2L_1\left(3x_2 - x\right)\right] \tag{6}$$

When $x = x_2$, the height of cantilever segment y is

$$y_2 = \frac{q}{8EI}x_2^4 + \frac{qL_1x_2^3}{3EI} \tag{7}$$

Substituting (5) into (6) and (7) yields

$$y = \frac{qx^2}{12EI}\left[3x_2^2 - 2xx_2 + \frac{1}{2}x^2 + 2a\left(3x_2 - x\right)\sinh\left(x_1/a\right)\right] \tag{8}$$

$$y_2 = \frac{q}{8EI}x_2^4 + \frac{qax_2^3}{3EI}\sinh\left(x_1/a\right) \tag{9}$$

2.4 Deformation compatibility condition

For Figures 3 and 4, the following deformation compatibility conditions are considered:

(1) The sum of the total rise of the catenary segment and cantilever segment equals to f, i.e.

$$y_1 + y_2 = f \tag{10}$$

(2) The sum of horizontal length of the catenary segment and the cantilever segment is equal to half of the slab span, i.e.

$$x_1 + x_2 = l/2 \tag{11}$$

(3) At the inflection point, the curve angles of the catenary segment and cantilever segment are identical. Specifically, their first derivatives are identical. From formulas (1) and (8), the following is obtained:

$$\left\{a \cdot \left[\cosh\left(\frac{x_1}{a}\right) - 1\right]\right\}'\Big|_{x=x_2} = \left\{\frac{qx^2}{12EI}\left[3x_2^2 - 2xx_2 + \frac{1}{2}x^2 + 2a\left(3x_2 - x\right)\sinh\left(\frac{x_1}{a}\right)\right]\right\}'\Big|_{x=x_2}$$ and

then

$$\sinh\left(x_1/a\right) = \frac{qx_2^3}{6EI - 3qax_2^2} \tag{12}$$

2.5 Solving method

Equations (4), (9), (10), (11) and (12) constitute an equation group with five variables, i.e., a, x_1, x_2, y_1, y_2 (for a certain prestressed slab, f, l, and q are given). Since the numbers of equations and unknown variables are equal, the equations can be solved. However, formulas (4), (9), and (12) are transcendental equations and must be solved by numerical methods.

3 SOLUTION RESULT AND COMPARISON WITH PARABOLA CURVE FEATURE

3.1 Position of the inflection point

The relative position of the inflection point can be expressed by the ratio $\eta = x_2/l$, where x_2 denotes the horizontal projection length of the cantilever segment and l is the slab span. Prestressed slabs with commonly employed spans of 4−12 m are calculated. Given that the total rises (f values) of the prestressed tendons are $l/40$, $l/50$, and $l/60$, respectively, the values of η (deduced from x_2, which can be solved from the equations in section 2), are shown in Figure 4(a). It can be seen that for various rise-to-span ratios (f/l), the relative position of the inflection point changes significantly with increasing slab span. When the slab span is 4 m, the value of η is 0.34−0.47, and when the slab span reaches 12 m, the value of η is only 0.06−0.07. However, for the conventional four-segment parabola curve, η = 0.10−0.15 is usually assumed.

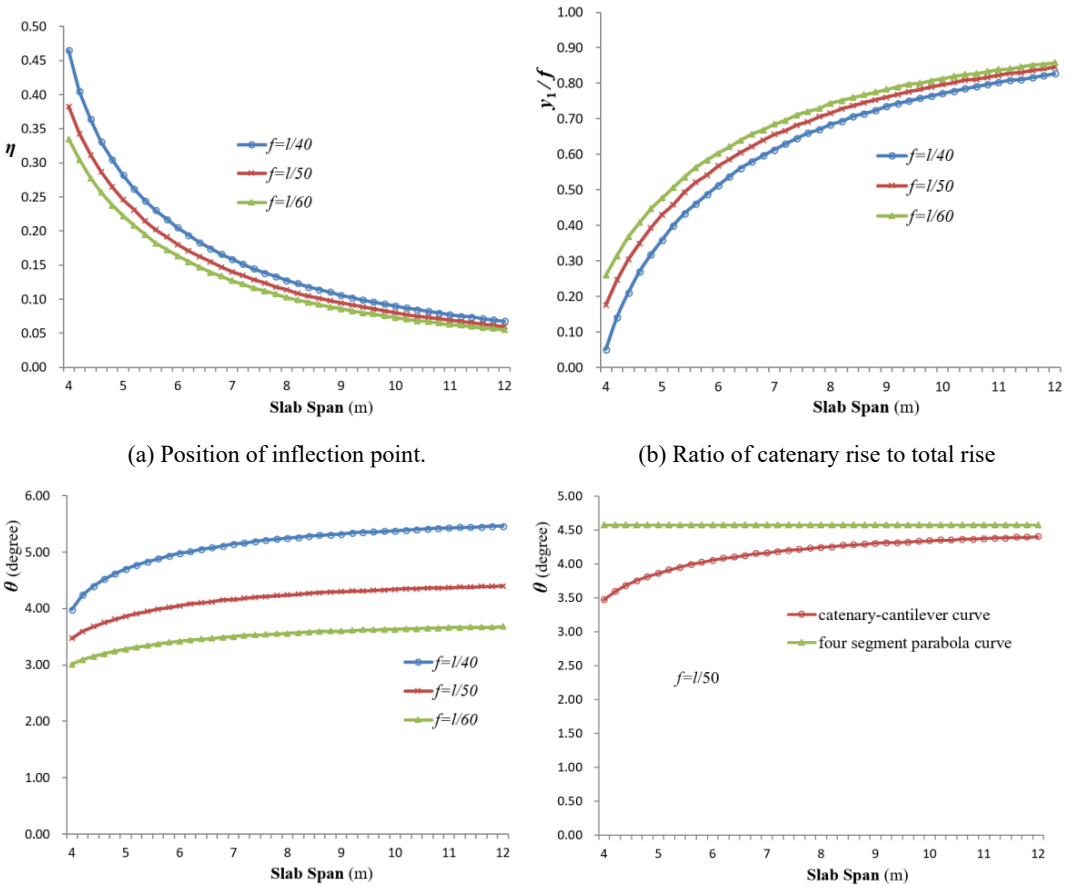

(a) Position of inflection point.

(b) Ratio of catenary rise to total rise

(c) Curve angle at the inflection point.

(d) Comparison of curve angle at the inflection point.

Figure 4. Features of C-C curve for slab spans 4−12 m.

3.2 Proportion of catenary rise

The rises of the catenary segment and cantilever segment are designated as y_1 and y_2, respectively, which together compose the total rise f. The ratio y_1/f, i.e., the proportion of the catenary segment rise to the total rise, is shown in Figure 4(b). It is obvious that for various rise-to-span ratios (f/l), the proportion of the catenary segment rise to the total rise increases with increasing slab span. For a rise-to-span ratio of 1/50, ratio y_1/f is only 17.6% when the slab span is 4 m, but increases dramatically to 84.6% when the slab span reaches 12 m. For four-segment parabola parabolic tendons, the proportion of the middle segment parabola rise to the total rise is 70−80%, which is quite different from that of the aforementioned proportion.

3.3 Curve angle at the inflection point

The curve angle θ is shown in Figure 4(c), which indicates that for C-C tendons, the curve angle at the inflection point is limited, and the maximum angle is not higher than 5.5°. For the same slab span, the curve slope increases with increasing total rise of the tendon. For a prestressed slab with a span of 6 m, the value of θ is 3.4° when $f = l/60$, and increases to 5° when $f = l/40$. The rate of growth is 47%.

The curve angle at the inflection point of the C-C curve shape is contrasted with parabolic shape in Figure 4(d), which illustrated only an $f = l/50$ case. It can be shown that the angle of the latter is greater than that the former, but the difference is not more than 1°. With an increase in slab span, the two angles tend to be close.

4 COMPARISON OF PRESTRESS FRICTION LOSSES AND INVERTED ARCH DEFLECTION

4.1 Calculation of prestress friction loss

The calculation formula for the prestress loss attributable to friction between the tendon and the duct's wall is as follows [19]:

$$\sigma_{l2} = \sigma_{\text{con}}\left(1 - \frac{1}{e^{\kappa x + \mu\theta}}\right) \tag{13}$$

where x denotes the duct length measured from the tension end to the calculation section; θ is tangent angle difference between the tension end and the calculation section of the curve; κ represents the friction coefficient with consideration of the local deviation within a 1-meter segment of the duct; σ_{con} is the tension control stress. For unboned tendons, the friction coefficient κ is typically set to 0.004; μ is the coefficient of friction between the prestressed tendon and the duct's wall. The value of μ is customarily assumed as 0.09 for unbonded tendon applications.

4.2 The comparison of prestress losses of prestressed tendons

In this study, the prestressed tendon is assumed to be a single steel strand, with a strength grade of 1860 N/mm^2 (f_{ptk} = 1860 N/mm^2). A value of 0.7f_{ptk} (i.e., 1302 N/mm^2) is taken as the tension control stress σ_{con}. Within the range of commonly used slab spans, the prestress friction loss is shown in Figure 5(a). In case that σ_{con} differs from 0.7f_{ptk}, the value of σ_{l2} can be ascertained through the application of a linear correlation.

Figure 5(a) shows that for various total rises, the friction loss σ_{l2} of a prestressed tendon conforming to a C-C profile is linear with the slab span. In addition, for a certain slab span, σ_{l2} increases with increases in the total rise f. When f increases from $l/60$ to $l/40$, the friction loss experiences an approximate elevation of 15 N/mm^2.

Figures 5(b)−5(d) present a comparative assessment of the prestress friction losses, highlighting differences between those configured in C-C and parabola curve shapes, with a range of total rises taken into account.

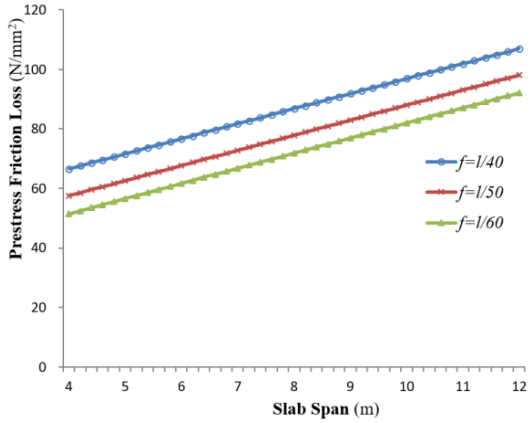

(a) Friction loss of C-C curve tendons

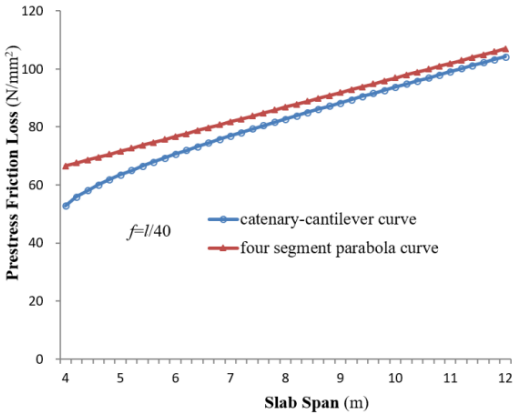

(b) Friction loss of two tendon shapes (while $f = l/40$) .

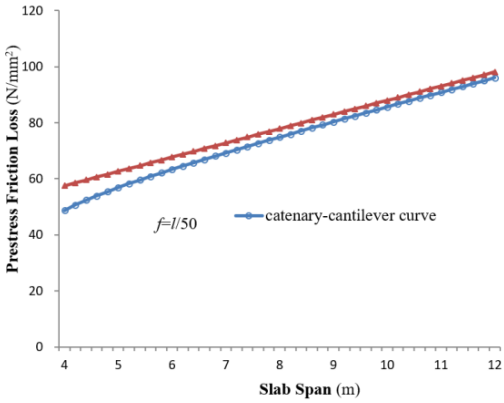

(c) Friction loss of two tendon shapes (while $f = l/50$).

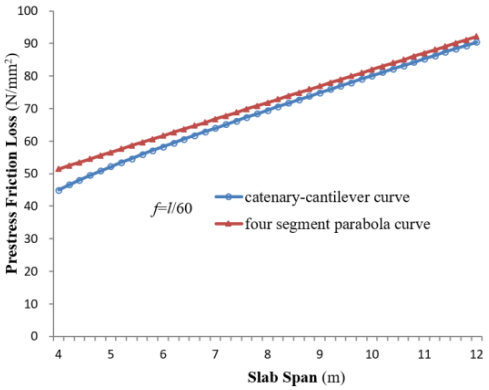

(d) Friction loss of two tendon shapes (while $f = l/60$).

Figure 5. Comparisons of friction loss of prestressed tendons for slab spans of 4−12 m.

The followings can be derived from Figures 5(b)−5(d):

(1) In the range of typically employed slab spans, the friction loss of a prestressed tendon configured in a C-C shape is observed to be less compared to that of a tendon following a four-segment parabola profile.

(2) When the span of the prestressed slab is relatively small, there is a discernible discrepancy in the friction loss of prestressed tendons conforming to the two shapes. The maximum discrepancy can attain 13.8 N/mm^2, equating to 26.1% of the friction loss. However, this variance diminished as the slab span extends. Specifically, upon reaching a span of 12 m, the

distinction shrinks dramatically to a mere 2.7 N/mm^2, accounting for only 2.6% of the prestress friction loss.

(3) Suppose that the total prestress loss of a prestressed slab amounts to 20% of σ_{con} [20]. In instances where the span of the slab is relatively compact, the difference in friction losses of prestressed tendons adopting either the parabolic or C-C configurations constitutes roughly 5.3% of this total prestress loss. As the slab span increases substantially, the difference decreases to no more than 1.0% of the total prestress loss, and can be ignored in practical engineering.

4.3 The comparison of inverted arch deflections caused by prestressed tendons

For prestressed tendon with a parabola profile, the balanced-load generated by prestressing manifests as a uniformly distributed load (or, in the case of multi-segmented parabola, as multiple segments of uniformly distributed loads). When the tendon shifts to adapt a C-C shape, expressing the corresponding balanced-load in a straightforward mathematical formulation becomes notably more challenging. Considering that different balanced-loads induce different inverted arch deflections of the concrete slab, a comparative analysis between the balanced loads corresponding to the two shapes can be facilitated through the observation of the deflections simulated by numerical analysis software Ansys.

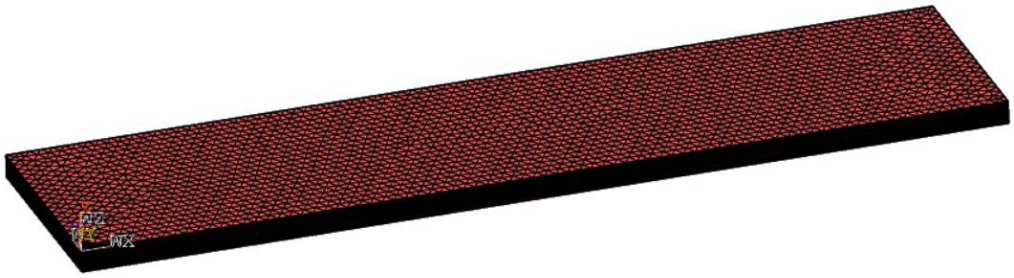

Figure 6. Overall meshing of FEA model.

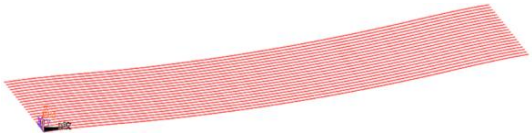

Figure 7. Prestressed tendons in FEA model.

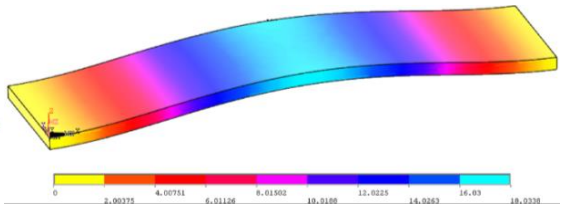

Figure 8. Inverted arch deflection contour.

Prestressed concrete plates with spans 4 m and 8 m, respectively, are taken as examples. The corresponding plate thicknesses are 120 mm and 200 mm, respectively. The overall rises of the prestressed tendons are 75 mm and 155 mm, respectively. The concrete plate is modelled using three-dimensional element type SOLID65, with element sizes set to 5 mm in the thickness direction and 100 mm within the plate plane, respectively. The prestressed tendons, arranged at a spacing of 100 mm, are modelled using element type LINK8, with the element size set to 50 mm. The elastic modulus and Poisson's ratio of the concrete are set to 3.45×10^4 N/mm^2 and 0.3, respectively, while those of the prestressed tendons are set to 1.95×10^5 N/mm^2 and 0.2, respectively. This calculation solely concerns the inverted arch deflection in the elastic stage, hence, no material parameters for the plastic stage are defined. The area and self-weight of each

prestressed tendon are set to 139 mm and 1.2 kg/m, respectively. The constraint conditions of the plate are set to hinged at both ends. Prestressing is applied by using initial strain method, and the magnitude of the prestressing force for each prestressed tendon is 180 kN. The strain, calculated by dividing this force by the area of the prestressed tendon, is defined as one of the real constants of the prestressed tendon. The connections between the elements of the prestressed tendons and concrete slab are simulated by defining constraint equations. Figure 6 shows the overall meshing of the model, among which the prestressed tendons are shown in Figure 7. The schematic diagram of the inverted arch deflection contour is shown in Figure 8. The comparison of the inverted arch deflection values is shown in Table 1.

Table 1. Comparison of inverted arch deflections corresponding to two prestressed tendon shapes

Plate span /m	Inverted arch deflection /mm	
	for C-C shape	for parabola shape
4	7.36	8.32
8	18.07	18.15

Table 1 shows that the inverted arch deflection for C-C shape is marginally less than parabola shape when the slab span is relatively compact, but the two deflections tend to be nearly identical with the increase of the span. For a slab span of 8m, the discrepancy between the two deformations is only 0.5%, which implies that the balanced-load induced by prestressed tendons assuming a C-C shape is nearly equivalent to that induced by a parabolic shape.

5 CONCLUSIONS

By analysing the features of prestressed tendons with catenary-cantilever shape in concrete slabs and contrasting the finding with the corresponding items of four-segment parabola-shaped tendons, several conclusions can be drawn.

(1) Prestressed curve tendons with the two aforementioned shapes exhibit a substantial discrepancy in the inflection point positions and a significant difference in the proportion of curve segment rise.

(2) The variation between the curve angles of the two shapes is not considerable.

(3) Calculation of friction losses of the prestressed tendons reveals that the discrepancy between the friction losses of prestressed tendons with the two shapes is insignificant, and constitutes a minor proportion of the total prestress loss of prestressed tendons within the scope of commonly employed slab spans. In the context of practical engineering, this discrepancy can be disregarded.

(4) The inverted arch deflection induced by prestressed tendons assuming a catenary-cantilever shape is close to that induced by a parabolic shape, especially for a slab with relatively large span.

It is worth noting that the findings and conclusions drawn herein are specifically pertinent to prestressed concrete slabs and should not be extrapolated to prestressed concrete beams.

References

[1] Park, S. , & Kim K. (2004). A new design method for prestressed concrete continuous flat slabs. *Struct Method for Tall Spec Build*, 13(4), 265-276.

[2] Mohamed, G., Eisa, A., Purcz, P., Ručinský, R., El-Feky, M. (2022). Effect of External Tendon Profile on Improving Structural Performance of RC Beams. *Buildings*, 12(6), 789.

[3] Zhou, X., Fu, C., Hou, W., Guo, H., Hu, W. (2021). Comparison of the Mechanical Properties of Different Tendon Profiles with External Prestressed Reinforcement. *Technical Gazette*, 28(4), 1338-1344.

[4] Mohammed, A., Taysi, N. (2017). Modelling of bonded and unbonded post-tensioned concrete flat slabs under flexural and thermal loading. *Structural Engineering and Mechanics*, 62(5), 595-606.

[5] Zou, J., Huang, Y., Feng, W., Chen, Y., Huang, Y. (2019). Experimental study on flexural behavior of concrete T-beams strengthened with externally prestressed tendons. *Mathematical Biosciences and Engineering*, 16(6), 6962-6974.

[6] Dai, G., Lu, L., & Xu, Y. (2017). Optimization analysis of prestressed reinforcement layout scheme for external prestressed self-resetting structure. *Structural Engineers*, 33(02), 26-33.

[7] He, Y., Wang, J., & Zhou, X. (2017). Research on cable layout of prestressed giant grid Structure. *Journal of Hunan University (Natural Science Edition)*, 44(07), 1-6.

[8] Yu, J. (2018). Study on prestress loss of curved prestressed steel beam [D]. Lanzhou Jiaotong University.

[9] Zhang, Y., Guo, C., & Zhang, Y. (2018). Accurate analysis of anchorage loss of curved steel beam in post-tensioned prestressed concrete beam. *China Journal of Highway and Transport*, 31(01), 67-73+90.

[10] Zhao, Y., & Huang, D. (2005). Analysis of friction and anchorage prestress loss of space curved reinforcement. *Building Structure*, 2005 (04), 31-34.

[11] Kim, U., Ballu, E., Hong, S., et al. (2022). Structural behavior of continuous two-span prestressed concrete T beams with different tendon profiles. *PCI Journal*, 67(4).

[12] Pandimani, Ponnada, M., & Geddada, Y. (2022). Finite-element modeling of partially prestressed concrete beams with unbonded tendon under monotonic loadings. *Journal of Engineering, Design and Technology*, 22(1): 235-256.

[13] Le, T., Pham, T., & Hao, H. (2020). Numerical study on the flexural performance of precast segmental concrete beams with unbonded internal steel tendons. *Construction and Building Materials*, 248, 118362.

[14] Pang, M., Liu, X., Dong, Y., et al. (2022). Numerical assessment on bonded and unbonded prestressed concrete beams. *Buildings*, 12(10), 1658.

[15] Toader, T., Kiss Z., Tere, S., Puskás, A. (2021). An analytical design approach for post-tensioned concrete slabs with unguided tendons. *IOP Conference Series: Materials Science and Engineering,* 1141(2021), 012013.

[16] Abbas H., Nildem T., Dia N., Ali K. (2017). Finite element analysis and optimization of bonded post-tensioned concrete slabs. Cogent Engineering, 4(1), 1341288

[17] *Technical Specification for Concrete Structures Prestressed with Unbonded Tendons*. (2016). Beijing: China Building Industry Press.

[18] Wang, D., & Liu, J. (2007). Application of the catenary curve's equation in common condition. *Ship&Ocean Engineering*, 36(3), 26-28.

[19] *Code for Design of Concrete Structures*. (2010). Beijing: China Building Industry Press.

[20] Lin, T. (1983) *Design of Prestressed Concrete Structures*[M]. Beijing: China Railway Publishing House

EQUIVALENT STATIC PRESSURE DESIGN PROCEDURE FOR INTERNAL PRESSURE DUE TO EXTERNAL BLAST

Ashok Malhotra[1], Scott McFadden[2] and Babak Mashayekhi[3]

[1] Senior Principal, WSP Canada, Ashok.Malhotra@wsp.com

[2] Senior Engineer, WSP Canada, Scott.Mcfadden@wsp.com

[3] Senior Engineer, WSP Canada, Babak.Mashayekhi@wsp.com

Corresponding Author: Ashok Malhotra, P.Eng.

2611 Queensview Drive, Suite 300, Ottawa, Ontario, Canada, K2B 8K2

Email: Ashok.Malhotra@wsp.com

ABSTRACT

Current methods for calculating interior pressure in a building caused by an external blast, which penetrates through broken windows or openings, are often intricate and time intensive. The UFC 3-340 [1] procedure is notably laborious, and its results are applicable only within specific parameters of explosive weight and standoffs. Utilizing Computational Fluid Dynamics (CFD) techniques necessitates specialized software and entails significant time investment to generate a pressure-time history for design purposes, given the highly variable and transient nature of interior blast pressures.

A simplified procedure is proposed in this paper, based on converting the dynamic pressure and impulse to an Equivalent Static Pressure (ESP).

In the proposed procedure, when an explosion occurs outside a building with openings, and windows shatter, the blast pressure infiltrates, compressing the air within the interior space. This compression reduces the volume of the air, consequently elevating the air pressure within the interior space above atmospheric pressure. To implement this approach, the dynamic blast pressure and impulse resulting from the Design Basis Threat (DBT) are converted into an Equivalent Static Pressure (ESP). This conversion is facilitated through charts provided in the book "Introduction to Structural Dynamics [2]." The method involves modeling the air within the room as an equivalent Single Degree of Freedom (SDOF) system, with its mass and stiffness determined based on the properties of air within a confined space.

Keywords: *Blast, Dynamics, Pressure, Internal Pressure, External Blast, Equivalent Static Pressure, Blast Pressure Leakage.*

INTRODUCTION

General information

Current methods for calculating interior pressure in a building caused by an external blast, which penetrates through broken windows or openings, are often intricate and time intensive. The UFC 3-340 [1] procedure is notably laborious, and its results are applicable only within specific parameters of explosive weight and standoffs. Utilizing Computational Fluid Dynamics (CFD) techniques necessitates specialized software and entails significant time investment to generate a pressure-time history for design purposes, given the highly variable and transient nature of interior blast pressures.

A simplified procedure is proposed in this paper, based on converting the dynamic pressure and impulse to an Equivalent Static Pressure (ESP). This procedure results in a static pressure which can be directly employed for preliminary designs facilitating rapid assessment of the feasibility of various design configurations. Additionally, it serves as a valuable tool for validating the outcomes of more intricate methods, allowing for efficient cross-verification of results.

EQUIVALENT STATIC PRESSURE DESIGN PROCEDURE

This procedure relies on converting the dynamic blast pressure attributable to the Design Basis Threat (DBT) into an Equivalent Static Pressure (ESP). The dynamic blast pressure can be reflected pressure or side-on pressure depending upon the relative location of the DBT and the wall opening. Subsequently, the ESP and the Bulk Modulus of the air within the room are utilized to ascertain the reduction in air volume caused by the ESP. According to Boyle's Law, this reduction in air volume corresponds to a proportional increase in air pressure within the room. This augmented air pressure is denoted as the Design Static Pressure, employed to evaluate the response of the structural system such as the walls, floor or ceiling of the room. Nevertheless, the propagation of ESP throughout the air volume within the room constitutes a complex phenomenon, necessitating adjustments to the ESP to accommodate this intricacy. These adjustments will be elucidated further in the subsequent sections of the article.

The Bulk Modulus (BM) of a material quantifies the change in volume in response to applied pressure. Mathematically, it is represented as the ratio of the change in pressure (Δp) to the corresponding change in volume or volumetric strain (εv):

$$Bulk\ Modulus\ (BM) = \frac{\Delta p}{\varepsilon v} \tag{1}$$

For air as an example, the Bulk Modulus is approximately 142×10^3 N/m^2.

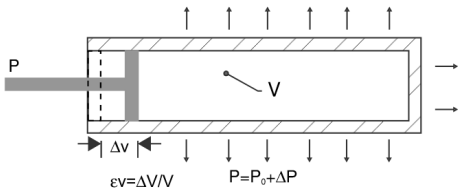

Figure 1. Volumetric strain and change in pressure in a sealed container

To illustrate, consider a scenario where a uniform pressure of P=14.2×10^3 N/m^2 is exerted upon a volume of air confined within a sealed container of initial volume V_0 and pressure P_0. The volume of air will contract by a factor of:

$$\varepsilon v = \frac{P}{BM} \text{ or } \varepsilon v = \frac{14.2\times10^3}{142\times10^3} = 0.1$$

resulting in a new volume of $V=0.9V_0$. By Boyle's Law, the increase in pressure is inversely proportional to the reduction in volume by $(\frac{1}{1-\varepsilon v})$, yielding a new pressure of:

$$P = \frac{V_0}{V}P_0 = 1.11P_0$$

For instance, envision an airtight room initially filled with air at an absolute atmospheric pressure of P_a=101.3×10^3 N/m^2. If a pressure of 14.2×10^3 N/m^2 is applied at an opening, the resultant absolute pressure will be 1.11 times the initial pressure (1.11 × 101.3×10^3 N/m^2), indicating an increase of 11% of the initial pressure, or 11.2×10^3 N/m^2. Consequently, the absolute pressure of the air within the room will now be 112.5×10^3 N/m^2.

To establish our procedure, we first define several key parameters as follows:

L = inside length of the space under consideration, m

W = inside width, this is the wall with an opening, m

H = inside height, m

A = interior face area of wall with openings, W x H; m^2

Z = area of wall opening, m^2

P_r= Peak blast pressure, N/m^2

t_d = duration of positive blast phase; ms

T = natural period of the air mass in the direction of length, i.e. "L"

The natural period (T) of a unit footprint of a column of air can be calculated using the formula:

$$T = 2\pi\sqrt{\frac{K_{LM}\,Mass}{k}} \tag{2}$$

where:

K_{LM}, is the Load-mass factor = 0.67

Mass, is the mass of a column of air with the length of L and a unit area footprint (1 m^2),

$$Mass = density \times volume \tag{3}$$

Considering air density being 1.225 kg/m^3 the mass for the column of air can be calculated as: Mass = 1.225 $kg/m^3 \times L \times 1\ m^2$

k in equation (2), represents the stiffness of the column of air with the length of L. In other words, this is the force required to deform the air volume by one cubic meter. If the sides of the container are considered rigid, only the length will be reduced by one meter, thereby the stiffness can be calculated as:

$$k = \frac{force}{displacement} = \frac{Area \times BM}{L} \tag{4}$$

$k = 1 \times BM/L = 142 \times 10^3/L$ (N/m)

Assuming the air column being a linear elastic body, a Dynamic Load Factor (DLF) can be used to establish an equivalent static pressure. Refer to Figure 2.7 of "Introduction to Structural Dynamics" [2], or to Figure B1 of CAN/CSA -852-18 [3], adapted as Figure 2 herein in order to calculate DLF.

Therefore, the procedure can be established as follows:

a) Calculate mass = 1.225 $kg/m^3 \times L \times 1\ m^2 = 1.225L\ N.s^2/m$,

b) Calculate stiffness, $k = 142 \times 10^3 / L$ N/m,

c) Calculate natural period (T) of the air volume, using Eq. (2),

d) Determine Peak Blast Pressure (P_r) and Positive Phase Duration (t_d) based on the Design Basis Threat (DBT) using commercially available software or other means,

e) Calculate t_d/T,

f) Read the value of DLF from Figure 2 below,

g) Calculate Equivalent Static Pressure (ESP):

$$ESP = P_r \times DLF \tag{5}$$

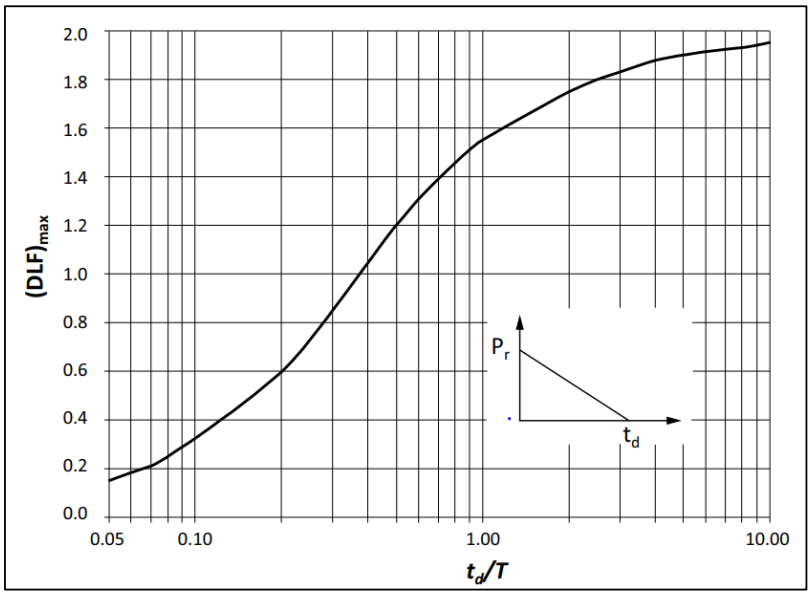

Figure 2. Variation of maximum DLF with t_d /T ratio (Adapted from CAN/CSA-852-18 [3])

h) Calculate Average Equivalent Static Pressure (AESP):

When Equivalent Static Pressure (ESP) is applied to the inside air mass, the propagation of pressure throughout the air volume occurs in a complex manner. Typically, pressure is highest near the opening and decreases as it propagates inward. To simplify this aspect of the calculation, two types of pressure, namely P1 and P2, are calculated.

1- P1: This pressure is computed assuming that ESP spreads out and distributes over the entire area of the wall opposite to the opening. It is calculated using the formula:

$$P1 = \frac{ESP \times Z}{A} \tag{6}$$

2- P2: This pressure is computed assuming that ESP is not distributed but instead loads only a portion of the opposite wall equal in area to the opening area (Z). It is calculated as:

$$P2 = \frac{ESP \times Z}{Z} = ESP \tag{7}$$

3- To account for the varying pressure distribution within the enclosed space during the blast event, an average of P1 and P2 is utilized. This average, denoted as Average Equivalent Static Pressure (AESP), is calculated as:

$$AESP = \frac{(P1 + P2)}{2} \tag{8}$$

The rationale behind averaging these two extreme values is the assumption that it provides a reasonable distribution of pressure throughout the air volume. However, it's important to note that depending on the actual layout and specific conditions of the space, AESP may be calculated using different ratios of P1 and P2. This flexibility allows for adjustments tailored to the unique characteristics of the environment under consideration.

After AESP is calculated, the following steps shall be taken to obtain the Design Static Pressure (DSP);

i) Calculate reduction in the volume due to AESP being applied as:

$$\varepsilon v = \frac{AESP}{BM} \tag{9}$$

j) Calculate Design Static Pressure as:

$$DSP = \left(\frac{\varepsilon v}{1 - \varepsilon v}\right) \times P_a = \left(\frac{\varepsilon v}{1 - \varepsilon v}\right) \times 101.3 \times 10^3\ N/m^2 \tag{10}$$

The Design Static Pressure (DSP) can be employed to assess the structural response of the enclosing structural system within the space under investigation.

SAMPLE CALCULATION OF EQUIVALENT STATIC PRESSURE (ESP) AND DESIGN STATIC PRESSURE (DSP)

In this example, we will compute equivalent static pressure for a sample blast incident using the previously described method. In this example, a peak dynamic reflected pressure of $P_r = 20\times10^3$ N/m^2 with a duration of $t_d = 65$ ms is considered.

The assumed space has the following inside dimensions:

inside width, W = 8.5 m

inside height, H = 4 m

inside length, L = 8 m

Therefore, the inside area of exposed wall is:

A = 8.5 × 4 = 34 m^2,

An opening area of Z = 7.5 m^2 has been considered in this example.

a) Calculate mass: the mass of 1.0 m^2 of 8 m long column of air will be,

Mass = $1.225 \times 8 \times 1 \times 1 = 9.8$ N.s^2/m

b) Calculate stiffness of air:
k = 142×10^3 /8 =17750 N/m

c) Calculate natural period of air column volume using Eq. (2) and with the load mass factor being K_{LM} = 0.67:

$$T = 2\pi\sqrt{\frac{K_{LM}\ Mass}{k}} = 2\pi\sqrt{\frac{0.67 \times\ 9.8}{17750}} = 121\ ms$$

d) $P_r = 20\times10^3$ N/m^2 and td = 65 ms

e) Calculate $\frac{t_d}{T} = \frac{65}{121} = 0.54$

f) Determine the Dynamic Load Factor (DLF) from Figure 2, based on the ratio of the duration of the blast impulse to the natural period of
$\frac{t_d}{T} = 0.54$ then from Figure 2 DLF max = 1.25

g) Calculate Equivalent Static Pressure (ESP):

$ESP = P_r \times DLF = 20\times10^3 \times 1.25 = 25\times10^3$ N/m^2

h) Calculate Average Equivalent Static Pressure:

$$P1 = \frac{ESP\times Z}{A} = \frac{25\times10^3\times7.5}{34} = 5515\ \text{N/m}^2$$

$P2 = ESP = 25\times10^3$ N/m^2

$$AESP = \frac{(P1+P2)}{2} = \frac{(5515+25\times10^3)}{2} = 15257\ \text{N/m}^2$$

i) Calculate reduction in the air volume due to AESP being applied. Since, the space contains air at atmospheric pressure with an absolute pressure of $P_a=101.3\times10^3$ N/m^2 when an AESP of 15257 N/m^2 is applied to the air volume, the volume will reduce by:

$$\varepsilon v = \frac{AESP}{BM} = \frac{15257}{142\times10^3} = 0.107$$

j) Calculate Design Static Pressure. As the air volume has reduced by 0.107, accordingly the absolute pressure will increase by:

$$DSP = \left(\frac{\varepsilon v}{1-\varepsilon v}\right) \times P_a = \left(\frac{0.107}{1-0.107}\right) \times 101.3 \times 10^3 = 12.14\ \text{N/m}^2$$

The Design Static Pressure (DSP) acting inside is 12.14×10^3 N/m^2. This value can be utilized to assess the response of the structural components surrounding the space under consideration.

VERIFICATION OF RESULTS

It is important to emphasize that a direct comparison between a static and a dynamic loading is not feasible. However, to evaluate the effectiveness of the Equivalent Static Method

proposed in this paper, comparison was made to the results obtained by the full-scale tests presented by Codina et al. [4].

Four separate full-scale tests were carried out and various standoffs, charges and angle of inclination to the target. The field experiment investigated a partially vented room subjected to four different combinations of external charge weights and standoff distances. Test 2 was selected based on its location directly perpendicular to the wall opening, with a charge weight of 5 kg. equivalent TNT at a 25m standoff. The square room consisted of a reinforced concrete frame filled with four masonry walls, roof slab and a square opening in the middle of the front wall.

The clear inner dimensions of the square room were:

Inside length of typical wall: L = 2.64 m

Height: H = 2.22 m

Opening area: $Z = 0.64\ m^2$

Wall area: $A = 2.64 \times 2.22 = 5.86\ m^2$

Four gauges were installed as part of the test setup. We will be using information from two of the four gauges for this comparison. Gauge G1 was located at the center of the room at 1m above the floor level, and gauge G3 was located at the exterior face, aligned with the center the opening and at 0.5m above the floor level. G1 measures the overpressure and impulse in the center of the room; G3 measures overpressure and impulse at the exterior envelope below the opening; it is this overpressure and impulse that compresses the volume of air inside and raises its pressure.

Using the procedure described in this paper, the Design Static Pressure (DSP) can be calculated as follows:

Mass = $1.225 \times 2.64 = 3.234\ N.Sec^2/m$

k of air column = $142 \times 10^3 / 2.64 = 53788\ N/m$

$$T = 2\pi\sqrt{\frac{K_{LM}\ Mass}{k}} = 2\pi\sqrt{\frac{0.67 \times 3.234}{53788}} = 39.9\ ms$$

From Table 2 of Ref. [4], the charge weight of TNT and standoff distance for Test No. 2 were 5Kg and 25 m respectively. From Table 3 of Ref. [4], maximum reflected overpressure P_r at gauge G3 is $18.41 \times 10^3\ N/m^2$ and from Table 4 of Ref. [4], the maximum reflected impulse at gauge G3 is $51.64 \times 10^3\ N/m^2$ ms. Based on triangular pressure-time variation, the positive phase duration td is 5.6 ms. As such $\frac{t_d}{T} = \frac{5.6}{39.9} = 0.14\ ms$ and DLF from Figure 2 is 0.45.

The Equivalent Static Pressure (ESP) and Design Static Pressure (DSP) can then be calculated as:

$ESP = P_r \times DLF = 18.41 \times 10^3 \times 0.45 = 8.28 \times 10^3\ N/m^2$

$$P1 = \frac{ESP \times Z}{A} = \frac{8.28 \times 10^3 \times 0.64}{5.86} = 0.90 \times 10^3 \text{ N/m}^2$$

$$P2 = ESP = 8.28 \times 10^3 \text{ N/m}^2$$

$$AESP = \frac{(P1+P2)}{2} = \frac{(0.90 \times 10^3 + 8.28 \times 10^3)}{2} = 4.59 \times 10^3 \text{ N/m}^2$$

$$\varepsilon v = \frac{AESP}{BM} = \frac{4.59 \times 10^3}{142 \times 10^3} = 0.032$$

$$DSP = \left(\frac{\varepsilon v}{1 - \varepsilon v}\right) \times 101.3 \times 10^3 = \left(\frac{0.032}{1 - 0.032}\right) \times 101.3 \times 10^3$$

$$DSP = 0.033 \times 101.3 \times 10^3 = 3.35 \times 10^3 \text{ N/m}^2$$

The following information is extracted from the test results in Ref. [4]:

Gauge 1: From Table 13, the maximum overpressure for Test No. 2 is 9.05×10^3 N/m^2 and from Table 4, the maximum reflected impulse is 32.31×10^3 N/m^2 ms. Based on triangular pressure-time variation, the positive phase duration td is 7.2 ms. This applies to the center of the room 1 m above floor.

As mentioned before, it would not be possible to directly compare static and dynamic pressures, however, a practical approach to evaluate the equivalent static method would be to design a component of the building using both the static and dynamic pressures, and compare the results. For that purpose, we will compare the dynamic analysis of a vertical partition wall with the following properties, using the maximum overpressure and impulse at gauge G1, to the static design using the DSP equal to 3.35×10^3 N/m^2 calculated above.

The partition structural system is assumed to consist of 150 mm×63.5 mm×1.6 mm light gauge steel channels at 1.5 m center to center spacing. A dynamic yield strength of 430 MPa is used in design. The height of wall is 3 m and the space between the vertical channels is framed with light gauge steel framing and steel sheets. The wall system spans vertically from floor to floor.

The dynamic analysis was carried out using SBEDS [5] and static design was carried out by commonly used static design methods. The ductility ratio and deflection were computed in the case of dynamic analysis method and similarly flexural stress and deflection were computed in the case of Design Static Pressure Method. Table 1 summarizes the analyses results.

Table 1. Summary of analyses results

Loading Type	Ductility Ratio	Flexural Stress	Deflection
Dynamic Analysis method	0.47	Not applicable	11.4 mm
Design Static Pressure (DSP) method	Not applicable	375 MPa	15.2 mm

A review of the summary in Table 1 shows that the Design Static Pressure method yields more conservative results compared to the Dynamic Analysis method. The Design Static Pressure method results in wall deflection of 15.2 mm, while the Dynamic Analysis method results in wall deflection of 11.4 mm. This suggests that a structural member designed using the Design Static Pressure method as proposed in this paper would also meet the criteria when assessed using the Dynamic Analysis method.

CONCLUSIONS

The current methods for determining interior pressure in buildings due to external blasts through broken windows or openings pose significant challenges in terms of complexity and time consumption. Traditional approaches like the UFC 3-340 procedure and Computational Fluid Dynamics (CFD) techniques often require specialized software and substantial time investment. To address these issues, this study introduces a simplified procedure based on converting dynamic pressure and impulse into Equivalent Static Pressure (ESP). This method offers a practical solution for preliminary assessment of interior blast pressures and evaluating various design configurations. Comparative analysis with test data from [4] indicates that the proposed ESP method yields results in the same order of magnitude as a dynamic analysis. The proposed method should only be used for preliminary analysis to be verified by other established methods for final analysis and design.

ACKNOWLEDGMENTS

The help provided by Megan Besley in producing the paper is gratefully acknowledged.

REFERENCES

[1] Department of Defense. (2008). U.S. DoD: Structures to Resist the Effects of Accidental Explosions. Washington, DC, USA. UFC 3-340-02.

[2] Biggs, John M. (1964). Introduction to Structural Dynamics. McGraw-Hill Book Company. New York, USA.

[3] CSA Group. (2018). CAN/CSA-852-18. Blast resistant window anchor systems. Toronto, Ontario, Canada.

[4] Codina, R., & Ambrosini, D. (2017). Full-scale testing of leakage of blast waves inside a partially vented room exposed to air blast loading. Springer-Verlag GmbH Germany.

[5] U.S. Army Corps of Engineers; PDC TR-06-02 Rev1; September 2008; Single-Degree-of-Freedom Blast Effects Design Spreadsheet (SBEDS); Department of Defense, Washington, DC.

STUDY ON FLUCTUATING WIND PRESSURE CHARACTERISTICS AND FATIGUE PERFORMANCE OF FULLY ENCLOSED NOISE BARRIER OF BEIJING-XIONG'AN INTERCITY HIGH-SPEED RAILWAY BRIDGE

Ming LI [1,3], Changqing MIAO [1,2], Manrong SONG [4,5], Gezhi XU [4,5], Pengyu DONG [2]

[1] Key Laboratory of C & PC Structures Ministry of Education, Southeast University, Nanjing 211189, China;

[2] School of Civil Engineering, Southeast University, Nanjing 211189, China;

[3] The Civil Construction Engineering Co., Ltd. of CRESH Group;

[4] College of Civil and Hydraulic Engineering, Hefei University of Technology, Hefei 230009, China;

[5] Anhui Key Laboratory of Civil Engineering Structures and Materials, Hefei University of Technology, Hefei 230009, China

Corresponding Author: 1. Changqing MIAO, PhD, Professor; Nanjing, Jiangsu, China, 211189; **2. Manrong SONG, PhD, Associate Professor;** Hefei, Anhui, China, 230009.

Email: chqmiao@163.com (Changqing MIAO); songmanrong@hfut.edu.cn (Manrong SONG).

ABSTRACT

Related to the project of the fully enclosed noise barrier of Beijing-Xiong'an intercity high-speed railway, the fluctuating wind pressure, structural dynamic response, and structural fatigue performance of the train passing at 350 km/h were studied. Based on the computational fluid dynamics analysis method, the finite element flow field model and the train and the noise barrier structure model were established. The fluctuating wind pressure on the wall surface of the noise barrier and the time-history dynamic response of the noise barrier unit plate and the steel arch were analyzed. The results show that the maximum stress position of the noise barrier appears near the column base. The 1:1 full-scale boot steel column base specimen and concrete pedestal were designed and manufactured, and 4 million fatigue loading tests were carried out on the members under the most unfavorable design load conditions. The displacement and stress time-history curves of steel column foot, concrete, and bolt under various cyclic loading were obtained. A high-accuracy finite element model of the noise barrier column base was established, and different stress fields and corresponding fatigue load spectra were introduced for fatigue analysis. Depending on the fatigue test results and finite element analysis, the structural safety was verified.

Keywords: *High-Speed Railway, Fully Enclosed Noise Barrier, Numerical Simulation of Fluctuating Wind, Fatigue Test, Design Optimization.*

1 INTRODUCTION

With the increasing scale of China's railway construction, noise pollution is considered the most significant environmental pollution factor caused by high-speed rail to society [1,2]. Compared with ordinary trains, high-speed trains use ballastless tracks, and the friction noise between wheels and tracks has been reduced to very low. However, due to its extremely fast speed, the noise generated by the friction between the train and the air cannot be ignored and even far exceeds the wheel-rail noise of ordinary trains [3].

As one of the effective methods to reduce noise pollution, noise barriers have been widely used in railway transportation [4,5]. However, when the high-speed railway passes through residential or ecological protection areas, the ordinary vertical and semi-closed noise barriers can no longer meet the noise reduction standards. The fully enclosed noise barrier has a closed structure and good air tightness. It can maximize the arrangement of unit plates to absorb noise, and the noise reduction performance is the most prominent [6]. However, air mobility is more limited when the train is running, and the compressed air flow cannot be discharged in time to form a strong piston wind effect, which brings a vast aerodynamic impact to the fully enclosed noise barrier structure [7]. In the design service life period, the noise barrier needs to withstand millions of times of train fluctuating wind pressure. Therefore, analyzing the vehicle-induced fluctuating wind pressure, structural dynamic response, and fatigue performance when the high-speed train passes through the fully enclosed noise barrier is necessary. At present, few scholars at home and abroad are involved.

In terms of train-induced fluctuating wind pressure, Tomasini [8] conducted a wind tunnel test to compare the train model and the surface pressure of the barrier under different types, heights, and porosity wind barriers when the train is running in a low-speed test section ($Re = 1.3 \times 105$). Hashmmi [9] measured the surface pressure of different windbreak walls of a 1: 25 scaled model of a 390-class Pendolino train in the wind tunnel at different wind incident angles and evaluated the influence of the transition zone where the windbreak wall undergoes geometric changes on the aerodynamic characteristics of the train when it is subjected to crosswind. In China, Long [10] numerically simulated the air fluctuating pressure caused by the train passing through the noise barrier of the Beijing-Tianjin high-speed passenger dedicated line, obtained the fluctuating pressure curves of each part of the noise barrier at different train speeds, and analyzed the distribution law of air fluctuating pressure in detail. Peng [11] established a bridge tunnel, bridge wall, and bridge-dike transition section model using dynamic mesh technology. The numerical simulation results were compared with the wind tunnel test to compare the aerodynamic pressure differences at different positions when the train passed through different transition sections.

Thomas Keller et al. [12] experimentally studied the fatigue performance of vertical noise barrier columns reinforced with glass fiber-reinforced plastics (GFRP) for the mechanical

properties of fully enclosed noise barriers. Berthellemy Jacques et al. [13,14] studied the mechanical properties of the composite pins connected between the noise barrier column base and the concrete base, introduced the fatigue behavior under cyclic loading in detail, and optimized the design concept based on the model. In China, to better improve the actual noise reduction effect of the noise barrier, Lv [15] proposed a method to simplify the excitation input of fluctuating wind load to analyze the fluctuating wind-induced response of the noise barrier and gave suggestions on the insert plate noise barrier and the integral noise barrier. Ma [16] designed a full-scale, fully enclosed noise barrier model to simulate the fatigue performance of steel beams and connecting bolts of the noise barrier under equivalent train fluctuating wind pressure.

The Beiluodiancun project of the newly-built Jingxiong intercity railway is the first fully enclosed noise barrier project of a high-speed railway with a design speed of 350 km / h at home and abroad, which needs systematic technical research. This study mainly studies the vehicle-induced fluctuating wind pressure, structural dynamic response, and structural fatigue performance of the noise barrier project when the train passes at 350km / h.

2 PROJECT PROFILE

The fully enclosed noise barrier is in the DK78 + 082.72-DK78 + 929.97 section of the Guba Bridge. The design speed is 350 km / h, and the total length of the project is 847.25 m, as shown in **Fig. 1.** It includes 16-32 m, 2-24 m simply supported beams and a (73 + 128 + 73) m continuous beam. The innovative main structure of the fully enclosed noise barrier adopts a fully welded circular arc H-shaped steel frame with a span of 13.28 m and a height of 9.4 m. It comprises three arc H-shaped steel beams, as shown in **Fig. 2**. The steel frames are connected by tie rods with a spacing of about 2m. The side and top of the noise barrier are respectively provided with full-length inter-column support and full-length horizontal support. The column foot is rigidly connected to form a stable unit structure. The steel column base adopts a boot-shaped column base with an inward opening. Four transverse and two longitudinal U-shaped bolts are innovatively used in the connection joint between the steel column base and the concrete box girder. The material of the beam and column main steel structure, joint connecting plate, stiffening plate, and column bottom plate is Q355D; the material of the column support, top support, and tie bar are Q355B., and the total mass of the steel structure is 2972t.

Figure 1. Sound barrier accurate picture

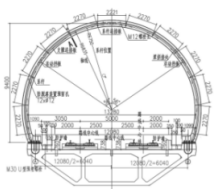

Figure 2. Fully enclosed noise barrier structure

3 NUMERICAL MODELLING

3.1 Establishment of numerical model

3.1.1 Determination of computational domain

In the flow around a high-speed train, the computational domain boundary distance model should be at least three times the model height [17]. Therefore, the width of the calculation domain was 30 m, and the height was 30 m. The longitudinal length was 920 m. In addition to the 420 m noise barrier, there was a 250 m buffer zone at the front and rear. The region was divided into two parts: the dynamic grid fluid region and the static grid fluid region (from now on referred to as the dynamic grid region and the static grid region). As shown in **Fig. 3**, the following models are based on the dynamic and static areas.

3.1.2 Mesh subdivision

The static grid area comprised a fully enclosed noise barrier and the remaining air in the computational domain. The length of the fully enclosed noise barrier model was 420 m, and the bottom of the vehicle was 0.3 m from the ground, which was a double lane. The maximum size of the grid was 0.7 m, and the number of grids was 5.3351 million. The dynamic grid area comprised the train and the surrounding attached air. The train model took CRH380A surface parameters. The model's width was 3.38 m, the height was 3.70 m, and the total length was 74.28 m. A three-car train formation was adopted, and the head car, tail car, and part of the intermediate length were retained. The lengths of the head car, the middle car, and the tail car are shown in **Fig. 4**. The maximum size of the grid in the dynamic grid area was 0.2m, and the number of grids was 965,000 (single vehicle).

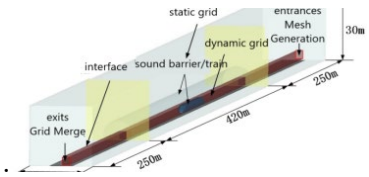

Figure 3. Calculation domain diagram

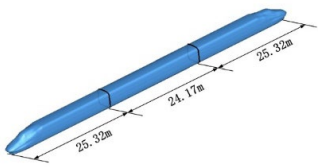

Figure 4. Simplified train model

3.1.3 Boundary condition

The fully enclosed noise barrier, the ground, and the surface of the train body were all wall conditions. Considering the viscosity of air, the above surface was set as a non-slip adiabatic boundary, the tangential velocity was 0, and the typical dimensionless wall distance (y+) value was 100. It was calculated that the air on the outer surface could flow freely, and the air in the noise barrier was static, all of which were in the standard atmospheric pressure state. In the grid model, the junction position of the dynamic and static grids was set as the interface condition.

3.1.4 Monitoring points layout

When the two trains met, the pressure load of the middle section of the noise barrier changed most drastically [18]. At the same time, considering the needs of structural analysis, a section was set every 2 m in the middle section, and every 30 m in the rest of the position, a total of 30 sections, and the number increases in turn along the driving direction, as shown in **Fig. 5(a)**. The selected section was arranged with 11 measuring points, corresponding to 11 noise barrier unit plates. The points were located at the center of the unit plate. They were numbered successively from one side of the train. The numbers of measuring points of different sections were accumulated in turn. The monitoring points of the No.1 section are shown in **Fig. 5(b)**.

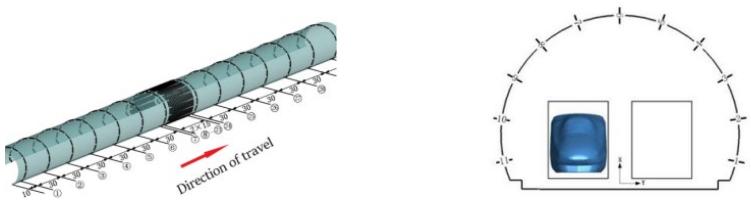

（a）Cross-section layout of noise barrier　　（b）noise barrier section measuring points

Figure 5. Noise barrier numerical simulation monitoring point layout

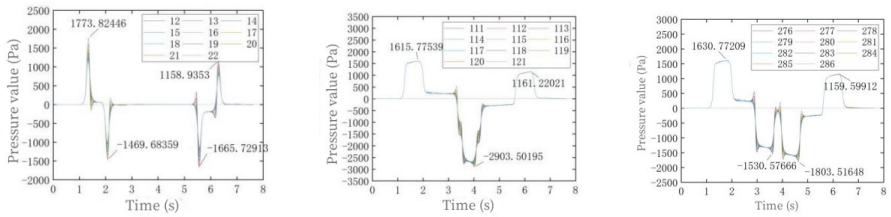

(a) Section 2　　(b) Section 12　　(c) Section 24

Figure 6. The time history curve of pressure at the measuring points of intersection of the train with a speed of 350 km/h at the middle section

3.2 Distribution law of train fluctuating wind along train running direction

Fig. 6 shows the fluctuating wind pressure time history curve of some sections and corresponding measuring points when the trains meet at 350 km/h in the middle section of the noise barrier. The time history curve of fluctuating wind has a certain symmetry. The height of the pulsation curve between different measuring points on the same section coincides, indicating that the pressure value of the same section of the sound barrier changes uniformly during the running of the train. The pressure amplitude of the section near the entrance and exit of the sound barrier is smaller. It shows that the middle section of the noise barrier is subjected to more complex and severe fluctuating wind impact.

4 DYNAMIC ANALYSIS OF FULLY ENCLOSED NOISE BARRIER STRUCTURE

In this section, the dynamic response of the fully enclosed noise barrier structure was analyzed by loading the fluctuating wind time history load of the train obtained above the structural surface.

4.1 Establishment of integral finite element model

The length of 32 m in the middle section of the sound barrier is taken as the calculation unit to model in ANSYS, as shown in **Fig. 7**. The model was divided into four parts: steel arch, tie bar, inclined web member, and unit plate. BEAM188 beam element was used for the steel arch, BEAM188 beam element was used for the tie bar and web member, and SHELL181 element was used for the unit plate. The boundary condition was that the steel arch bottom plate was firmly connected to the ground.

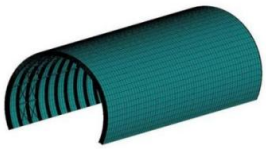

Figure 7. Overall model

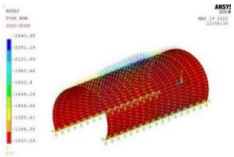

Figure 8. Pulsating wind loading

4.2 Pulsating wind loading

The fluctuating wind load is mainly transmitted to the steel arch through the metal element plate, and the overall force is supported by the tie bar and the inclined web bar. The above shows that the time-history curves of the main fluctuating wind at different measuring points on the same section of the sound barrier are highly coincident. Therefore, the load of each wind pressure time history point in the fully enclosed sound barrier model is uniformly applied as a surface load to its corresponding unit plate, as shown in **Fig. 8**. The correctness of the finite element model and the loading method were verified by comparing the dynamic test report of the noise barrier of Jingxiong high-speed railway.

4.3 Dynamic response of the unit plate

Fig. 9-10 show the stress response and vertical displacement response of the sound barrier unit plate when the train meets near the middle section at three moments of 1.50 s, 3.80 s, and 6.10 s at 350 km / h.

The stress distribution of the sound barrier unit plate is uniform, and the stress level is slightly more prominent at the centroid position. When the train meets, the fluctuating wind load is large, and the component stress increases. The stress of the element plate near the column foot at three moments increases locally due to the intersection of trains. As shown in **Fig.9**, the maximum stress of the element plate appears near the column foot at three moments. The

overall vertical displacement of the sound barrier unit plate is not uniform, and the displacement of the unit plate at the top and side is significant. When t = 3.80 s, the displacement of the unit plate at the end of the sound barrier increases sharply. When t = 1.50 s and t = 6.10 s, the unit plate expands outward, and the member is subjected to positive pressure. When t = 3.80 s, the unit plate shrinks inward, and the component is subjected to negative pressure.

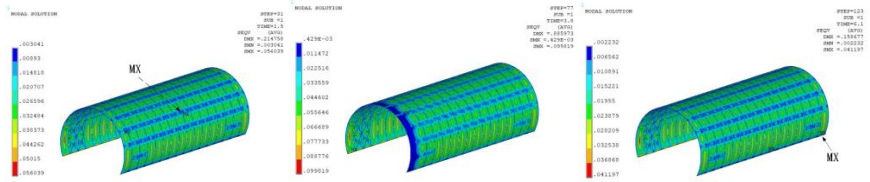

(a)1.50 s (b)3.80 s (c)6.10 s

Figure 9. Stress response of element plate

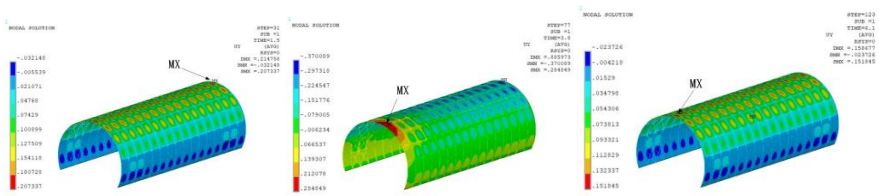

(a)1.50 s (b)3.80 s (c)6.10 s

Figure 10. Displacement response of the unit plate

4.4 Dynamic response of column foot

During the running of the train, the maximum stress often appeared in the unit plate near the foot of the noise barrier. Six measuring points are arranged at an interval of 10 m on the left and right sides near the foot of the steel skeleton column, as shown in **Fig. 11**.

Fig. 12-13 show the stress response and displacement response of the column foot measuring points when the train meets inside the fully enclosed sound barrier, respectively. The dynamic response curves of the measuring points on the same side are similar. The stress curves of the measuring points of the column foot show more obvious stress fluctuation when the fluctuating wind has peaks and troughs, and apparent positive stress appears near the measuring points of 1 #-3 #, indicating that the squeezed air causes the structure to expand outward. Except for the 5 # measuring point, the stress curves on the same side are similar. The displacement curve of the column foot measuring point fluctuates when the wind peaks and troughs fluctuate.

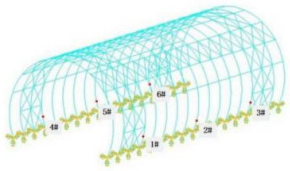

Figure 11. Layout of column foot measuring points

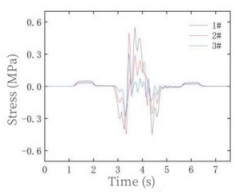

(a) 1 # - 3 #

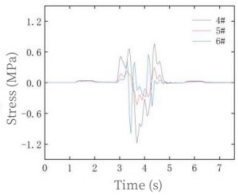

(b) 4# - 6 #

Figure 12. The stress response

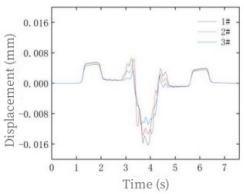

(a) 1 # - 3 #

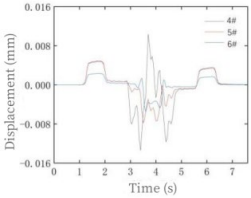

(b) 4# - 6 #

Figure 13. The displacement response

5 FATIGUE TEST OF COLUMN FOOT

5.1 Specimen design

Combined with the fluctuating wind and the numerical simulation results of the whole model, the maximum stress of the fully enclosed sound barrier under different working conditions appeared near the column foot. The previous simulation focused on the overall stress characteristics of the structure and the detailed structure of the column base of the sound barrier was not considered. In this section, a fine model composed of the column base of the sound barrier, the concrete pedestal, and the U-shaped connecting bolts was established to analyze the stress of the component. According to the full-scale test, the steel column foot member was 2.1m high, and the loading height was 1600mm according to the most unfavorable stress and the stress analysis results of the most unfavorable working conditions. The loading end plate was set at 0.5 m downward from the top of the column base. The structure and geometric dimensions of the steel column base specimen are shown in **Fig. 14**. The structure and geometric size of the concrete pedestal specimen were 1100mm × 1500mm × 1100mm, which was connected with the steel column base by U-shaped bolts, and fixed with the ground groove by anchor bolts.

5.2 Material properties

8.8 grade friction type high strength bolts and Q345 D grade steel were used in this test. Three groups were selected for the material test. The results showed that the yield strength of the U-bolt was 548 MPa, the ultimate strength was 758 MPa, the yield strength of steel was 379 MPa, and the ultimate strength was 529 MPa.

5.3 Test scheme

5.3.1 Test device

The test devices included an MTS hydraulic servo system, reaction wall, dynamic acquisition instrument, static acquisition instrument, etc. By loading the end plate, the MTS actuator applied a horizontal fatigue load to the steel column base specimen. The test-loading devices are shown in **Fig. 15**.

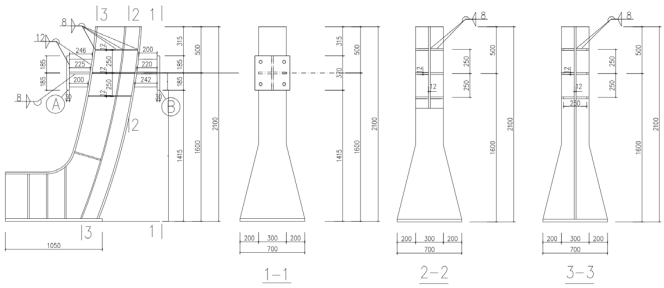

Figure 14. Steel column base structure and geometric size/mm

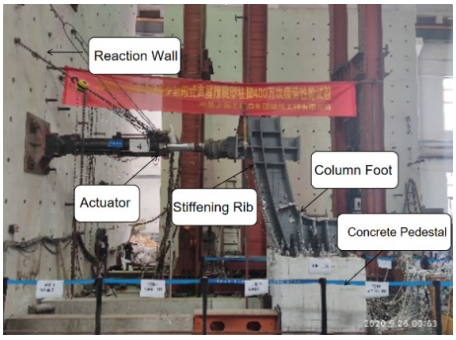

Figure 15. Test loading devices

5.3.2 Loading scheme

During the test, the most unfavorable stress of the bolt under the most unfavorable conditions was taken as the equivalent basis. The lower limit load of fatigue was 5kN, the upper limit load was 60.4kN, and the sinusoidal pulse cycle (5,60.4) kN was applied. A total of 4 million times were loaded, and the data were collected by the dynamic acquisition instrument.

Through the spectrum amplitude curve of fluctuating wind pressure, it can be seen that the main frequency of fluctuating wind pressure was 0.2Hz when the train passed, and there was an obvious resonance phenomenon when the loading frequency was about 4Hz. Combined with the actual conditions and time constraints of the laboratory, the loading frequency of this fatigue test was 10Hz.

Before the fatigue test, a static cyclic loading was completed, and the data were collected. When the number of cyclic load loading reaches 1 million, 2.1 million, 2.5 million, 2.9 million, 3.2 million, 3.8 million, and 4 million times, the machine is stopped, respectively, and the dynamic acquisition was converted into static acquisition for static loading. Loading starts from 5kN, increasing the load step by step to 60.4kN, and then unloading step by step to 5kN, during which the load increment was 5kN, a total of two cycles

5.3.3 Measurement solutions

Strain gauges were arranged on the flange of the steel column foot, the embedded part of the U-bolts, and the concrete surface. Strain flowers were arranged on the bottom plate, web, and stiffener of the steel column foot. The arrangement scheme of strain gauge measuring points is shown in **Fig.16-18**. Displacement meters W1 and W2 were respectively set in the middle of the actuator and the outer flange of the bottom plate.

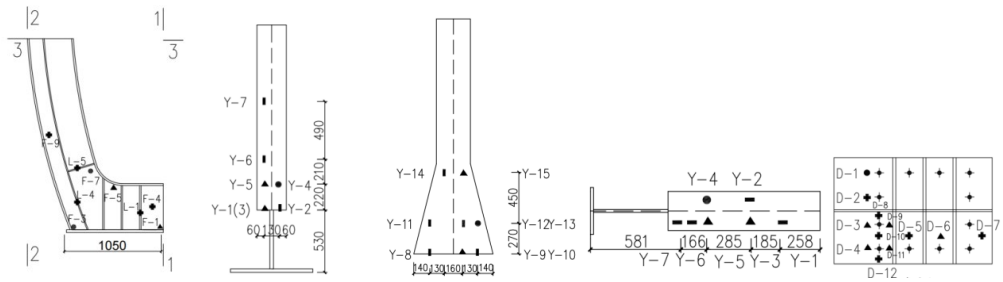

Figure16. The schematic diagram of the measuring points of the boot-type column foot

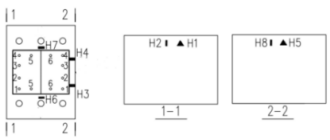

Figure 17. Concrete base measuring points diagram

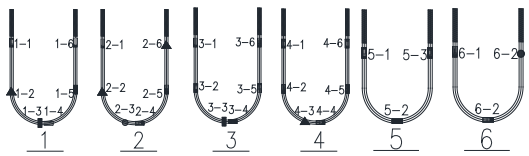

Figure 18. U-shaped bolt measuring points diagram

5.4 Experiment results and analysis

5.4.1 Experimental phenomena

The flange web was observed before and during the static test at each shutdown. No deformation of the structure was found, the paint coating did not fall, and the weld was complete. The U-shaped bolts were well anchored, and no deformation was found. There was no gap between the nut and the bottom plate, and the bottom nut rotated slightly compared with that before the test. The concrete pedestal concrete pedestal structure was complete, no displacement occurred, and no cracks occurred. The corresponding parts of the specimen after 4 million cycles of cyclic loading are shown in **Fig.19**.

（a）Web （b）Inner flange （c）Outer flange （d）U-bolts （e）Concrete

Figure 19. Test observation results of each component

5.4.2 Static loading stress and displacement analysis

The stress-loading series curves of each measuring point under different load cycles were obtained by the static loading test. The linear relationship between the loading and unloading curves of the measuring points of each component was apparent, and the stress curves after different fatigue loading times almost coincided, indicating that the stress characteristics of the steel column base did not change under the fatigue load. **Fig. 20** shows the maximum stress-cycle number curve of each measuring point in the static stop test. The maximum stress trend of most measuring points is almost linear, indicating that the mechanical properties of the steel column base system are relatively stable during the fatigue loading process.

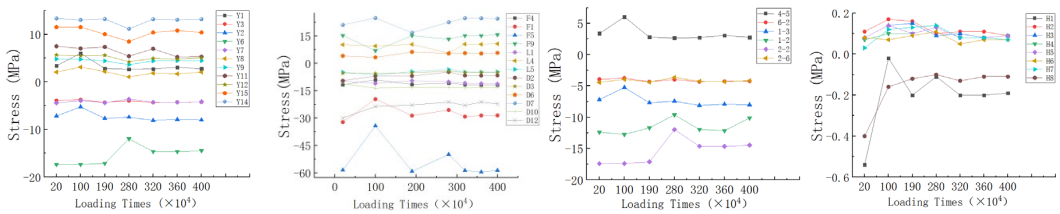

(a) Flange （b）Stiffening rib of web bottom plate （c）U-bolts （d）Concrete

Figure 20. The relationship curve between the maximum stress of the measuring points and the number of typical fatigue loading cycles

The displacement of the W1 measuring point varied from -1.5 to 1.0mm, and the linear relationship between the loading and unloading curves of the load is obvious. The displacement of the W2 measuring point varied from 0 to 0.5 mm, indicating a slight loosening between the foot of the shoe column and the concrete pedestal. Under different load cycles, the shape and trend of the curve were roughly the same, and the maximum displacement of each measuring point was obtained under the same loading series. The displacement-thrust curve was symmetrical in the two loading and unloading processes, indicating that the specimen had good recoverability.

5.4.3 Fatigue loading stress analysis

Fig.21 shows the time history curve of the stress of the steel structure's flange, web, and U-

shaped bolts under different load cycles. Each curve is in the form of a sine wave, which is consistent with the loading curve. The shape of the time history curve under different load cycles is almost coincident, with similar periods and amplitude.

Fig. 22 shows measuring points' stress amplitude curves under different fatigue loading cycles. The stress amplitude of each part of the steel column foot and the U-shaped bolt did not attenuate, almost in a horizontal straight line; the dynamic strain change is consistent with the load change, which well reflects the elastic advantages of steel. The maximum strain (tension or compression) is almost consistent with the corresponding maximum value under static load. The stress of each measuring point is low, the stress amplitude is lower than the fatigue limit, the material has a significant degree of surplus, and the size of the steel column foot has ample optimization space.

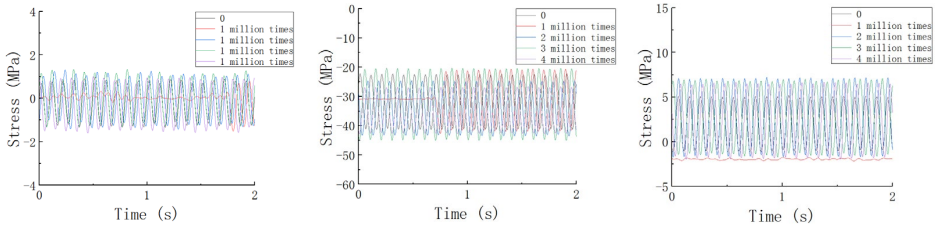

(a)Y3 （b）F5 （c）2-6

Figure 21. Dynamic stress time history curve of measuring points

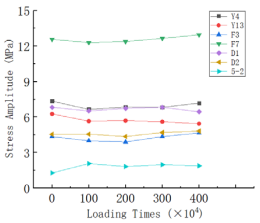

Figure 22. The relationship curve between the stress amplitude of the measuring points and the number of fatigue loading cycles

6 FATIGUE LIFE ESTIMATION OF FULLY ENCLOSED NOISE BARRIER

6.1 Establishment of a steel beam model

A fine finite element model of the shoe-type column base of the sound barrier was established, and the fatigue life of each component was obtained. The validity of the model and fatigue analysis method was verified by comparison with the aforementioned test results. Further expanded the model to simulate the fatigue life of a steel beam.

Rhino solid modeling was used to establish the finite element model. Hypermesh was used to preprocess the finite element mesh, and 20 mm was selected as the standard mesh size. After the mesh preprocessing was completed, it was imported into ANSYS Workbench for static analysis. The steel part adopted the solid185 element with plasticity, stress stiffening, and supporting large strain. The concrete base adopted the Solid65 unit and the Solid185 unit. The friction pair of bolt pre-tightening force was used to limit the displacement between the U-shaped bolt group and the boot column foot. The reinforced concrete base was modeled by hybrid modeling, the key parts were modeled by separate modeling, and the rest parts were modeled by integral modeling. The boundary condition was set to all six degrees of freedom constraints of the surrounding elements of the concrete base.

6.2 Calculation results

The ANSYS Workbench model was imported into Ncode Designlife, and the fatigue performance of the structure was estimated by the rain flow counting method. The results are shown in **Fig. 23**.

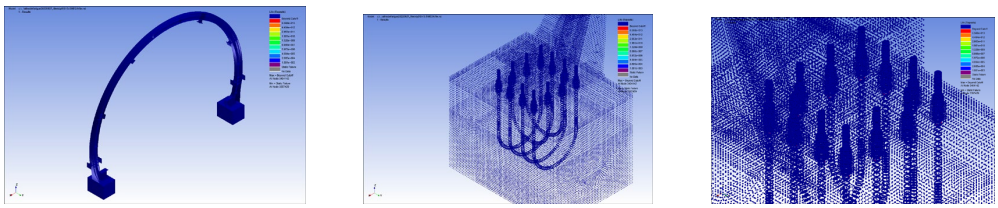

(a)The whole steel beam (b)Right boot-type column foot (c)Left boot-type column foot

Figure 23. The fatigue performance cloud diagram of the whole steel beam

Fig.23 shows that the stress field of the whole steel beam model is numerically close to that of the local boot-type column foot model, and the stress gradient is more moderate than that of the test member. Most of the fatigue properties of the structure are more than 4 million times. It can be seen from the scatter plot that the weak points of the structure are still in the stress concentration area of the U-shaped screw and mortar layer, which does not cause fatigue damage.

7 CONCLUSIONS

（1）When the train passes through the fully enclosed noise barrier, the wall pressure value of the noise barrier is positive pressure-negative pressure-positive pressure alternately. When the trains meet in the middle section, the main fluctuating wind curves of different measuring points on the same section are highly coincident. The pressure amplitude of the section near the entrance and exit of the noise barrier is smaller, while the pressure amplitude of the section near the middle section is larger.

（2）When the trains meet inside the noise barrier the unit plate shrinks inward or expands outward at different times, which corresponds to the simulation results of fluctuating wind load, but the maximum stress of the unit plate appears near the column foot. The stress amplitude and displacement amplitude of the column base position of the structure increase obviously with the increase of the vehicle speed.

（3）After 4 million times of fatigue test loading, the steel plate, weld, and stiffening rib of the steel column base are not cracked or buckled. Except for the slight rotation of the bottom nuts, the U-shaped bolts are not damaged, and the overall structure of the steel column base has good fatigue resistance.

（4）The static stop loading test shows that the stress curves of each measuring point after different fatigue loading times are almost coincident, and the maximum stress trend is almost linear. During fatigue loading, the time history curves of each measuring point under different load cycles, including amplitude and frequency, remain highly consistent and the stress variation range is small, indicating that the member has good stability under fatigue load.

（5）The finite element fatigue analysis shows that the stress field of the whole steel beam model is numerically close to that of the local boot column foot model. The stress gradient is more moderate than that of the test component, and the fatigue performance of the whole steel beam is higher than that of the test member.

ACKNOWLEDGMENTS

The authors gratefully acknowledge the financial support provided by China State Railway Group Co., Ltd.-Intelligent Jingxiong Foundation under Grant-No.-P2018G004.

REFERENCES

[1] Wang Huili, Ge Jiangchen, Wang Shanmei, et al. (2014) Study on the new index of noise impact assessment of high-speed railway.*Environmental impact assessment*,55-57.

[2] Xuan Xiaomei. (2021) Research on characterization analysis and control strategy of the negative externality of high-speed railway noise.*China Academy of Railway Sciences.*

[3] Ping Qian, Song Lizhong. (2011) Analysis of high-speed rail noise pollution *Manager*, 362-370.

[4] Yin Hao. (2008) Research progress of sound barrier structure.*Annual Meeting of Noise and Vibration Group, Environmental Protection Committee, China Railway Society, Beijing*: 38-44.

[5] Jin Ming, Zhou Jingxuan. (2005) Research progress on the structure of road noise barrier

abroad.*Highway*,190-193.

[6] Xin Siyuan, Zhang Shifeng, Wang Xiaowei. (2022) Research on noise reduction effect of fully enclosed noise barrier for Jingxiong intercity railway.*Railway standard design*, 1-6.

[7] Chen Yingqing, Liu Rundong, Liu Lanhua. (2021) Experimental study on wind pressure characteristics of fully enclosed noise barrier train for high-speed railway *Railway technology innovation*,95-99.

[8] Tomasini G, Giappino S, Cheli F, et al. (2016) Windbreaks for railway lines: Wind tunnel experimental tests.*Proceedings of the Institution of Mechanical Engineers, Part F: Journal of Rail and Rapid Transit*, 230(4): 1270-1282.

[9] Hashmi S A, Hemida H, Soper D. (2019) Wind tunnel testing on a train model subjected to crosswinds with different windbreak walls. *Journal of Wind Engineering and Industrial Aerodynamics*, 195: 104-112.

[10] Long Liping, Zhao Libin, Liu Lidong. (2010) Aerodynamic study of train induced noise barrier structure. *Engineering Mechanics*, 27: 246-250.

[11] Peng Dong. (2017) Aerodynamic characteristics and optimization measures of vehicles in the transition section of bridges and other types of lines.*Chengdu: Southwest Jiaotong* University.

[12] Keller T， Riebel F， Vallée T. （2008） GFRP posts for railway noise barriers - Experimental validation of load-carrying performance and durability．*Composite Structures*，85(2)：116-125．

[13] Berthellemy J，Lorenc W，Mensinger M，et al．(2011) Zum tragverhalten von verbunddübeln - teil 1：tragverhalten unter statischer belastung．*Stahlbau*，80(3)：172-184．

[14] Berthellemy J，Lorenc W，Mensinger M，et al． (2011) Zum tragverhalten von verbunddübeln - teil 2：ermüdungsverhalten．*Stahlbau*，80(4)：256-267．

[15] Lv Jianpin. (2010) Study on the structure of the plug-in plate and integral noise barrier for high-speed railway. *Nanjing: Southeast University.*

[16] Ma Chi. (2017) Research on static and fatigue performance of large-scale fully enclosed sound barriers for freight railways. *Wuhan: Huazhong University of Science and Technology.*

[17] Luo Yunke. (2018) Analysis of train fluctuating wind-induced vibration of the semi-enclosed sound barrier of high-speed railway.*Chengdu: Southwest Jiaotong University.*

[18] He Xuhui, Guo Kezhen, Yang Bin, et al. (2020) Numerical simulation of air pressure load on 840 m fully enclosed sound barrier of high-speed railway. *China Railway Science*, 41: 137-144.

STUDY ON DYNAMIC BEHAVIOR OF PRECAST CONCRETE COLUMNS WITH PRESSED SLEEVE CONNECTIONS UNDER IMPACT LOADING

Jun Lei[1], Qing-Jun Chen[2], Miao-jin Yao[3] and Yu-qi Zhang[4]

[1] *Mr.* School of Civil Engineering and Transportation, South China University of Technology, leijun0601@foxmail.com.

[2] *Prof.* School of Civil Engineering and Transportation, South China University of Technology, qjchen@scut.edu.cn.

[3] *Mr.* School of Civil Engineering and Transportation, South China University of Technology, 1348962749@qq.com.

[4] *Mr.* School of Civil Engineering and Transportation, South China University of Technology, 3346683587@qq.com.

Corresponding Author: Qing-Jun Chen, Prof.

381 Wushan Road, Tianhe District, Guangzhou, Guangdong, China, 510641

Email: qjchen@scut.edu.cn

ABSTRACT

Precast concrete members are increasingly being adopted, but their performance under impact loading is yet to be verified. In this study, precast concrete (PC) columns with pressed sleeve connections are investigated using finite-element (FE) simulations in LS-DYNA, accompanied by the establishment of reinforced concrete (RC) columns to facilitate a comparative analysis. The simulations are verified against experimental data. This validation underscores that the FEM models exhibit robust accuracy in simulating the impact force, displacement, and failure modes of the columns. Following this validation, an intensive parametric study is carried out to explore the influence of impact parameters on the dynamic responses of the columns. The results show that as the axial compression ratio increases, the peak displacement of the member decreases. With an increase in impact velocity, both the peak impact force and peak displacement of the member increase. Under the same impact kinetic energy, a larger impact mass leads to greater impact displacement and smaller impact force. When considering the influence of interfacial failure stress between the new and old concrete, the peak displacement of the member increases.

Keywords: *Impact Loading; Dynamic Behaviour; Precast Concrete Column; Finite Element Model.*

1. INTRODUCTION

Precast concrete (PC) structures have been widely used. The difference between PC structures and conventional cast-in-place reinforced concrete (RC) structures lies in the fact that PC structures are composed of multiple prefabricated components. In this regard, the connection region plays a crucial role in load-bearing. The safety of PC structures is significantly influenced by the methods employed for rebar connection, as well as the diverse forms in which concrete connections are made.

In PC structures, various steel rebar and structural member connection methods are utilized [1, 2]. Meanwhile, there are several methods of connecting rebars with sleeves. Extensive research has been conducted on the performance of both full and semi-grouting sleeves. Certain investigations have primarily addressed the tensile properties of sleeve specimens [3,4], while others have explored the mechanical performance of precast components with grouted sleeve connections [5-8]. However, in the actual construction process, the grouting sleeve may suffer from insufficient grouting defect, which will weaken the mechanical properties of the sleeve connection. This issue has attracted the attention and interest of scholars [9,10]. Due to the easily inspectable quality and good mechanical properties, the pressed sleeve connections are advantageous due to rapid construction and cost-effectiveness [11] and have gained widespread application in precast structures in recent years. PC members with pressed sleeve connections have demonstrated commendable seismic performance [11, 12]. However, there is a scarcity of research findings regarding their performance and failure mechanisms under impact loading.

In a PC member with pressed sleeve connections, post-poured concrete would be employed for wet connections. Therefore, there is an interface of new and old concrete between the wet connection and the PC components. The dynamic performance of this interface has not yet been clearly clarified. Therefore, this paper establishes a finite element model of a PC column considering the influence of the interface of concrete and a finite element model of RC column for comparison. Simulation results are compared with experimental data. Finally, a parametric analysis is conducted for impact velocity, axial compression ratio, and different impact mass and velocity with the same impact energy.

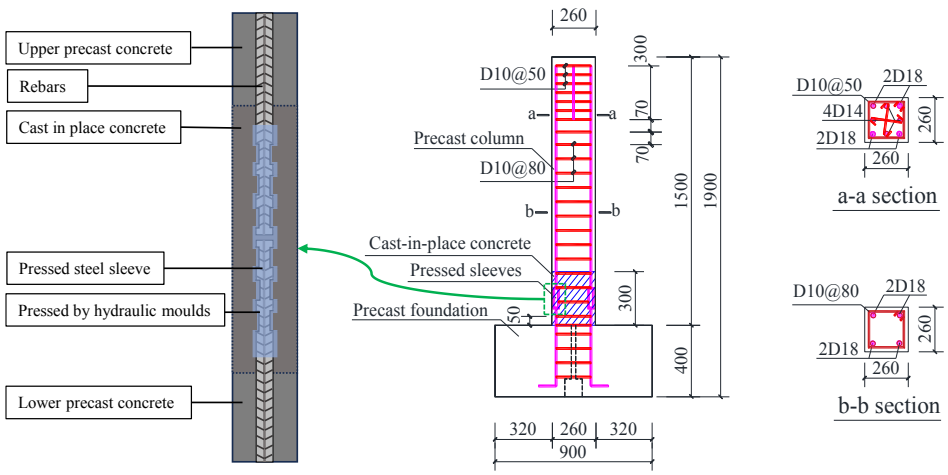

Figure 1. Reinforcement details of PC specimen (unit. mm).

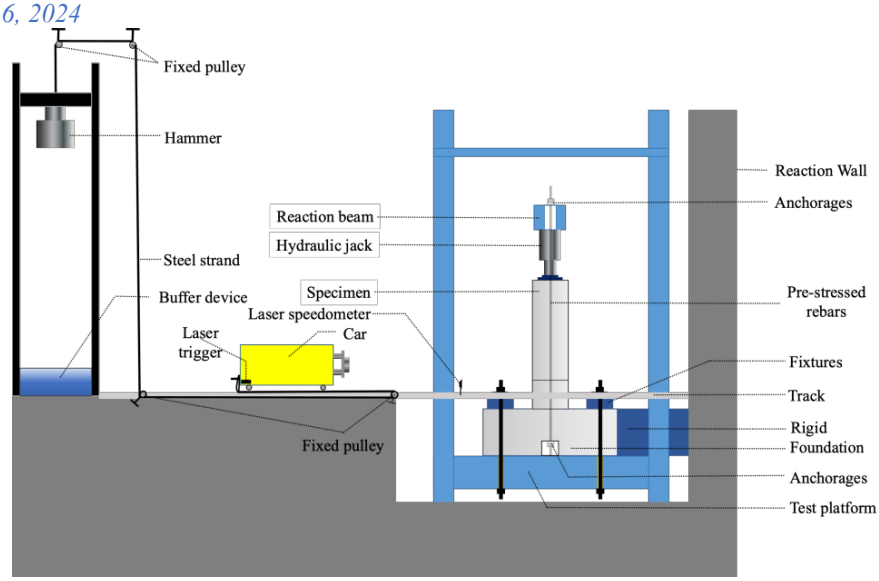

Figure 2. Sketch of the impact test setup

2. FINITE ELEMENT MODEL

2.1. Impact test

The experiment discussed in this paper involves an impact test on both a RC column and a PC column with pressed sleeve connections. Except for the cast-in-place region and the pressed sleeve connections for reinforcement, all other parameters of RC and PC members are consistent. The reinforcement details of PC column are show in Figure 1. Before the concrete was cast, two aluminum pipes were symmetrically embedded in the concrete foundation to serve as channels for the subsequent installation of pre-stressed rebars. The columns with a cross-section of 260 mm×260mm had a height of 1500mm and was reinforced with four longitudinal rebars of 18mm diameter. The stirrups of 10mm diameter were spaced 80 mm apart in most areas of the column. To prevent axial compression, within a range of 300mm from the top of the column, the stirrups were spaced 50mm apart and four longitudinal rebars of 14mm diameter were added. In PC column, the longitudinal rebars were connected by pressed sleeves of 34mm diameter and the post-pouring concrete region had a height of 300mm.

The sketch of the experimental specimen is shown in Figure 2. Before the test, the hydraulic jack and the reaction beam were installed on the top of the column, and then the two pre-stressed rebars were passed through the reserved channels and anchored to the foundation. The pre-stressed rebars and anchorages were installed on the reaction beam on the top of the column, forming a small reaction frame system, through which axial compression was applied by the hydraulic pressure of the jack. Finally, the specimen was fixed to the test platform through fixtures on the foundation.

A car with a mass of 900 kg impacted the column at a height of 500 mm from the bottom of the column. The impact head of the car was flat, forming a contact surface of size 260mm× 200mm (width × height) when the car impacted the column. Design impact parameters of the two columns are summarized in Table 1. The interconnection between the car and the hammer was

facilitated through a steel strand and four designated pulleys. In the experiment, the hammer was dropped from a predetermined height, causing it to descend and subsequently pull the car to accelerate to the desired velocity. An automatic decoupling mechanism was installed about 4 meters from the test specimen to separate the car from the steel strand, allowing the car to proceed and eventually impact the specimen. A laser speedometer was employed to measure the impact speed, with a laser trigger mechanism positioned at the end of the car. The speed of the car was measured when the car reached 100mm in front of the column.

Table 1. Impact parameters

Impact velocity (m/s)	Impact height (mm)	Impact mass (kg)	Impact area dimension (*w*/mm × *h*/mm)	Impact energy (J)
4	500	900	200 × 260	7200

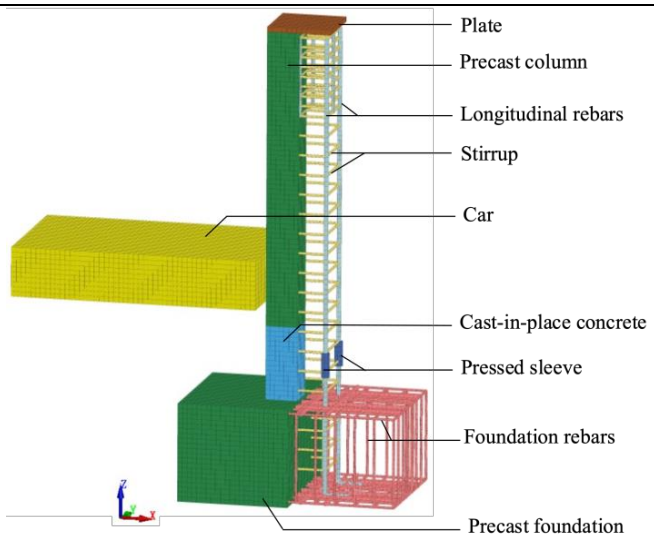

Figure 3. Finite element model for PC column

2.2. Geometry of FE model

The PC column and the RC column are modeled using FE package LSDYNA. Figure 3 illustrates the FE mesh for the columns PC260-4-900. Eight nodes constant stress solid elements are used to model the plate, column concrete, foundation concrete, and rigid car. The rebars are modeled using two node Hughes-Liu beam elements with 2 × 2 Gauss integration. Meanwhile, zero-energy modes of concrete elements are prevented using the stiffness-based hourglass control method with a coefficient of 0.05.

2.3. Material model

The concrete of the column and the foundation is simulated by MAT_159. MAT_159 is in keyword format as MAT_CSCM for Continuous Surface Cap Model. For the CSCM material model, estimation of erosion is built-in and the value of ERODE is taken as 1.05. Moreover,

the stiffness recovery of the material is controlled by a parameter named RECOV, which is taken as 0.5 in this model. The concrete model maintains constant fracture energy to reduce mesh sensitivity. MAT_3 (MAT_PLASTIC_KINEMATIC) is employed to predict the dynamic behavior of rebars and sleeves in the column, and the strain rate effect is characterized by the Cowper-Symonds model. Meanwhile, because no damage on the pressed sleeves is observed in the test, the pressed sleeve is simplified as a perfect rebar with a diameter of the outer diameter of sleeve. The car and the plate are simulated by MAT_20(MAT_RIGID). The material model characteristic in the current research is presented in Table 2.

Table 2. Material properties of FEA model

Element	LS-DYNA model	Input parameter	Magnitude
Concrete	*Mat_CSCM_Concrete	Mass density	2400 kg/m^3
		Unconfined compression Strength	23.7 MPa for PC components 18.9 MPa for cast-in-place concrete
		ERODE\RECOV	1.05\0.5
Steel	*Mat_Plastic_Kinematic	Mass density	7800 kg/m^3
		Yield stress	400 MPa
		SRC\SRP	40\5
Rigid	*Mat_Rigid	Young's modulus	2.1×10^5 MPa
		Poisson's ratio	0.3

2.4. Contact modelling

In LS-DYNA, a variety of contact algorithms are available to address distinct simulation requirements. The interactions between the rigid car and the concrete column, as well as between the steel plate and the concrete column, are modeled utilizing the AUTOMATIC_SURFACE_TO_SURFACE method. The concrete and the reinforcement are coupling by the algorithm of CONSTRAINED_LARGRANGE_IN_SOLID. Meanwhile, the shear stress between the concrete and the longitudinal rebars of the column is modelled by CONTACT_1D. For the interface of new and old concrete, a coefficient of friction of 0.6 is assumed between the two concrete part [13, 14].

Besides, bond at old and new concrete interface is simulated utilizing the contact tiebreak surface-to-surface. Referred to [15-17], the bond strength failure criterion and the calculation formula of the normal and shear stresses at failure are as follows:

$$\left(\frac{|\sigma_n|}{\sigma_{n,F}}\right)^2+\left(\frac{|\sigma_s|}{\sigma_{s,F}}\right)^2\geq 1 \tag{1}$$

$$\sigma_{n,F}=0.2\sqrt{\min(f_{c1}^{'},f_{c2}^{'})}(\text{Units:MPa}) \quad (2)$$

$$\sigma_{s,F}=0.62\sqrt{\min(f_{c1}^{'},f_{c2}^{'})}(\text{Units:MPa}) \quad (3)$$

where σ_n and σ_s are, in turn, the normal and shear stresses at contact surfaces, $\sigma_{n,F}$ and $\sigma_{s,F}$ are the normal and shear stresses at failure, f_{c1}' and f_{c2}' are the axial compressive strength of precast concrete and post-pouring concrete.

2.5. Boundary conditions and loading setting

This preloaded axial compression is applied by using LS-DYNA keyword card ∗ LOAD_SEGMENT_SET. As depicted in Figure 4, the right-side surface of the foundational block is constrained against displacement along the *x*-axis. Additionally, select regions on both the top and bottom surfaces of the foundation are restricted from displacement in the directions of *z*-axis, indicating a fixed boundary condition in the vertical direction.

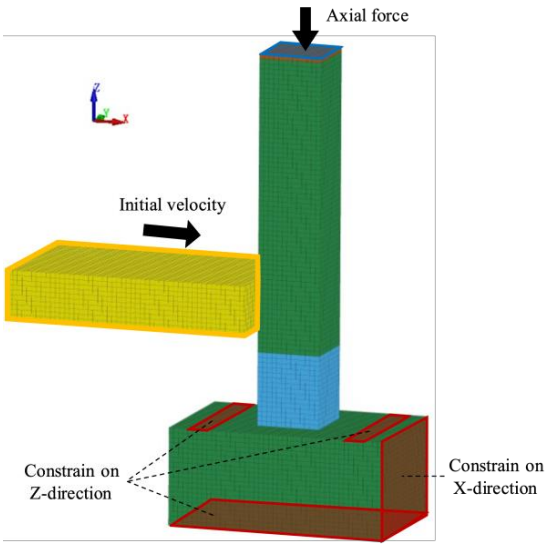

Figure 4. Boundary conditions and inital setting of the FEA model.

3. VALIDATIONS AND DISCUSSIONS

3.1. Failure mode

The comparisons of failure mode between numerical and test results are shown in Figure 5. As depicted in Figure 5(a), damage cracks are evident at the bottom of the RC column following the impact experiment. Concurrently, results from finite element simulation indicate a pronounced plastic strain at the same location. Both experimental result and finite element simulation revealed slip phenomena at the interface of the PC column, as shown in Figure 5(b). It can be seen that the concrete damage predicted by the numerical model is consistent with the

distribution of concrete cracks in the test. These multiple comparisons between the numerical results and experimental results demonstrate the accuracy of the numerical models.

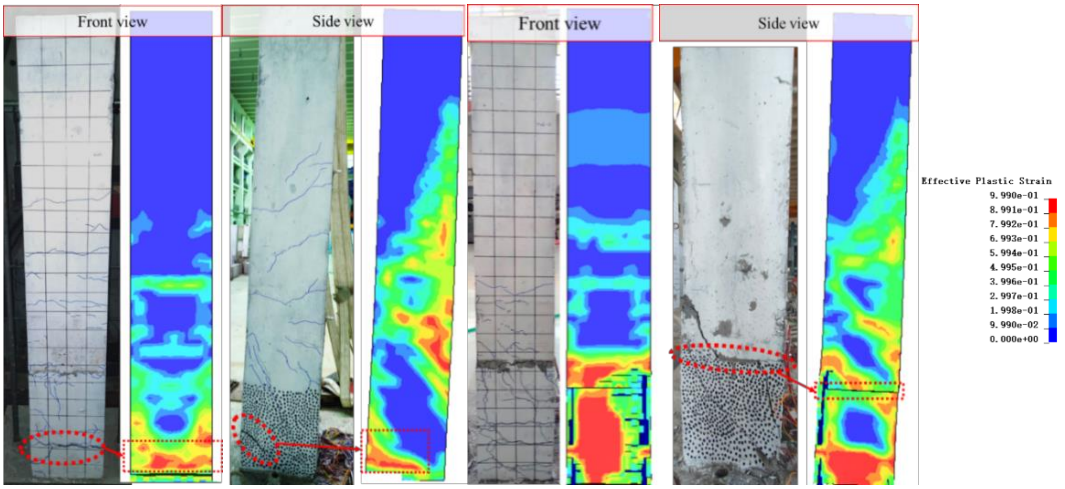

(a) RC260-4-900 (b) PC260-4-900

Figure 5. Comparison of concrete damage between test and FE simulation

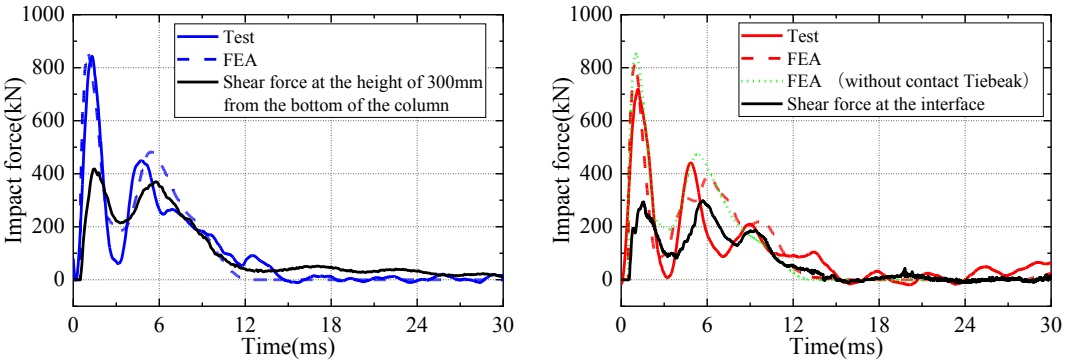

(a) RC260-4-900 (b) PC260-4-900

Figure 6. Comparison of load response between test and FE simulation

3.2. Load-displacement response

The time histories of the impact force are compared as shown in Figure 6. The maximum impact forces for RC260-4-900 and PC260-4-900 from the numerical results are 854.73kN and 819.01kN, respectively, which closely align with the 843.25kN and 718.59kN obtained in the experimental results. In addition, both the second peak impact forces from the simulations are closely to the experimental ones. Figure 6 also shows the shear force time-history curves at the section 300 mm high for the RC column and PC column finite element models. It can be observed that the overall trend of the shear force time-history curves is very similar to that of the impact force time-history curves. The peak shear force of the PC column model is 291 kN and 416 kN for the RC260 model, with the shear force representing 35.8% and 48.8% of the peak impact force for each respective member. This indicates that the continuous interface can transmit greater shear forces under the impact due to its structural consistency and integrity. While the interface in precast member, due to its small gaps or discontinuities, has a lower shear force transmission efficiency.

The time histories of the impact displacement at the impact point and the top of the column are compared as shown in Figure 7. The simulated maximum displacements at the impact point and the top of specimen RC260-4-900 are 32.52mm and 80.34mm, respectively, which are comparable to 29.40mm and 84.10mm from the experimental results. Similarly, the simulated maximum displacements at the impact point and the top of specimen PC260-4-900 are 39.14mm and 87.59mm, respectively, which are comparable to 36.10mm and 92.00mm from the experimental results. According to Figure 7, when comparing the experimental curves of RC and PC, there is a noticeable increase in peak displacement and a longer plateau at the peak. As observed from Figure 5, significant slip phenomena were observed at the interface of PC columns after impact. This observation confirms that the increase in displacement in PC column was partly due to slip at the concrete interface. Consequently, when using Tiebreak contact to simulate the concrete interface, the simulated member exhibits an increase in peak displacement compared to simulations without Tiebreak contact, and also maintained a longer plateau at the peak.

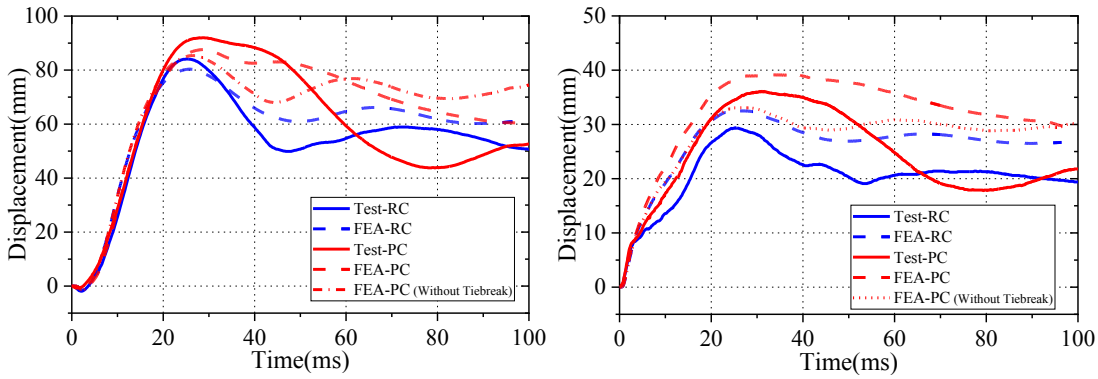

(a) Lateral displacementat the top of the column (b)Lateral displacementat the impact point

Figure 7. Comparison of displacement response between test and FE simulation

4. PARAMETRIC STUDY

Following the validation of the FE models, an intensive parametric study was carried out to explore the influence of impact parameters including the impact velocity, axial compression ratio, and different impact mass and velocity with the same impact kinetic energy, on the dynamic responses of the columns.

4.1. Impact velocity

The performance of the PC column is examined under different impactor velocity, such as 2m/s, 3m/s, 4m/s, 5m/s, and 6m/s. Figure 8 illustrates comparisons of impact force and lateral displacement of the reference column. As expected, with an increase in impact velocity, both the peak impact force and peak displacement of the member increase. The first peak impact force increases but the second peak impact force remain almost the same as the impact velocity increases.

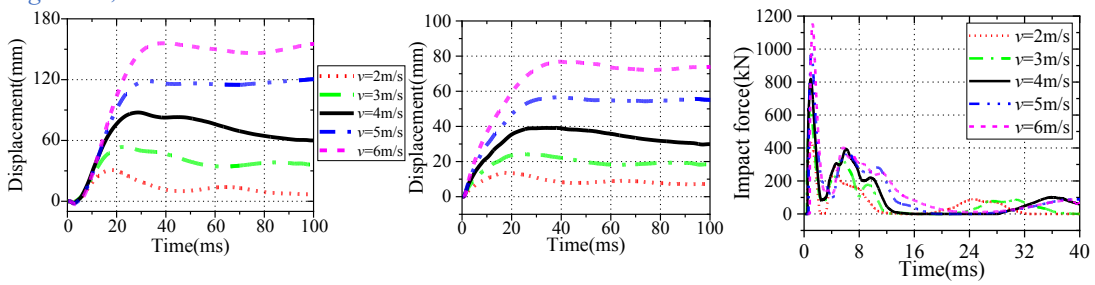

(a) Lateral displacement at the top of the column

(b)Lateral displacement at the impact point

(c) Impact force

Figure 8. Impact responses of columns under different impact velocity

4.2. Axial compression ratio

The impact responses of the column under different axial compression ratios are shown in Figure 8. As depicted in Figure 9 (a) and (b), it can be seen that as the axial compression ratios increase, the peak displacements of the members decrease and the peak displacements decrease more quickly. It can be obtained that increasing axial compression ratio not only reduces the peak lateral displacements of the columns but also diminishes the slippage at the interface between new and old concrete. However, when axial compression ratio is set to 0.6, there is complete failure in the simulated specimen at the time of 65ms. As shown in the Figure 9(c), the axial compression ratio has little influence on the impact force. But the minimum forces between the first and second peak forces exhibit a decreasing trend with the decrease in axial compression ratio.

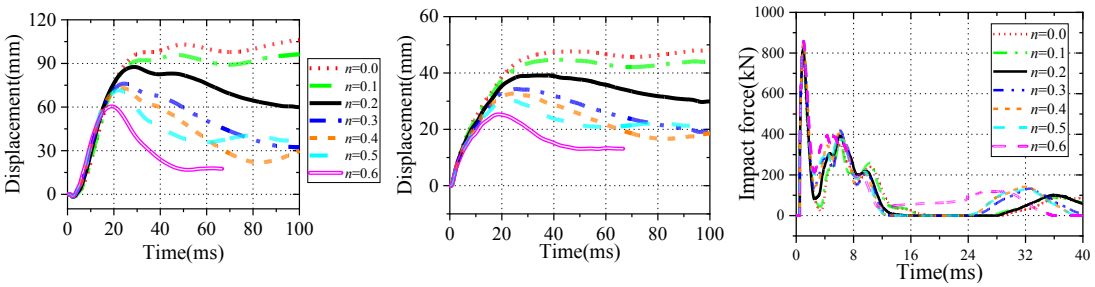

(a) Lateral displacement at the top of the column

(b)Lateral displacement at the impact point

(c) Impact force

Figure 9. Impact responses of columns under different impact axial compression ratio

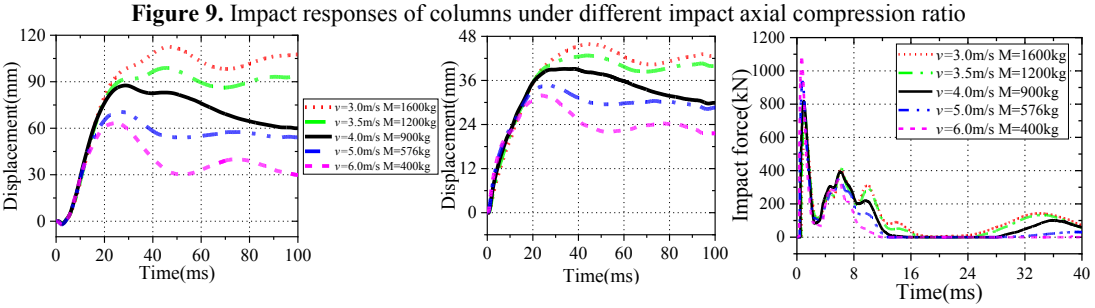

(a) Lateral displacement at the top of the column

(b)Lateral displacement at the impact point

(c) Impact force

Figure 10. Impact responses of columns under different combinations with the same impact energy

4.3. Different impact mass and velocity with the same impact kinetic energy

Figure 10 depicts impact forces and lateral displacements of the PC column under different combinations of impact mass and velocity with the same impact energy. As observed from these figures, a larger impact mass leads to greater impact displacement and smaller impact force under the same impact kinetic energy.

5. CONCLUSIONS

This study performs numerical analysis of the dynamic performance of RC columns with pressed sleeve connections. The findings are summarized as follows:

(1) The finite element model based on LS-DYNA, incorporating contact mechanisms like contact tiebreak and CONTACT_1D, exhibits robust accuracy in simulating the impact force, displacement, and failure modes of the columns. The interface in precast member, due to its small gaps or discontinuities, has a lower shear force transmission efficiency. When using Tiebreak contact to simulate the concrete interface, there was a slip at the interface in PC column. Consequently, the simulated component displayed an increase in peak displacement and sustained a longer plateau at that peak.

(2) Following this validation, an intensive parametric study was carried out to explore the influence of impact parameters on the dynamic responses of the columns. The results show that as the axial compression ratio increases, it not only reduces the peak displacement of the member but also diminishes the slippage at the interface between new and old concrete. With an increase in impact velocity, both the peak impact force and peak displacement of the member increase. Under the same impact kinetic energy, a larger impact mass leads to greater impact displacement and smaller impact force.

ACKNOWLEDGMENTS

This research work was financially supported by the National Natural Science Foundation of China, Grant No.52178139 and the Guangdong Basic and Applied Basic Research Foundation (Project No. 2024A1515012518).

REFERENCES

[1] Liang Z, Gong C, Zhang S, Liang W, Hou Z. (2023). Tensile behaviors and configurations of double-headed bar overlap connections for precast concrete members. *Engineering Structures*, 293, 116701.

[2] Xu T, Li Q, Zhao R, Ding J, Zhan Y. (2019). On the early-age bond-slip behavior of an eccentric bar embedded in a grouted sleeve. *Engineering Structures*, 190, 160-70.

[3] Liu, Y., Xu, N., Zhao, S., Feng, A., Yang, H., Kang, Y., et al. (2024). Proposal and experimental verification of enhancement method for half-grouted sleeve connection quality. *Construction and Building Materials*, 416, 135161.

[4] Lu, Z., Huang, J., Li, Y., Dai, S., Peng, Z., Liu, X., et al. (2019). Mechanical behaviour of grouted sleeve splice under uniaxial tensile loading. *Engineering Structures*, 186, 421-435.

[5] Li, H., Chen, W., Hao, H. (2019). Dynamic response of precast concrete beam with wet connection subjected to impact loads. *Engineering Structures*, 191, 247-263.

[6] Su, H., Yang, C., Sun, C., Hu, L., Fan, W. (2024). Seismic performance of precast multi-segment columns with grouted sleeves: Experimental and numerical investigations. *Engineering Structures*, 301, 117239.

[7] Xu, L., Pan, J., Guo, L. (2022). Mechanical performance of precast RC columns with grouted sleeve connections. *Engineering Structures*, 252, 113654.

[8] Zeng, Z., Yu, W., Luo, Y., Wu, C., Liu, X. (2022). Experimental study on seismic behavior of precast concrete circular section column with grouted sleeve. *Journal of Building Engineering*, 46, 103693.

[9] Guo, T., Yang, J., Wang, W., Li, C. (2022). Experimental investigation on connection performance of fully-grouted sleeve connectors with various grouting defects. *Construction and Building Materials*, 327, 126981.

[10] Xu, F., Wang, K., Wang, S., Li, W., Liu, W., Du, D. (2018). Experimental bond behavior of deformed rebars in half-grouted sleeve connections with insufficient grouting defect. *Construction and Building Materials*, 185, 264-274.

[11] Yuan, C., Cai, J., Chen, Q., Liu, X., Zuo, Z., He, A., et al. (2023). Experimental study on seismic behaviour of precast recycled fine aggregate concrete columns with pressed sleeve connections. *Structures*, 48, 1373-1390.

[12] Yuan, C., Cai, J., Chen, Q., Liu, X., Huang, H., Zuo, Z., et al. (2022). Experimental study on seismic behaviour of precast recycled fine aggregate concrete beam-column joints with pressed sleeve connections. *Journal of Building Engineering,* 58, 104988.

[13] ACI Committee 318. (2019). *Building code requirements for structural concrete and commentary* (ACI 318-19). Detroit, MI: American Concrete Institute.

[14] Elsanadedy, H. M., Al-Salloum, Y. A., Alrubaidi, M. A., Almusallam, T. H., Abbas, H. (2021). Finite element analysis for progressive collapse potential of precast concrete beam-to-column connections strengthened with steel plates. *Journal of Building Engineering*, 34, 101875.

[15] Elsanadedy, H. M., Almusallam, T. H., Alsayed, S. H., Al-Salloum, Y. A. (2013). Flexural strengthening of RC beams using textile reinforced mortar – Experimental and numerical study. *Composite Structures*, 97, 40-55.

[16] Silfwerbrand, J. (2003). Shear bond strength in repaired concrete structures. *Materials and Structures/Materiaux et Constructions*, 36(260), 419-424.

[17] Chen, G., Cheng X., Li Y. (2024). A detailed numerical analysis for progressive collapse of precasted concrete frame substructures with wet connections. *Engineering Mechanics*, 1-8. (in Chinese)

PROTECT2024